Electronic Structure and Light Emission from Erbium Centers in Silicon

by

Fanqi Gan

B.S., Electrical Engineering and Computer Science

Peking University, 1989

M.S., Physics

University of Missouri-Kansas City, 1991

Submitted to the Department of Materials Science and Engineering

in partial fulfillment of the requirements for the degree of

Master of Science in Electronic Materials

at the

Massachusetts Institute of Technology

May 1995

© 1995 Fanqi Gan. All rights reserved

Author _____

Department of Materials Science and Engineering

May 12, 1995

Certified by _____

Lionel C. Kimerling

Thomas Lord Professor of Material Science

Thesis Supervisor

Accepted by _____

Carl V. Thompson II

Professor of Electronic Materials

Chair, Departmental Committee on Graduate Student

MASSACHUSETTS INSTITUTE OF TECHNOLOGY

JUL 20 1995

LIBRARIES ARCHIVES

Electronic Structure and Light Emission from Erbium Centers in Silicon

by
Fanqi Gan

Submitted to the Department of Materials Science and Engineering
on May 12, 1995, in partial fulfillment of the
requirements for the degree of Master of Science in Electronic Materials

Abstract

The electronic structures of erbium and related ligand impurities (oxygen and fluorine) are studied by using the self-consistent-field multiple scattering Xα theory within the framework of the molecular cluster model. The quasirelativistic theory in which the radial functions inside each atomic sphere satisfy an average Dirac equation that includes the Darwin and mass-velocity corrections, but not spin-orbit term on this work, has been used in connection with the spin-restricted and spin-unrestricted formalism.

The possible defect positions of erbium are evaluated by comparing the results of two different geometry of clusters. The substitutional impurity has been simulated by a cluster containing 71 atoms: the impurity, Er, 31 silicon atoms, and 36 hydrogen terminators. The tetrahedral interstitial erbium impurity has been simulated by a cluster of 39 atoms: the impurity Er, 14 silicon atoms, and 24 hydrogen terminators.

The Er 4*f* and 6*s* states are treated as valence states. The calculated results do not support the assumption that the 4*f* electrons can be treated as a frozen core. The results show that hybridization among 4*f*, 6*s*, 5*d*, and 6*p* orbitals takes place in the interaction between Er and the silicon host atoms.

High symmetry (T_d) ligands (O, F) are added to the system around Er impurity to best simulate the real sample. Bonding between O (F), Si and Er 4*f* orbitals are observed. The positions of O and F ligands are crucial to the results.

It is necessary to maximize the Si:Er luminescence intensity to improve Si:Er performance as an optoelectronic semiconductor material. The understanding of mechanisms of excitation and thermal quenching of Si:Er luminescence are essential. The dependence of the photoluminescence intensity as well as its rise and decay times on excitation power and temperature were studies. The important role of the quenching of the luminescence by an impurity Auger process was observed. The results are described by a set of rate equations considering radiative and nonradiative processes which occur during excitation and decay.

Thesis Supervisor: Lionel C. Kimerling
Title: Professor

Acknowledgments

I would like to express my deepest gratitude to my advisor, Professor L.C. Kimerling for his generous support, consistent encouragement and excellent guidance. It is most valuable and wonderful experience working with him.

I would also like to thank Dr. Jurgen Mechel for the discussion and general help.

My special thanks goes to Dr. Jorg Palm, who taught me experimental skills and gave me very valuable help in doing experiment and data analysis. I am also grateful to visiting Prof. Lucy Aassali, who helped me analyze the theoretical calculation.

I also want to thank my group members for their friendship and help through my study at MIT, especially my officemate Mike Morse. I do benefit from all kinds of discussion with him. They make my life here more enjoyable. It is fortunate to be in such a wonderful group. Ms. Kate Paterson, the group secretary deserves special thanks for doing a excellent job of managing all the accounting and purchasing matters.

Finally, I would also like to thank my family: my parents and my brother for their encouragement and love. I want to thank my wife Sharon Xin Lu for her understanding, support and love.

Contents

List of Figures

List of Tables

Chapter 1

Introduction

Crystalline silicon, the heart of the modern computer and telecommunications industry, is an extremely well characterized material. It has the best combination of physical and chemical properties, making it the material of choice for data processing and memory chips. Silicon VLSI is the most mature technology of any electronic material. Its role is unlikely to be replaced for a long time. However, silicon does not emit light well mainly due to its indirect bandgap, which precludes it use in display devices, lasers and so on. Instead, more complex compound semiconductor materials such as GaAs and InP are used in optical applications. Therefore, it will be very exciting to see the light coming out of silicon and the production of silicon light-emitting diodes (LED). Integration of the high functionality of silicon integrated circuits (ICs) with the high information carrying capacity of optical fiber networks will result in a significant increase of information processing capability. Optical interconnects have advantages over metal interconnects in areas like interconnection density reduction by multiplexing and drive power reduction by elimination of on chip interconnection the resistance and capacitance. Such a device would enable optoelectronic circuit to be based entirely on silicon and would revolutionize VLSI technology since other required Si-based devices (detectors, waveguides, modulators, etc.) have already been demonstrated. This is a very hot research area in recent years. Extensive research has been devoted to the development of silicon based light sources. Dramatic progress has been made in recent years. Among the alternatives, erbium-doped

silicon (Si:Er) stands out as a promising candidate for a fully integral silicon based LEDs. The 1.54 μm emission wavelength matches the minimum absorption loss of silica fibers and is compatible with existing silica-based optical network. The first room temperature Si:Er LED was demonstrated recently, but the relatively small power output hampered its commercial application [1]. Nevertheless, it is a big stride forward.

In order to continuously improve functionality of Si:Er LEDs, it is necessary to have a thorough understanding of how Er and its related defects behave in silicon before a better LED design and optimal processing conditions can be achieved. Some of fundamental properties of the Si:Er system remain unclear, such as the Er defect configuration and the photoluminescence (PL) mechanism. Further more, it has been observed that coexistence of some ligands with large electronegativities greatly enhance the PL intensity[2]. Some of these elements are F, O, C, B, etc. However, the role of these ligands during the PL process is not fully understood yet. These are some of the critical problems that need to be investigated to get better room temperature light emission, and they are the main issues to be addressed in this thesis.

It is well known that there should be some crystal field around Er to assist light emission process [3]. Because the existence of a ligand field causes some mixing of wavefunctions of Er $4f$ electrons and other atoms, this configuration helps break the parity of forbidden transition of intra $4f$ electrons. The crystal field effect for rare earth (RE) elements in ionic materials were subjected to extensive studies in 50s and 60s. In the next chapter, we will summarize the published results of crystal field studies of RE in different materials and to provide a background for our investigation.

Chapter 3 will illustrate the theoretical approach used in this study, the self-consistent field multiple scattering Xα method. The results are presented in Chapter 4. Comparison to other researchers' work and assessment of our data are also included in chapter 4. From the computational results by the Xα method, it is believed that the $4f$ electrons can not be treated as core (or frozen) electrons as other theoretical publications have done. The $4f$ electrons, although very localized, still interact with the host to some extent, especially in the presence of ligands. Positions of the Er impurity levels are proposed and evaluated based on the calculation results. The improvements obtained by

applying quasi-relativistic calculations (only the Darwin and Mass velocity correction considered) demonstrate the importance of relativistic effects for such a system involving the heavy atom Er (atomic number 68). We also believe that the spin-orbit interaction is very important. The full relativistic correction is in progress.

Chapter 5 attempts to address the problem of PL excitation and deexcitation mechanisms from an experimental point of view. Extensive experimental data will be shown here. The PL intensity dependence on excitation power and temperature, and the rise and decay time dependence on power and temperature will be presented here. The PL intensity and decay time for different coimplanted ligands are also discussed. We have found a difference for p-type and n-type samples in the thermal quenching process. The understanding of this difference is very important because the Fermi level position determines whether a level in the gap is electrically active or not. Based on the experimental evidence, especially lifetime measurements, we believe that Auger effect is mainly responsible for the thermal quenching at least in the low temperature range (4 K - 130 K).

Based on the above results, Chapter 6 will set up a set of rate equations to describe the kinetics of photoluminescence process. The simulation results of power and temperature dependence of PL intensity will be compared to the experimental data. The presented rate equations are reasonably successful. But more complete rate equations are necessary to have a better agreement with the experiment. Finally, a summary and future work are discussed in Chapter 7.

Chapter 2

Literature Review

2.1 General Properties of Rare Earth Elements

The rare earth elements form a group of similar chemical properties which have in common an open $4f$ shell. The trivalent ion is the most stable state, and it is principally the properties of the trivalent ions which are important rather than those of neutral atoms. All trivalent ions have the xenon-like rare gas shell of 54 electrons in common. The trivalent $4f$ electron number n ranges from 0 (La^{3+}) to 14 (Lu^{3+}). Some of the important properties of these ions are summarized in Table 2.1

Due to the common feature of partially filled $4f$ shell (Ce to Yb), all rare earths have similar though not identical chemical behavior. They are strongly paramagnetic, in some cases ferromagnetic or antiferromagnetic at low temperatures. Absorption spectra and fluorescence spectra with sharp lines in the visible or infrared regions have been observed when they are in the 3+ charge states. Some divalent ions like Sm^{2+} also have a pronounced sharp-line spectrum, while divalent europium seems to produce chiefly a continuous spectrum [3].

One of the most recognized pioneer investigators in this field is Professor G. H. Dieke from John Hopkins University. His investigations were begun in 1953. The primary concern of his study was to understand the electronic structure of $4f^n$ levels of rare earths and its relationship to the optical spectra of these elements. Most of his results were summarized in the book "Spectra and Energy Levels of Rare Earth Ions in Crystals" [3].

Some earlier work of other researchers can be found in another book edited by Professor Dieke. "Optical Properties of Ions in Crystals" [4].

Table 2.1. Properties of trivalent rare earth ions

Z		Ground state	Electronic Configuration	Ionic Radius (Å)	Covalent Radius (Å)	Electronegativity (Pauling's)
57	La	$^1S_0$	$4f^0 5s^2 5p^6$	1.061	1.69	1.10
58	Ce	$^2F_{5/2}$	$4f^1 5s^2 5p^6$	1.02	1.65	1.12
59	Pr	$^3H_4$	$4f^2 5s^2 5p^6$	1.00	1.65	1.13
60	Nd	$^4I_{9/2}$	$4f^3 5s^2 5p^6$	0.99	1.64	1.14
61	Pm	$^5I_4$	$4f^4 5s^2 5p^6$	0.98	1.53	1.13
62	Sm	$^6H_{5/2}$	$4f^5 5s^2 5p^6$	0.97	1.62	1.17
63	Eu	$^7F_0$	$4f^6 5s^2 5p^6$	0.97	1.85	1.20
64	Gd	$^8S_{7/2}$	$4f^7 5s^2 5p^6$	0.97	1.61	1.20
65	Yb	$^7F_6$	$4f^8 5s^2 5p^6$	1.00	1.59	1.20
66	Dy	$^6H_{15/2}$	$4f^9 5s^2 5p^6$	0.99	1.59	1.22
67	Ho	$^5I_8$	$4f^{10} 5s^2 5p^6$	0.97	1.58	1.23
68	Er	$^4I_{15/2}$	$4f^{11} 5s^2 5p^6$	0.96	1.57	1.24
69	Tm	$^3H_6$	$4f^{12} 5s^2 5p^6$	0.95	1.56	1.25
70	Yb	$^2F_{17/2}$	$4f^{13} 5s^2 5p^6$	0.94	1.74	1.10
71	Lu	$^1S_0$	$4f^{14} 5s^2 5p^6$	0.85	1.56	1.27

Generally, it is possible to observe very sharp emission and absorption lines only when atoms or molecules are in the gaseous state or at very low pressure. Under these conditions, the distance between atoms or molecules can be considered large so that their properties are those of the isolated atoms. As the distance between atoms is reduced (pressure increases), interactions (collision) between neighboring atoms are increased and can not be ignored anymore. The interactions cause sharp lines to overlap and results in a continuous spectrum without noticeable structure.

In a constant static field (crystal field), ions can produce large Stark effects which give sharp components. But the thermal motion (vibration) of ions averages the effect to a continuous spectrum. Thus it seems that only at temperatures close to absolute zero should sharp lines be seen in a concentrated system. However, even though lower temperature indeed reduces the thermal motion, the interaction among neighboring atoms can still exist through resonant molecular orbital interactions. This resonance means that the valence electron is not strictly localized in the vicinity of one nucleus, but is partly shared by the neighbors. This effect is more important in covalently bound semiconductors than ionic crystals.

We can briefly summarize the conditions for which sharp line emission or absorption spectra can be observed in liquid and solids. First is the minimum fluctuations of the position of surrounding atoms. It means that low temperature is necessary. Second is the minimum interaction among neighboring atoms, i.e., the electron responsible for the emission or absorption should be very localized. The wave functions of these electrons of neighboring atoms must not appreciably overlap. Thus, the salts of rare earths are ideal candidates for the study of RE optical spectrum. The $4f$ orbitals lie well inside the electronic shell of 5s, 5p and 6s and are well protected.

2.2 The Levels of the Free Ions

If there are n electrons in $4f$ orbitals, we have the $4f^n$ configuration. If there were no interactions between the electrons, i.e., essentially no coulomb and exchange interactions, we would have just one level for this configuration, because the relative orientation of the these orbitals to each other would not matter. Actually, because of the electrostatic (coulomb and exchange) and spin-orbit interactions, there are many levels belonging to one configuration, for instance, when n = 11 (Er^{3+}), there are 41 levels in the case of $4f^{11}$ configuration. Other possible low energy configurations for 11 electrons outside xenon shell are $4f^{10}5d$, $4f^{10}6s$ and $4f^{10}6p$. These are the four lowest energy configurations, and the order is the same for all the trivalent rare earth ions [3]. The four lowest configurations of trivalent rare earth ions are summarized in Table 2.2.

Table 2.2 The number of levels for each of the four lowest energy configurations of free RE^{3+}

RE^{3+}	$4f^n$	$4f^{n-1}5d$	$4f^{n-1}6s$	$4f^{n-1}6p$	Sum	Allowed transitions
La	1	-	-	-	1	-
Ce	2	2	1	2	7	324
Pr	13	20	4	12	49	5393
Nd	41	107	24	69	242	54639
Pm	107	386	82	242	817	306604
Sm	198	977	208	611	1994	
Eu	295	1878	396	1168	3737	
Gd	327	2725	576	1095	4723	
Tb	295	3006	654	1928	5883	
Dy	198	2725	576	1095	4594	
Ho	107	1878	396	1168	3549	
Er	41	977	208	611	1837	
Tm	13	386	82	242	723	42281
Yb	2	107	24	69	202	3733
Lu	1	20	4	12	37	217

In Table 2.2, the integer under each configuration such as $4f^n$ is the total number of possible levels for this configuration. The number is a theoretical value considering all the possible interactions. The integer in "Sum" column is the sum of the levels of each configuration. The number of allowed transitions between these levels is listed in the last column.

2.3 The Crystal Field Effect

When a rare earth ion is placed in a crystal lattice, it is subjected to a number of forces which are absent for the free ion, such as resonance interactions with neighboring ions of the same kind and electric and magnetic interactions with each individual ion. Some of

these interactions are coupling between ion and the crystal lattice, and they provide a gateway for rare earth ions to transfer some or all their energies to crystal lattice vibrations. These can be best described by crystal field theory.

The influence of a crystal field on energy levels and wave functions will modify the PL spectrum. For instance, the ions of the iron group have valence electrons in the protected incomplete $3d$ shell. The localization of 3d electrons, however, is not as good as that of the $4f$ electrons. Thus in most cases, only the ground level of $3d$ ions is sharp enough that paramagnetic resonance measurements are possible. Excited state optical absorption is not easily observed. The fundamental reason behind it is that, in the iron group, the influence of the crystal field on the energy levels is very large, much larger than that of the spin-orbit interaction, and the excited states is delocalized in the host. In the rare earths, the situation is reversed due to the greater localization of $4f$ electrons and the influence of the crystal field can in many cases be regarded as a relatively small perturbation. For $3d$ ions, the spin-orbit interaction energy is about 0.01 eV while the energy due to the crystal field is ~ 1.24 eV. This large crystal field causes a complete breakdown of the Russell-Saunders ($\mathbf{J} = \mathbf{L} + \mathbf{S}$) coupling scheme and J is no longer a good quantum number. But for $4f$ ions, the spin-orbit interaction energy is about is about 1.0 eV while the crystal field splitting energy is about 0.01 eV. The eigenfunction in the crystal are, consequently, to the first-order, linear superposition of the $2J + 1$ degenerate members of a given J manifold. J is thus a fairly good quantum number, but M (magnetic momentum) is not.

The effect of the crystal field is reduction of degeneracy. A free ion level with total angular momentum J is $2J + 1$ fold degenerate. Due to the non-spherical symmetry of crystal field, this spatial degeneracy is partly or totally removed. The symmetry which is of great interest to us is the symmetry of electric field at the position of rare earth ion, which may or may not have the same symmetry as the macroscopic structure of the crystal. Fig. 2.1 shows the Er^{3+} $4f$ state splitting in a crystal field. In particular, the $\lambda = 1.54$ μm light emission observed in Er^{3+} is the transition between the multi-fold splittings of the ground state and first excited state $4f^{11}$ electrons. The number of levels of the $4f$ state splitting depends on the symmetry of the lattice site which surrounds Er^{3+} or RE^{3+} and the total

angular momentum J. Table 2.3 and Table 2.4 list the number of multi-fold split states of RE^{3+} under different symmetries where J is half integer and integer, respectively. If J is a half integer, i.e., there are an odd number of electrons in the *4f* orbital; for the cubic symmetry, there may be doubly and quadruply degenerate levels. For noncubic symmetry, a free ion level with angular momentum J splits into J + 1/2 Stark components. If J is an integer, there are even number of electrons in the *f* orbitals. There are maybe single, double and triply degenerate levels for the cubic symmetry.

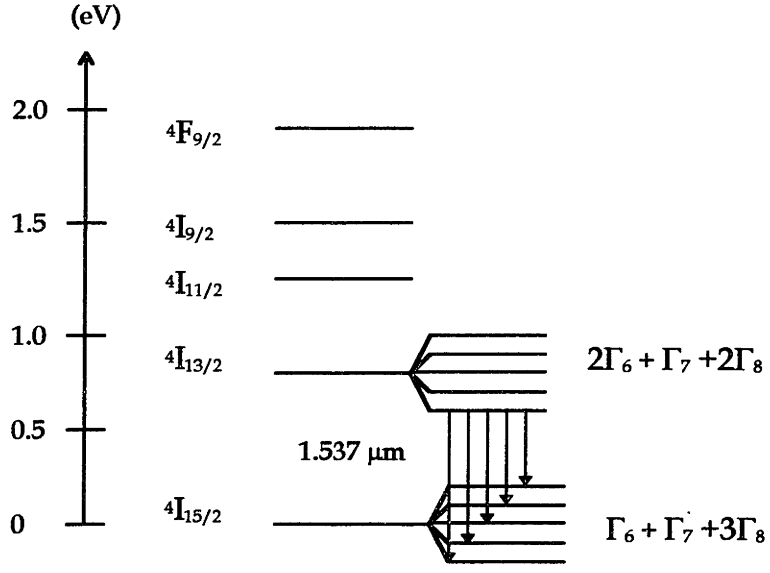

Fig. 2.1 Energy level of Er^{3+} in T_d symmetry

Table 2.3 RE^{3+} ion manifold splitting in crystal field (J= half integer)

		J number							
Symmetry	Degeneracy	1/2	3/2	5/2	7/2	9/2	11/2	13/2	15/2
Cubic O_h, T_d, O, T_h,	Double	1	0	1	2	1	2	3	2
	Quad.	–	1	1	1	2	2	2	3
Non Cubic		1	2	3	4	5	6	7	8

Table 2.4 RE^{3+} ion manifold splitting in crystal field (J= integer)

	J number									
Degeneracy	0	1	2	3	4	5	6	7	8	9
single	1	_	_	1	1	_	2	1	1	2
Double	_	_	1	_	1	1	1	1	2	1
Triple	_	1	1	2	2	3	3	4	4	5
Total	1	1	2	3	4	4	6	6	7	8

2.4 Intensities, Selection, and Polarization Rules

The intensities of absorption or emission lines are given, as in any other cases, by the matrix elements of the multiplets responsible for the transition. The Einstein emission coefficient defines the transition probability is

$$P_{mn} = \frac{64\pi^4 \upsilon^3}{3hc^3} \left|(n|\Omega|m)\right|^2 \qquad (4.1)$$

where Ω is either the electric or magnetic dipole moment. c is the speed of light. ν is the transition frequency.

In so-called "allowed" transitions, the transition probabilities are overwhelmingly determined by the electric dipole moment $\mathbf{d} = \sum_i e\mathbf{r}_i$. The transition rate of visible allowed transitions is of the order 10^8 sec^{-1}. A different way of specifying intensity is by the oscillator strength *f*. The oscillator strength compares the actual transition probability to that of classical oscillating electrons, where the energy radiation loss is given by

$$\frac{dE}{dt} = -aE = -\frac{8\pi^2 e^2 \upsilon^2}{3mc^3} \qquad (4.2)$$

where m is the mass, e is the electron charge.

from which follows

$$P_{nm}=\frac{8\pi^2 e^2 \upsilon^2}{3mc^3} f_{nm}=2.68\bullet 10^9\left(\frac{\sigma}{R}\right)^2 f_{nm} \qquad (4.3)$$

where σ is the wavenumber and R is Rydberg constant. which can also be estimated by Xα potential [5].

$$f=\frac{2\hbar^2}{3m(\Delta E)^3}\langle\Psi_f|\nabla V|\Psi_i\rangle^2 \qquad (4.4)$$

where Ψ_i and Ψ_f and are the initial and final states of the wavefunction. ΔE is the energy difference between initial state and final state.

For an allowed transition the oscillator strengths are of order of magnitude one. For such transitions in or near the visible region, the electric dipole approximation predominates to such an extent that all other contributions may be neglected. This is not true, however, if we deal with forbidden transition where the electric dipole moment is zero or very small.

The transitions between the levels of the $4f^n$ configurations, which are responsible for the light emission, are all forbidden as electric dipole transitions by the parity rule, which is valid if the electron is in a central force field which has a center of symmetry. The parity rule states that in Eq. 4.1, if the initial and final states are the same, for example, both are *f* states. The transition probability will be zero. This is always true for the free ion and the transitions are forbidden. However, the observed emission lines can be due to the following three mechanisms:

- Forced electric dipole transitions
- Magnetic dipole transitions
- Electric quadruple transitions.

A forced electric dipole transition occurs when the force (external) field in which the electrons move does not have a center of symmetry. For instance, this is the case when the rare earth ion is placed in a crystal field, which ordinarily lacks a center of symmetry.

This results in mixed parity wavefunctions. But the weight of nonparity wavefunctions is very small due to the small noncentral symmetric part of the total force field. Thus intensity is not expected to be very strong.

The expression for the transition probabilities of a magnetic dipole can be easily determined by substituting the magnetic moment for Ω in Eq. (4.1). Similarly, substituting the quadrupole moment tensor Q can give us the electric quadrupole transitions. These two transitions are not the focus of this thesis. Particularly, from the experimentally evidence, the role of the quadrupole transition if (there is any) is very small in the emission spectra [3].

The selection and polarization rules for electric dipole transitions are very important and worth discussion. For the free ion, electric dipole transitions between states of the $4f^n$ configuration are strictly forbidden by the parity rule. But it is quite different for forced electric dipole transitions. These can take place only because of admixtures of opposite parity in the wave functions and admixtures caused by the interaction of the $4f^n$ level with the remote states of opposite parity, such as $4f^{n-1}5d$ or $4f^{n-1}5g$. The wavefunction in a crystal field is

$$\Psi = a\Psi_0 + b\Psi_1 \qquad (4.5)$$

where Ψ_0 is the wavefunction with the parity of $4f^n$ and Ψ_1 is the wavefunction of opposite parity, with the coefficients $a \sim 1$ and $b << 1$. Empirically it has been found that b is of the order of magnitude 10^{-3}, and this follows also from approximate calculation [3].

Most of earlier work in 1960s concentrated on the identification of free ion levels from the crystal spectra. Combined with some empirical calculations, it was highly successful [3]. The lower levels for all of the rare earths ions have been satisfactorily identified. The effect of crystal field was estimated too at the same time both experimentally and empirically. Fig. 2.2 summarizes this achievement for the lower levels of all trivalent rare earth ions. Each level is represented by a line, and the linewidth

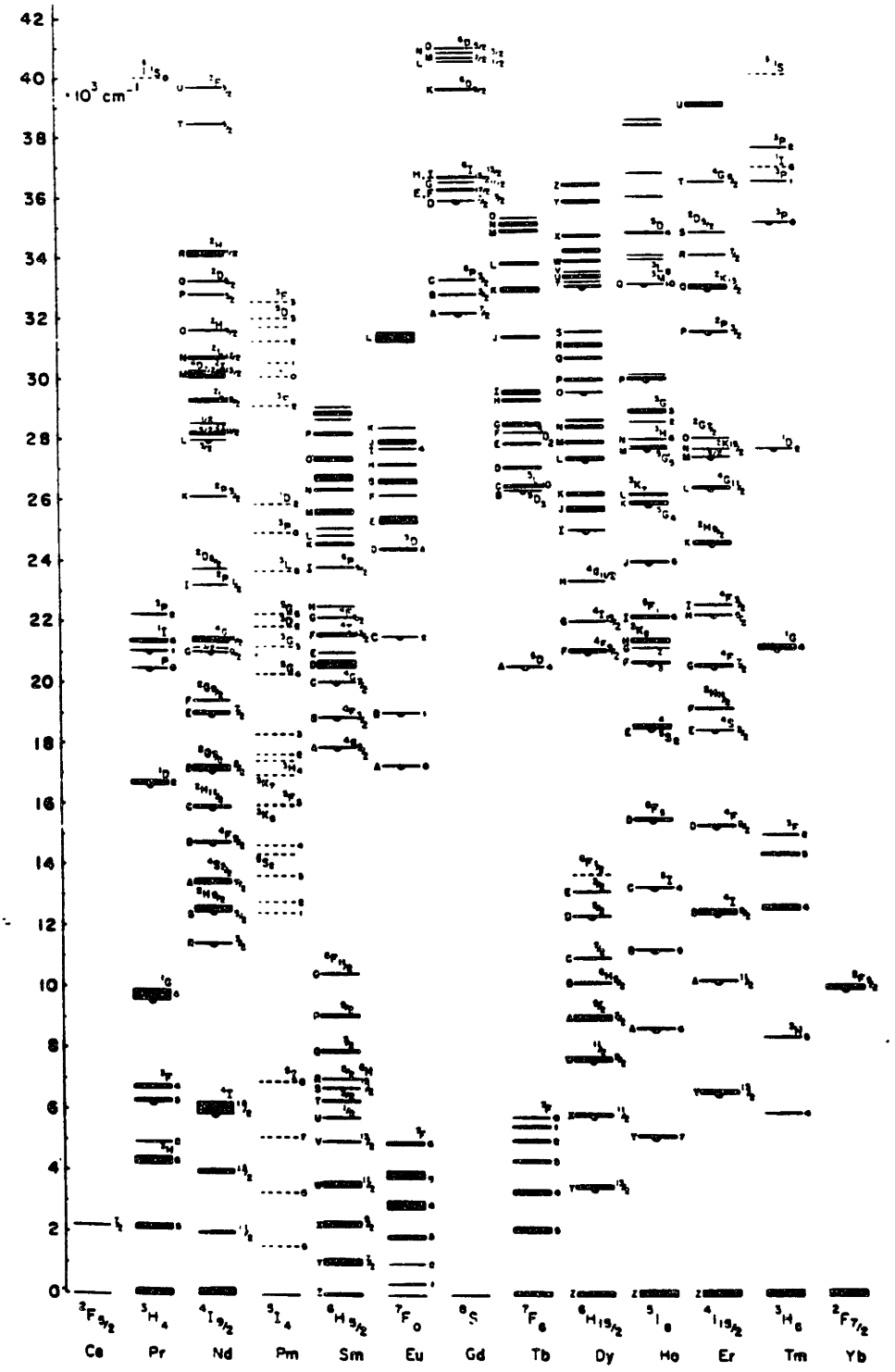

Fig. 2.2 Observed energy levels of the trivalent rare-earth ions. The width of the levels indicates the total separation of the Stark components in the anhydrous trichlorides (after Dieke).

indicates the total crystal field splitting in $LaCl_3$. For our interest and as the example, in Fig. 2.2, the ground state of Er is $I_{15/2}$. The next state above (first excited state) is $I_{13/2}$. The distance (transition energy) between them is about 6.5 $x10^3$ cm^{-1}, which is about 0.8 eV. The ground state crystal field splitting is about 0.03 eV, and it becomes smaller for the states of higher energy. This data is very important information which can be of great help in justifying our calculation later on. But beware the crystal field splitting here is in ionic material which should be somewhat different in a covalent bonded semiconductor such as Si.

The method used in identification of the J number is very straight forward in principle. For an odd number of electrons in a noncubic field, every free ion level splits into J + ½ components. While for an even number of electrons there are 2J + 1 components if the symmetry of the field is low, otherwise the number is smaller but can be determined if the field symmetry is known. As in the case of Er^{3+}, Figure 2.3 shows three successive groups which gave 6, 7 and 8 lines, respectively, which would indicate J = 11/2, 13/2 and 15/2.

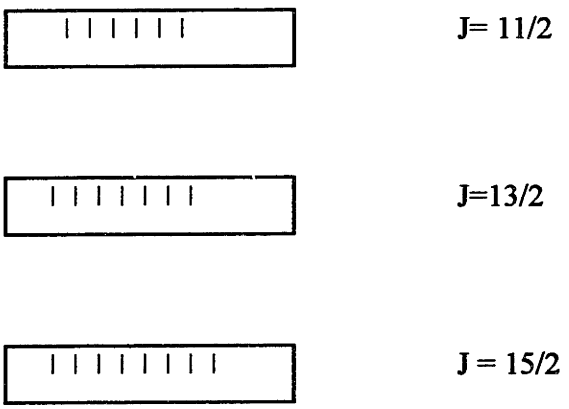

Fig. 2.3 Schematical diagram of identification of J number from spectra

There are some other problems which need special attention. The first is that selection rules may make it impossible to obtain all Stark components. Secondly, the intensities of some lines are so weak that they escape observation. The remedy for this is to observe the same line group in several lattices and make sure that these are lattices of low symmetry. The third problem is that of satellite lines, which means that there are several lines where only one should be. This multiplicity is probably due to the superimposed crystal vibrations that make J appear larger than it really is. This happens when the lattice vibration frequency is the same as the optical transition. Again, repeat experiments of the same line group for different lattices, and choosing those with weak satellite lines can avoid this problem. The forth problem arises when two electronic levels are so close together that their Stark components can not be clearly distinguished. In this case, the theoretical calculation may be very helpful.

2.5 Lattice Location of Rare Earth Ions in Crystal

There are several techniques available to probe the atomic configuration of RE ion in materials, such as Rutherford backscattering (RBS) and channeling, electron paramagnetic resonance (EPR) and PL. RBS it very suitable to determine the location of heavy ions in the lattice. The principle of the lattice location technique is shown in Fig. 2.4. In the simplest case an RBS experiment has to be performed in two configurations. First of all axial channeling spectrum is recorded (Fig. 2.4a). In this measurement only interstitial atoms, apart from atoms at the surface, serve as scattering centers for incident analyzing ion beam. Next, the so-called random spectrum is collected (Fig. 2.4b), from which the total concentration of the impurity atoms can be calculated. The ratio of the channeling / random backscattering yields provides an approximate interstitial fraction of the impurity atoms. Determination of the exact position of an atom in the lattice requires that the angular dependence of the backscattering yield to be measured and model calculations have to be performed. PL studies are the most popular technique, but they are usually used in combination with RBS or EPR experiments. The EPR study is more complicated and will not be discussed here.

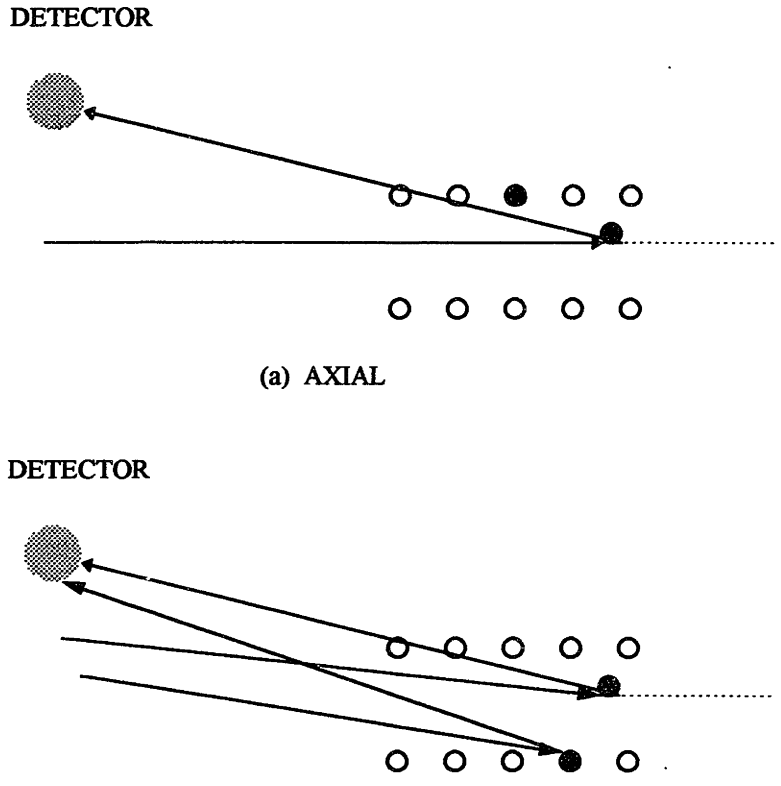

Fig. 2.4 Determination the lattice location by RBS:
(a) axial alignment; (b) random spectrum

The lattice site position of rare earth ions in ionic materials, III-V , II-V compound and Si semiconductors has been subjected to some experimental studies in the past [3,4, 6-11]. For ionic materials such as alkaline earth fluorides (MF_2), generally, it is believed that RE^{3+} will replace M^{2+}. There will be some formation of defects due to charge compensation which will influence the local environment of some of the rare earth ions by modification of the site symmetry on the RE ions. For example, when RE^{3+} is added to CaF_2 which is grown in an excess of fluorine, the predominant site symmetries are cubic, tetragonal and trigonal. People intend to treat RE^{3+} in ionic material as free RE^{3+} in most

cases, because of the low bonding energies. However, this approach is probably not effective in semiconductors.

It is very desirable to understand the lattice site of RE impurities after they are incorporated into semiconductors. This information can help us reduce the defect density and grow high quality RE-doped optoelectronic material. The lattice position of the RE ion in a semiconductor will also influence the bonding between ion and its host. Based on the published studies for III-V semiconductors such as GaAs and InP, there are points worth emphasizing here. The first is that RE has high chemical activity so that high quality growth is hard to achieve [6]. The second is that there is a large misfit between the fourfold coordinated zincblende-type lattice of semiconductors and the sixfold coordination of RE atoms in their stoichiometric As or P compounds (NaCl structure). This structural difference may prevent the RE atoms from occupying regular tetrahedral positions, resulting complex formation. The RE atoms can hardly be considered as isolated entities. The RBS and PL study of Er^{3+} and Yb^{3+} in GaAs and InP shows that Yb atoms locate substitutionally in InP (Yb substitutes In) and InP-based ternary alloys, and are tetrahedrally coordinated. This feature can be attributed to the fact that Yb^{3+} and In^{3+} have similar ionic radii and that has Yb-P partially covalent bond character.

In gallium compounds no substitutional fraction of Yb could be detected and no Yb^{3+} related PL could be observed. One possible explanation is that the electronic level associated with the Yb impurity is located close to the middle of the forbidden gap of GaAs; therefore the energy transferred from recombining charge carriers to the 4*f*-shell of Yb^{3+} is too low to excite the 4*f*-electron shell [7]. However, PL is observed in $Ga_xIn_{1-x}P$ and InPAs alloys. The compositional dependence of Yb PL in alloys suggests that in spite of screening by the outer $5s^2$ and $5p^6$ closed shells, the 4*f*-electron wave function is affected by the presence of gallium and arsenic atoms in the mixed sublattices [6].

Isoelectronic impurities added to a binary compound change the interatomic distances in the common sublattice, while keeping the bond lengths almost preserved. As a result the common sublattice suffers significant bond-angle distortions. Local distortions around impurities due to the shear component of the strain modify the intensity and symmetry of the electric field in the neighborhood of the Yb atom. They may cause the

Stark splitting of the 4*f*-electron energy levels of the RE^{3+} at a particular lattice site. There is a different correlation of PL and Er^{3+} location in GaAs. Interpretation sometimes depends on the growth and doping conditions of the samples. Kozanecki [6] and Alves et al [8] show that Er atoms locate predominantly at interstitial positions. In GaAs, Er^{3+} moves into tetrahedral lattice site as a result of thermal annealing at temperatures higher than 550° C. The location of Er atoms at substitutional positions is accompanied by the disappearance of the intra-4*f* luminescence of Er^{3+}. However, Takahei's experiment has shown that Er^{3+} in GaAs is Er at Ga sublattice, coupling with two oxygen atoms (Er_{Ga}-2O) [9]. The atomic configuration changes with the Er concentration, growth temperature , and oxygen co-doping and the concentration of Er_{Ga}-2O center in the samples is negligibly small [9].

For II-V materials such as ZnSe, several Er^{3+} centers have been found, especially with cubic symmetry. Both substitutional (center I) and interstitial site (center II) exist [4]. For center I, Er substitutes at the Zn site and the Er^{3+} ground state transforms as the Γ_7 representation of T_d symmetry. The study shows that center I only exists when the Er^{3+} concentration is very low and no fluorescence is observed from this center. In order to obtained fluorescence, noble metals such as Cu and Ag are added to modify in the structure of the center. Strong transitions from $I_{15/2}$ to $I_{13/2}$ is observed from center II. The ground state is more than 98% pure $I_{15/2}$, and the first excited state is about 99% pure $I_{13/2}$ based on the empirical calculations [4].

For RE in Si, there is no established experimental study. Tang et al found based on their backscattering angular scanning and PL spectra, that most of Er atoms (about 80%) in Si occupied substitutional sites in samples annealed at 900 C for 30 minutes with an Er implantation dose of 1.0 $x10^{15}$ cm^{-2} [10]. Przybylinska et al. suggested that optically active Er centers in Si(Cz):Er consisted of interstitial Er with cubic symmetry and some additional Er related centers with non-cubic symmetry [11].

The uncertainty of the lattice site of Er in Si leaves large room for both further experimental and theoretical study. From theoretical point of view, it is possible to get all kinds of predications for such a complex. These results have to be interpreted carefully correlated closely with the experimental evidence.

Chapter 3

The SCF -X α Multiple-Scattered Wave Method

3.1 The SCF-Xα Method

The self-consistent field (SCF) multiple-scattered wave (MSW) Xα method has been widely applied to determine the electronic structure of molecules (clusters) with success, especially in the areas of inorganic chemistry, solid state and surface physics. It is uniquely suitable for studies of high atomic number elements such as rare earths, because the localized 4*f* orbitals can be reasonably well described within a given cluster. It is the only known method which allows interactions of 4*f* electrons with valence band (VB) electrons (i.e., it does not treat it 4*f* as frozen core).

The key feature of the Xα method is the adoption of an exchange energy term which is proportional to the cube root of the electron density. The many-electron problem is thus reduced to a series of one-electron differential equations. Equations 3.1 and 3.2 describe the basic framework of Xα method.

$$\left(-\frac{1}{2}\nabla^2 + V_c + V_{X\alpha\uparrow}\right)\Phi_{i\uparrow} = \varepsilon_{i\uparrow}\Phi_{i\uparrow} \qquad (3.1)$$

where ϕ_i is an orbital for an electron with $M_s = 1/2$, and ε_i is its one electron energy. V_c is the Coulomb potential and $V_{x\alpha}$ is an the approximate exchange potential, which can be related to electron density ρ within Slater's model.

$$V_{X\alpha\uparrow} = -3\alpha\left(\frac{3\rho_{\uparrow}}{4\pi}\right)^{1/3} \qquad (3.2)$$

where α is the exchange coefficient.

The Xα method has much in common with the density functional method, which also invokes an exchange term like that in Eq. 3.2. The Hartree-Fock theory, a single Slater determinant of one-electron wave functions is used to represent the wave function, by expanding the one-electron wave functions in terms of basis functions such as linear combination of atomic orbitals (LCAO). The Schrödinger equation can be solved by matrix manipulation. The exact (SCF) Hartree-Fock calculation are difficult and costly, because they require a large basis set and involve many multicenter integrals. Aimed at efficiency and accuracy, SCF-MSW is one of such methods, which will be only briefly discuss here. There are many excellent review papers about this method, interested reader may refer to them for more details [12-15].

The local exchange potentials described by Eq. 3.2 is based on Slater's statistical approximation. However, the atomic values of the factor α is not unique; it ranges from 0.67 to 1[16]. For a given cluster, weighted average values of α should be used. In most cases it doesn't affect the final results very much, so that many calculations adopt an average value 0.7 or some studies have adopted empirical adjustments of αs to fit certain molecular or crystal properties.

There are also considerable effort trying to find a more solid theoretical foundation and incorporate the effects of electron correlation as well as exchange. The most widely used approach has been the local density approximation, in which the contribution to the exchange and correlation energy at each point is assumed to be the same as that in a homogeneous electron gas of the same density. The correlation energy is defined by the energy difference between the exact total energy of an electronic system and the Hartree-Fock total energy. Such a refinement is not always important because the approximations involved in solving the one-electron equations are often greater than the errors in the potentials themselves. In our tests, using Xα potential and Hedin-Lundqvist potential

(which has the same form as the Xα potential, but with a density-dependent α that resembles that of the "optimal" α factor.) gives essentially the same results.

There are also some studies of the local exchange and correlation potentials for relativistic calculations, which exhibit important differences in the high electron density region from nonrelativistic calculations. Such effects appear to be unimportant for the valence orbital.

3.2 Multiple-Scattered Wave Theory

One of popular methods of solving Eq. 3.1 approximately is to use multiple scattering theory. In this approach, the potential is assumed to be spherically symmetric inside a cell surrounding each atom (region I), and outside an "outer sphere" (region III) that surrounds the entire molecule. In the remaining "intersphere" region (region II), a constant potential is assumed. With these assumptions, the wavefunction may be determined essentially exactly, subject only to errors in the radial numerical integrations inside the atomic spheres and to truncation of angular momentum expansions. (Fig. 3.1)

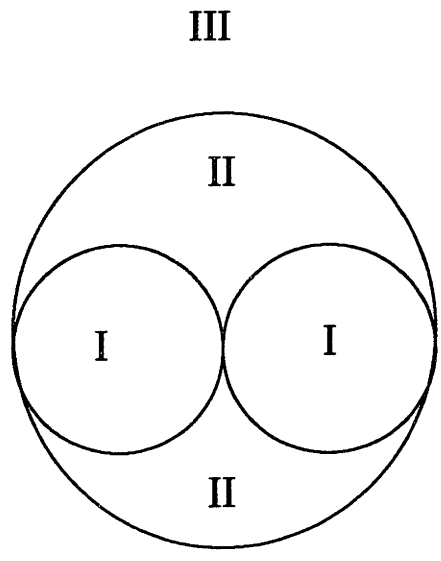

Fig. 3.1: Partition of a molecular cluster into (I) atomic, (II) interatomic, and (III) extramolecular regions.

In practice, the MSW method is usually able to include enough mesh points and spherical harmonic expansion functions to obtain convergence, even for sizable clusters. However, one obvious problem is the constant potential region which is not very realistic. One remedy is to allow sphere overlapping to remove charge from the intersphere region. But the overlapping results in three conceptual problems. The first is the wavefunction of overlap regions is not uniquely defined. Second, the charge in these regions is double counted. Third, the radii of atomic regions are somewhat arbitrary. The most successful procedure implemented by far was proposed by Norman [17], which begins from a superposition of atomic charge densities in the molecular geometry. Relative sphere sizes are determined by finding the atomic number radii that enclose an electron charge equal to the nuclear charge. Absolute radii are then chosen by scaling these values uniformly to satisfy the viral theorem.

The MSW method has often been combined with Xα theory, but one is free to use different exchange-correlation formalism. If the cluster carries a net charge or you want to impose an net charge for the cluster, the stabilizing Madelung potential of a crystalline can be mimicked through the use of a Watson sphere [18]. This approach usually results in a shift of the energy levels for each orbital, but the relative positions are not affected.

3.3 Relativistic Calculations

The use of relativistic calculations is very importance for the work of this thesis because Er is such a heavy atom. The relativistic effects are obviously unavoidable, because it is well known that relativistic corrections will modify energy levels of core electrons substantially for large atomic number atom. There are basically three practical approaches including the relativistic effect within the MSW method. The first is a quasirelativistic theory in which the radial functions inside each atomic sphere satisfy an average Dirac equation that includes the Darwin and mass-velocity corrections, but not the spin-orbit term [16]. This approach has used in this thesis. It is easy to adopt in the calculation and

give important information about energy level shift and charge redistributions compared to the nonrelativistic calculations. The second approach may follow in which the spin-orbit operator is diagonalized in the space of the valence orbitals [19]. In this way, complex wavefunctions that transform according to the molecular double point group are obtained. The third approach is to use the full four-component Dirac formalism throughout [20]. This computation reduces exactly (both in theory and in practice) to the usual nonrelativistic MSW in the limit $c \rightarrow \infty$. This approach could obtain an explicit representation of the small components of the wavefunction, which may be of importance in understanding the crystal field theories, and the double group representation enables a direct comparison with experimental data of transition energy. The adoption of this model is in progress right now.

Chapter 4

Electronic Structure of Si:Er

4.1 Brief Review of Recent Theoretical Work

Since the first discovery of sharp, temperature and host stable luminescence spectra from Er doped Si by H. Ennen et al. in 1983 [21], extensive research has been carried out and abundant experimental data are available. Most of the experimental study focused on fundamental excitation mechanism[22-26], device processing [1,27], high quality film growth [28-30] and ligand enhancement of PL. Surprisingly, there are not as many theoretical investigations as would be expected. There are several possible reasons. The first is due to the large atomic number of Er. Thus, if Er needs to be fully described in the interaction, the required minimum basis should at least include $4f$ orbital. This is not a feasible task for band theory and pseudopotential based calculations. The conventional method is to freeze the Er $4f$ electrons because of the large localization of density of states of these electrons. Secondly, relativistic effect should be included in the calculation to have a full understanding of Si:Er system. The third reason is due to the lack of directly comparable experimental evidence. In order to perform calculations more effectively, it is desirable to have experimental data such as the symmetry around the defect and the lattice location as input, but none of these have been firmly settled by experiment because of complexity of Er defect structure in silicon. On the other hand, the experiment data needs theoretical assistance to be understood. This is one of the major thrust of this thesis.

The first complete SCF calculation of Si:Er was done by Needles et al. in a 32-atom supercell of silicon with pseudopotential and a special k-point scheme [31]. The $4f$ electrons were treated as core states. Total energy was obtained for calculations which put

Er in Er^{3+} and Er^{2+} charge states and in different high symmetry sites, such as tetrahedral and hexagonal interstitial sites, and the tetrahedral substitutional site. It was concluded that Er^{3+} has the minimum total energy when it is in the tetrahedral interstitial position and a $4f^{11}6s^25d^1$ configuration. Si lattice is slightly distorted by the presence of Er, but no Si-Si bonds are broken. The calculation also suggested that there is a t_2 level which has the Er $5d$ and Si sp^3 antibonding character lies high in the gap, about 0.2 eV below conduction band (CB). The calculation also found that Er $6s$ states lie in the Si VB and mix strongly with the Si VB edge.

Another systematically theoretical study about RE ions in semiconductors was performed by Delerue and Lannoo [32] using a tight-binding Green's-function technique. All 13 ions in the RE family were put into the substitutional site in different semiconductors such as Si, InP and CdTe. Again $4f$ states were treated as a frozen core and the electronic configuration of the RE atom was described by $4f^{n+3-m}5d^{m-1}6s^1$, where m is the number of valence electrons. The $4f$ electron population is given by n+3-m. In this model, the oxidation state is simply equal to +m. The $6s^1$ representation can be justified by the fact that the $6s$ state is so extended that its local density of states will be spread almost equally between the valence and conduction bands. However, in this model, the only available state for interaction with atomic s and p states of neighbors in the crystal is $5d$ state. It should not be surprising to see the $5d$ states interact with neighbors. It is worth noting that they found the interactions are so strong that there are no $5d$-derived gap states. The 3+ is the most stable oxidation state in Si, InP and CdTe. The calculation also shows that $4f$ states for all the RE trivalent ions are in the VB. Fig. 4.1 is the reproduction of their calculation for the case of RE ions in substitutional site in Si.

There are two Xα method related calculations on RE ions in semiconductors done by Hemstreet[33] and Saito et al [34]. Hemstreet investigated the electronic states of a substitutional Yb impurity in InP by using a fully-relativistic LMSW-Xα method. He identified a single acceptor Yb level in the gap and the transition energy from the ground J = 7/2 state to the first excited J = 5/2 state is about 1.35 ~ 1.40 eV. These findings are in good agreement with experiment. However, one of the conclusions in this study is that the $4f$ related states are substantially delocalized which is opposite in spirit to experiments.

This difference could be due to the relatively arbitrary radius of the muffin-tin spheres and the fact that no indium atoms are included in the calculation because of the small cluster he chose. Thus no bonding effect between In-P was considered. In Satio's DV - Xα calculation about Er^{3+}, Yb^{3+} substitutional ions in InP, GaP and GaAs, a larger cluster was used which consists a centered Er^{3+} or Yb^{3+}, four nearest-neighbor group V atoms, and twelve next-nearest neighbor of group III atoms. No saturators were used in the calculation even though it had been shown that the dangling bonds could introduce additional defect levels in the gap [35]. The calculated results show a more localized 4*f* level than the results calculated by Hemstreet. The transition energy from $I_{15/2}$ to $I_{13/2}$ for Er^{3+} in InP was estimated as a perturbation, using the self-consistent atomic basis functions of 4*f* orbitals and potentials. The value 0.9 eV was obtained which is in agreement with the experimental value of 0.8 eV, eventhough no spin-orbit interaction was considered.

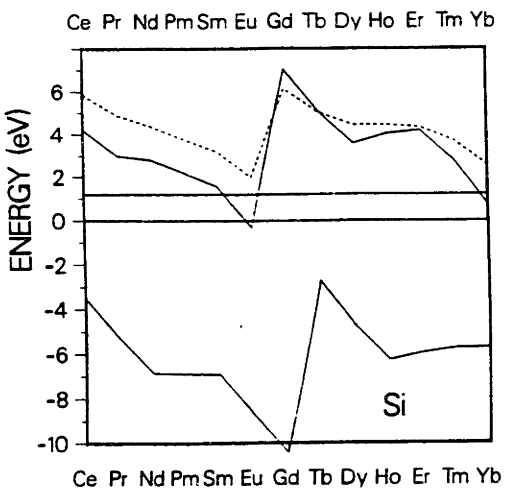

Fig. 4.1 4*f* levels for substitution rare-earth impurities in Si from Ref [32].

4.2 The Electronic Structure of Si:Er by MSW-Xα Method

The strategy adopted in this thesis work is as follows: First, constructing a suitable size pure Si cluster, computing its energy levels to be used as reference. In our case, 38-atom (14 silicon atoms + 24 hydrogen terminators) and 71-atom (35 silicon atoms + 36 hydrogen terminators) clusters are used for the study of tetrahedral interstitial and

substitutional defects, respectively. Second, Er as an isolated impurity is put into the cluster as interstitial and substitutional impurities and redo the SCF calculation. By comparing the energy spectra of the perfect cluster and the defect cluster, one understand the modifications caused by the presence of the impurity. Furthermore, different charge states can be imposed to the cluster, in which the charge is compensated by putting equal amount of opposite sign of charge in Watson sphere. Based on the relative change of energy levels with respect to the pure Si cluster, some conclusions can be made about the lattice location, stable charge state and interaction between impurity valence electrons and Si host. Third, the ligand effect can be investigated by putting different ligands around Er in high and low symmetry forming certain complex structures.

In order to analyze the result for the isolated substitutional erbium impurity in silicon, we have first calculated the electronic structure of the silicon vacancy which is simulated by removing the central atom from the 71-atom cluster. This test to confirm the effectiveness and accuracy of the method and the cluster used in this thesis, and because it is always instructive to picture a substitutional impurity as an atom captured by a single vacancy. It is well established by theoretical investigations that, the dangling bonds on the four nearest neighbors to the vacancy form a single symmetric a_1 and triply degenerate t_2 set of orbitals. The position of t_2 level is in the gap about 0.7 eV above VB, while the a_1 level is about 1.0 eV below the VB. In our calculation, for the 71-atom cluster, the band gap is about 1.15 eV, and the VB width is about 13.5 eV. The t_2 level is 0.62 eV above VB, and a_1 level is 1.05 eV below VB. These levels are in excellent agreement with other researcher's work, which is shown in Fig. 4.2. It is worth mentioning that the 71-atom cluster used in this thesis is by far the largest one ever published in this type of calculation. The test gives us confidence to move on.

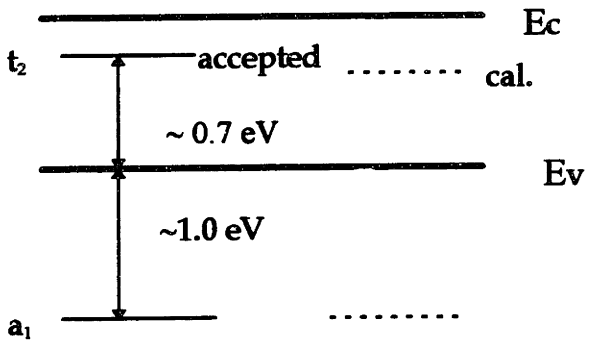

Fig. 4.2 The defect levels of neutral vacancy defect in Si

4.2.1 The Interstitial Er Defect

The 38-atom interstitial cluster ($Si_{14}H_{24}$) gives a gap of 1.6 eV and VB width of 11.0 eV which is in reasonably good agreement with experiment. The high occupied molecular orbital (HOMO) is $3t_1$ and the lowest unoccupied molecular orbital (LUMO) is $5a_1$. From the group theory, the Td group has five irreducible symmetries, two undemensional (a_1 and a_2), one two dimensional (e) and two three dimensional (t_1 and t_2). So the group of the sphere in this Td symmetry can be reduced as $s = a_1$, $p = t_2$, $d = t_2 + e$, $f = t_1 + t_2 + a_1$. After an interstitial Er is introduced in the center with tetrahedral symmetry ($ErSi_{14}H_{24}$), crystal field will cause the *f* electrons to split into t_1, t_2 and a_1 states. So t_1, t_2 and a_1 are the levels of our most interest. There are two notable changes after Er is put into Si. The first is that levels related to 5*s* and 5*p* become core-like levels. They are very deep below the bottom of VB. These levels are called hyperdeep levels. The input potential treats these levels as valence not core levels. Secondly, the almost all *f*-related levels are above VB. From the calculated result, there are 4 levels which have large percentage of Er 4*f* characteristic. They are $6a_1$, $9t_2$, $4t_1$ and $7a_1$ states with 40%, 91%, 97% and 53% *f* electrons respectively. This is shown in figure 4.3 (a) (All the plots in Fig. 4.3 show only the levels above VB since they are the most important ones). However, there are two occupied levels $9t_2$ and $4t_1$ in the CB, indicating that this is not a stable configuration because under equilibrium condition without external field, all the conduction electrons should fall back to levels in the VB or in the gap.

The total number of $4f$ electrons (n) in the levels mentioned above (t_1, t_2, a_1) can be obtained by adding the number of f electrons in each level (occupation x $4f$ percentage) together, which equals to 12.08 (2*40% + 3*91%+3*97%). The crystal field splitting (CFS) is the distance between $4t_1$ and $6a_1$ states, which is about 0.43 eV (see Fig. 4.3 (a)). Finally, the total valence electronic configuration for Er can be obtained in similar way, which is the sum of all the Er related electrons in the energy spectrum. That is:

$$5s^{1.96}5p^{5.28}4f^{12.39}6s^{0.19}5d^{1.09}6p^{0.68}.$$

The Er related electrons in the VB can be described by the electronic configuration:

$$4f^{0.31}6s^{0.19}5d^{1.09}6p^{0.68}.$$

This configuration shows that there are some hybridization among the $4f$, 5d, 6s and 6p atomic orbital when the impurity is placed in the crystal and is responsible by the covalent interaction between interstitial Er and Si host atoms. The difference of these two configuration will be the configuration for the Er related levels in the gap. These configurations agree with the $5d^{1.0}$ by Needls [31]. But $5d^{1.0}$ is in the VB not high in the CB, and it is not a pure $5d$ orbital. The total number of valence electron of Er is about 14.0 but there is no single pure $6s$ level, which means that most of the 6s electrons are promoted to $4f$, $5d$ and $6p$ orbital because its very extended wave function. For example, there are 0.68 $6p$ electrons. But no $6s^1$ configuration is observed. The calculation shows that not only $4f$ electrons but also $5d$, $6s$ and $6p$ electrons are interacting with host silicon atoms.

However, since this configuration is unstable because there are always some electrons in the CB under equilibrium conditions. It is unlikely to be the structure of the Er centers observed in the experiment. To further investigate the charge state of Er center, one electron is removed from the cluster. The new cluster is $(ErSi_{14}H_{24})^{1+}$ and we redo the SCF calculation. One obvious change results from the charge removal is that the occupied CB levels t_1 and t_2 shift down to be in the gap (Fig. 4.3 (b)). With more $4f$ electron in a_1

(from 40% to 76%). The *f* percentage of charge for the t_1 and t_2 remains the same. The crystal field splitting is reduce to CFS = 0.23 eV. The number of 4*f* electrons in the gap is n = 11.78. The new configuration for Er is :

$$5s^{1.96}5p^{5.28}4f^{12.39}6s^{0.24}5d^{1.15}6p^{0.71}.$$

The VB electronic configuration is :

$$4f^{0.61}6s^{0.24}5d^{1.15}6p^{0.71}.$$

This shows that there is a stronger interaction between Er and Si after one electron is removed. Even though the number of 4*f* electrons is the same (12.39) in both charge states (neutral and +1 charge states), more electrons are located in the energy levels in the VB. This means that in the +1 charge state, the number of electrons in the gap of 4*f* states is smaller. Fig. 4.3 (b) shows that there are only 5 electrons in the $4t_1$ level, from the Jahn-Teller (JT) theory, it is an unstable structure because it is an open shell. It will tend to be transformed to lower symmetry under JT distortion, and t_1 level will further split to more levels depends on what lower symmetry is.

Searching for the stable structure continues by taking more electrons off the cluster. Fig. 4.3 (c) and (d) show the energy levels for clusters $(ErSi_{14}H_{24})^{2+}$ and $(ErSi_{14}H_{24})^{3+}$, respectively. All the major *f* levels are still in the gap. The Er 4*f* concentration at $6a_1$ level increases to 88% in the 2+ charge case, while *f* percentage in $4t_1$ and $9t_2$ drops to 70% and 81% respectively. $3t_1$ level is promoted from VB to be in the gap. The charge transfer and promotion increase the hybridization of 4f, 5d, 6s and 6p orbitals. CFS = 0.17 eV and n = 11.46. This gives the Er configuration of $5s^{1.96}5p^{5.34}4f^{12.32}6s^{0.16}5d^{1.15}6p^{0.64}$, and the VB electronic configuration of $4f^{0.86}6s^{0.16}5d^{1.15}6p^{0.64}$. For the $(ErSi_{14}H_{24})^{3+}$ cluster, similar trend is also observed with $3t_1$ level gaining more *f* character. CFS = 0.18 eV and n = 11.13. The Er configuration of $5s^{1.96}5p^{5.34}4f^{12.15}6s^{0.18}5d^{1.42}6p^{0.65}$, and the VB electronic configuration of $4f^{1.02}6s^{0.18}5d^{1.42}6p^{0.65}$. Again, the $(ErSi_{14}H_{24})^{2+}$ cluster is not stable under JT distortion due to the occupation of 4 in the t_1 state. However the half filled triply degenerate $4t_1$ state (occupation is 3) is stable for the $(ErSi_{14}H_{24})^{3+}$ cluster. The 4*f* electron configuration is $4f^{11.13}$. This result suggests that in a sample with just Si and Er atoms such as Er implanted FZ growth Si sample, the possible Er related complex structure is $(ErSi_{14}H_{24})^{3+}$ although

from the experiment, we know that PL intensity from this sample is very weak. The relative PL intensity can be estimated for this structure when spin-orbit interaction is implanted in the calculation by using Slater's transition theory.

The crystal field splitting of 4*f* electrons is 0.18 eV for this cluster. Much less than the Coulomb interaction energy in the order of 10.0 eV and spin-orbit interaction energy about 1.0 eV. We can conclude that the crystal field influence on the 4*f* electron is indeed very small. This small influence can explain the independence of PL spectrum with respect to different hosts. The calculated CFS agrees with the general accepted value of 0.1 eV when a RE ion is placed into a crystal. However, this value is still higher than the experimental data about 0.01 eV to 0.05 eV[3, 10]. The exact value may depends on the interpretations of the PL spectra. For example, the experimental results could be interpreted as the CFS of the two nearest multiplets of $^4I_{15/2}$ states instead of the CFS between top and bottom mutiplets. In the simulation presented here, the calculations do not take account on the multiplet interactions that are more important than the Coulomb interaction among the electrons. We can speculate that this CFS would be reduced further if the spin-orbit interaction is taken into account. It is also worth pointing out that the interaction between Er and the host is stronger in this case, about 1.0 *f* electron, 1.42 5*d* electrons and 0.65 6p electron from Er participate in the bonding / antibonding interaction with VB Si *s*, *p* electrons. These are clearly described by the wavefunction plots in Fig. 4.4 to Fig. 4.7. The plane is (100). In these four plots, Er is in the center, there are four first Si neighbor and six next neighbor. These plotted levels reside in VB and they may not participate in the optical transitions. But they are responsible for the hybridization. As it is discussed in the preceding chapter, it is necessary to have some interactions between *f* electrons and the host in order to break the forbidden electron dipole transition by partially mixing of wavefunctions from 4*f* and VB *s*, *p* electrons. As shown in Fig. 4.3, none of the 4*f* levels in the gap are 100% Er 4*f* character although they are very localized. For example, the contour plot of $5t_2$ is shown in Fig. 4.6. Indeed, the bonding of wavefunctions between Er *f* (center) and Si *p* (4 first neighbors) electrons is observed.

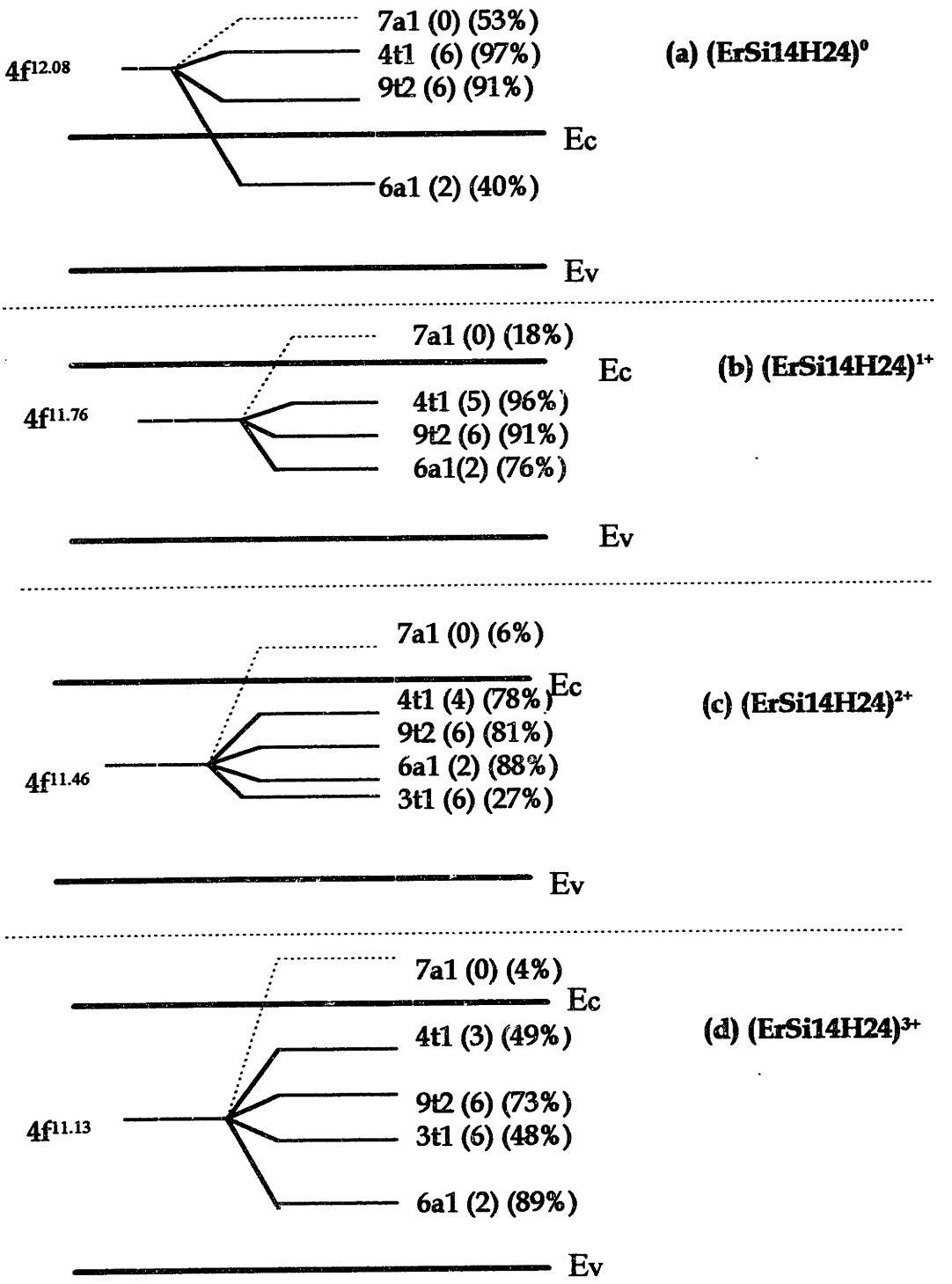

Fig. 4.3 Electronic structure of (a) $(ErSi_{14}H_{24})^0$, (b) $(ErSi_{14}H_{24})^{1+}$, (c) $(ErSi_{14}H_{24})^{2+}$ and (d) $(ErSi_{14}H_{24})^{3+}$. The integer in the ( ) represents electron occupation, the % in the () denotes weight of f electron character in each level. The energy levels are not in scale.

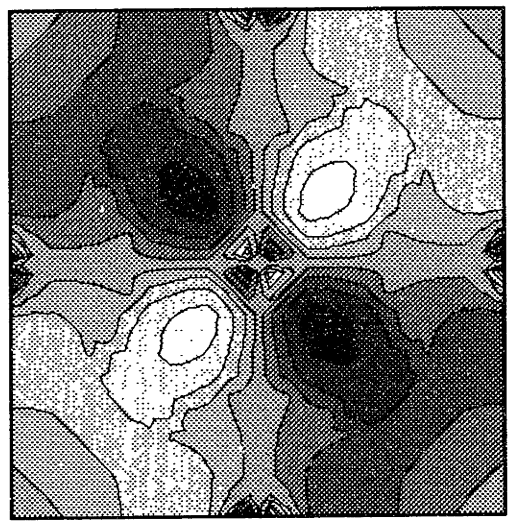

m

Fig. 4.4 The contour plot of 4t2 level

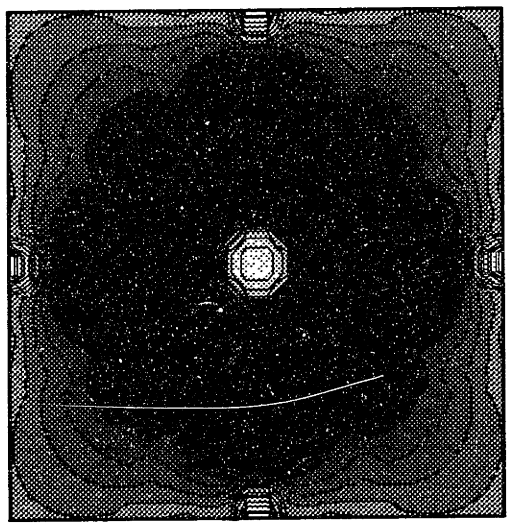

m

Fig 4.5 The contour plot of 2e level

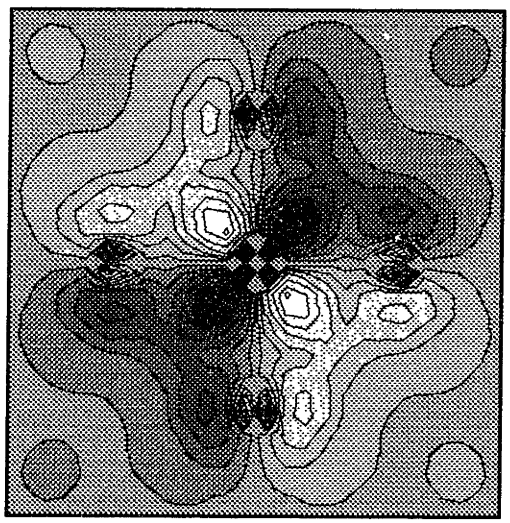

m

Fig. 4.6 The contour plot of 5t2 level

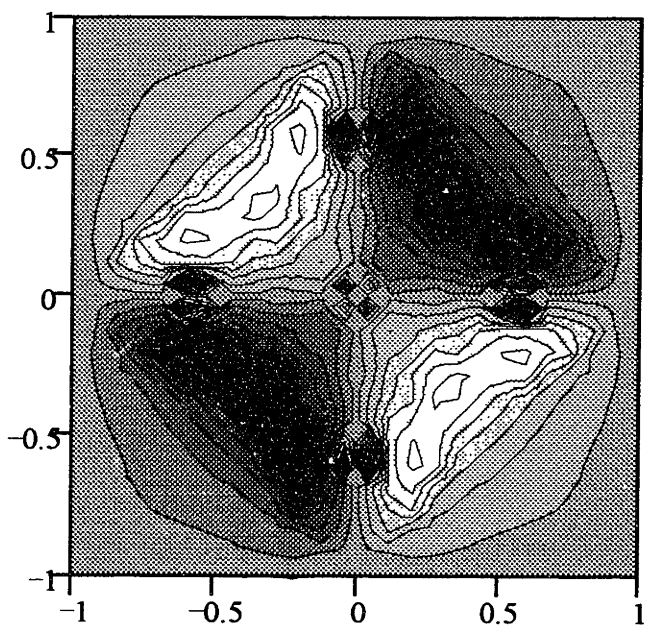

m

Fig. 4.7 The contour wave function plot of 3t2 level

4.2.2 Substitutional Er Defect

We have found that Er in Si assumes a stable 3+ charge state with the $4f^{11}$ configuration in the tetrahedral interstitial lattice site. Next question would be: how about the substitutional site? Based on the experimental evidence, there might be more than one optical center [36]. To answer this question, the 71-atom cluster (Er + 34 Si + 36 H) $ErSi_{34}H_{36}$ was constructed to test this hypothesis. Following the same analysis scheme as that for the interstitial Er, one could show the results that are summarized in Table 4.1.

Table 4.1 Electronic configuration of substitutional Er in silicon

	Electronic Structure of Er	VB Er Configuration	n	CFS (eV)
$ErSi_{34}H_{36}$	$5s^{1.96}5p^{5.35}4f^{12.48}6s^{0.51}5d^{1.24}6p^{0.53}$	$4f^{0.39}6s^{0.51}5d^{1.24}6p^{0.53}$	12.09	0.42
$(ErSi_{34}H_{36})^{1+}$	$5s^{1.96}5p^{5.35}4f^{12.55}6s^{0.38}5d^{1.27}6p^{0.58}$	$4f^{0.41}6s^{0.51}5d^{1.24}6p^{0.53}$	12.14	0.38
$(ErSi_{34}H_{36})^{3+}$	$5s^{1.96}5p^{5.47}4f^{12.47}6s^{0.42}5d^{1.35}6p^{0..56}$	$4f^{1.42}6s^{0.51}5d^{1.24}6p^{0.53}$	11.05	1.12

where in Table 4.1, the first column gives the charge state of each cluster; the second column is the electronic structure of Er in each cluster. The third column shows the VB Er configuration. The last two columns gives the number of 4f electrons and energy of the crystal field splitting respectively.

There are some notable differences between these results and the ones in the case of interstitial Er. Of all the above three configurations, none of is stable because there are always some occupied levels in the CB. So it is unlikely that Er sits in the substitutional position. Second, *f* electrons are split to more levels when Er is in the Si lattice site. For instance, in the case of neutral cluster, there are 6 *f* related levels, they are $8a_1$, $9t_1$, $14t_2$, $9a_1$, $15t_2$ and $10a_1$ states with 7%, 93%, 41%, 34%, 55%, 33% of *f* character respectively. The delocalization of *f* electrons when Er is in the substitutional site could be due to the distortion of Si lattice site.

In general, creation of a substitutional impurity can be described by a three-step process in a simplified manner. (1) Remove a Si atom from its lattice position and creating a single vacancy; (2) put Er atom into the vacancy; (3) bond Er atoms with the silicon neighbors. This process is also verified by comparing the energy levels of $ErSi_{34}H_{36}$ cluster

to that of $V_{Si}Si_{34}H_{36}$ cluster. The schematic energy diagram is shown in Fig. 4.8. The energy levels in the VB for clusters $ErSi_{34}H_{36}$ and $V_{Si}Si_{34}H_{36}$ are very much like each other, except for the cluster $ErSi_{34}H_{36}$, the levels from the addition of Er level are in the CB. It seems that electronic structure of $ErSi_{34}H_{36} = V_{Si}Si_{34}H_{36} + Er$.

The crystal field effect is larger for the substitutional Er than from the interstitial Er due to the large distortion of bonding by inserting the Er into Si lattice site. Has Er bonded with its four nearest neighbors? The contour plots of those levels ($8a_1$, $9t_1$, $14t_2$, $9a_1$, $15t_2$ and $10a_1$) should give us answer. Some of them are shown in Fig. 4.9 to Fig. 4. 11. Where Fig. 4.9 shows the contour plot of wavefunction of state 8a1. and Fig. 4.10 and Fig. 4.11 shows the wavefunction plots for $9a_1$ and $14t_2$ states respectively. The plane is (110) plane which cut through the two nearest neighbors. The other two Si atoms will have the same properties according to the symmetry.

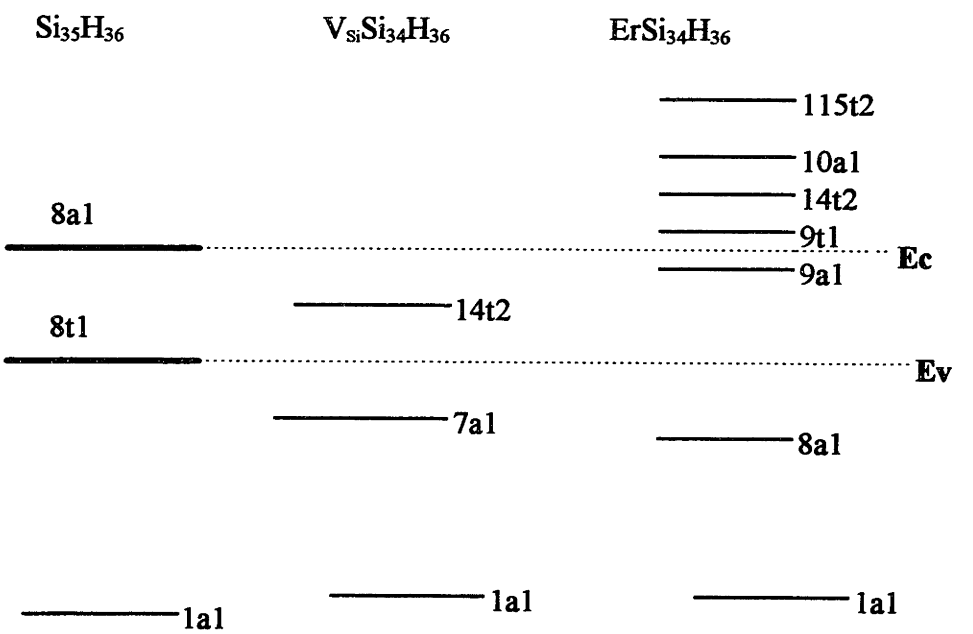

Fig. 4.8 The schematic diagram of substitutional Er defect in Si. The levels in the $V_{Si}Si_{34}H_{36}$ cluster are the defect level related to creation of vacancy. The levels in the $ErSi_{34}H_{36}$ are related to Er 4*f* levels. The diagram illustrates the level ordering only and is not drawn to scale.

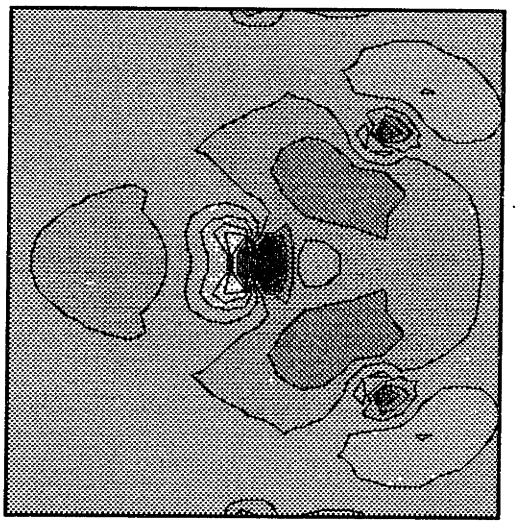

m

Fig. 4.9 The wavefunction plot of 8a1 level in (110) plane. Er is in the center. There is some bonding character between Er 4*f* and Si 2p orbitals.

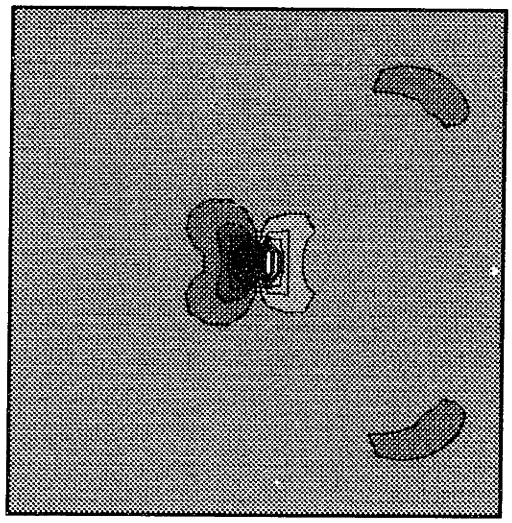

m

Fig. 4.10 The wavefunction plot of 9a1 level in (110) plane showing the nonbonding between Er and Si.

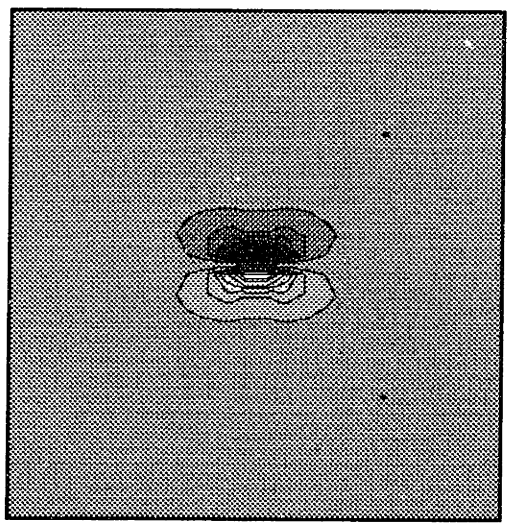

m

Fig. 4.11 The wavefunction plot of 14t2 level in (110) plane, which also shows nonbonding character between Er and Si.

Fig. 4.9 shows that there is some bonding between Er and Si $2p$ electrons for 8a1 level which is expected because $8a_1$ is in the VB. The composition of $8a_1$ is 11% Er of which 59% is $4f$ electrons and 41% are 6s electrons, it also has 21% first neighbor Si p electron, 18% from second neighbor s, p electrons and 4% each from third and fourth shell. The $9t_1$ level is nobonding because it is almost pure f electron (93%). But it is a little surprising that the rest of levels are all nobonding orbitals (Fig. 4.10 and Fig. 4.11). This could reflect the fact that there is no significant first neighbor silicon presence in these states. The $9a_1$ state has only 3% first neighbor Si, 2% for $14t_2$ state, 1% for both $15t_2$ and $11a_1$ states. Therefore, although Er sits in Si lattice site, it does not tend to bond with its neighbors. This is also the reason why the substitutional configuration is unstable. Some delocalization of the f electrons is caused by the bonding effect of the $8a_1$ orbital. The 6s and $4f$ hybridization could cause the f wavefunction to extend outside of $5s$ and $5p$ orbital. The electronic configuration of these two orbitals are $5s^{1.96}5p^{5.24}$. Another reason could be due to the imperfection of calculation because the spin-orbit interaction is not taken into account here, which is expected to make these two core-like levels more localized.

Based on the above theoretical evidence and discussion, it is reasonable to conclude that if Er sits interstitial in a cluster surrounded only by silicon atoms, the cluster will be stable in "+3" charge (Er in $4f^1$ configuration) state when it is in the Td symmetry. This position corresponds to the 5 peaks observed in the PL spectrum. The "n+" charge states of cluster in this thesis means that n electrons will leave the cluster before it stabilizes. These electrons are usually from Er 6s and $4f$ orbitals because they are occupied by the outmost electrons. Substitutional Er is unfavorable under present cluster structure calculation. However, the above discussion is valid only under the condition of no adjoining defects and 0 K temperature. It does not completely rule out the substitutional Er defect. As a matter of fact, in order to enhance PL intensity, Er is always co-doped with other ligands with large electronegativity. Ligands with large electronegativity might be able to interact with Er and stabilize the Si:Er complex structure. There is more detailed discussion about this configuration in section 4.3.

4.2.3 Relativistic Effect

Relativistic effects are important for heavy atoms. Unfortunately, only quasirelativistic calculations are done for this thesis, i.e., only the Darwin and mass-velocity corrections are included in the calculation. Full relativistic correction calculations are in progress. Nevertheless, some improvements have been seen by just taking into account these corrections.

The first improvement is that Er 4*f* electron and hyperdeep states are more localized under relativistic calculation. For the substitutional cluster $ErSi_{34}H_{36}$, the Er percentage in the hyperdeep levels $1a_1$ and $1t_2$ is increased from 98% to 99% and 90% to 94%. While for the interstitial cluster, $ErSi_{14}H_{24}$, Er character for $1a_1$ and $1t_2$ level is also increased by 1% (98% to 99%) and 5% (88% to 93%) respectively. These orbitals are essentially core levels of $5s^2$ and $5p^6$ electrons. The relativistic correction makes them behave more like core levels which gives better shielding to *f* electrons. One direct result of the correction can be observed from the bonded $8a_1$ level. The Er percentage is reduced from 11% to 7% and the *f* character in this level is reduced from 59% to 44%, i.e., less *f* electrons participate bonding with Si host. On the other hand, the *f* electrons in those nobonding levels become more localized, because there are two levels ($9t_1$ and $15t_2$) with predominated *f* character of 89%. No first neighbor Si is seen in these levels. This is summarized in Table 4.2. Charge redistribution is also accompanied by the level rearrangements which are shown in the following (only Er 4*f* related levels):

non-relativistic calculation: 8a1→9a1→9t1→14t2→10a1→15t2→11a1;

relativistic calculation: 8a1→9a1→14t2→10a1→9t1→15t2→11a1;

Table. 4.2 : The change of *f* character before and after relativistic correction for cluster (substitutional Er) $ErSi_{34}H_{36}$.

	1a1	1t2	8a1	9a1	10a1	11a1	9t1	14t2	15t2
nonrela(%*f*)	98	90	11	7	34	33	93	41	55
rela. (%*f*)	99	94	7	3	29	45	89	7	89
net	1	4	-4	-4	-5	-12	-4	-34	34

As can be seen that under relativistic correction, more *f* electrons are concentrated on certain levels instead of spreading out. The net change is about 24%, 0.48 electrons. The electronic configuration in this case is: $5s^{1.98}5p^{5.68}4f^{11.98}6s^{0.46}5d^{1.53}6p^{0.55}$ compared to that of the nonrelativistic case: $5s^{1.96}5p^{5.35}4f^{12.48}6s^{0.51}5d^{1.24}6p^{0.53}$. Unfortunately, these levels are still high in the CB (except 8a1 in the VB and 9a1 in the gap) being an unstable configuration.

Similarly, Table 4.3 summarizes the relativistic effect for 4*f* electron related levels in the cluster (interstitial Er) $ErSi_{14}H_{24}$. These are the levels shown in Fig. 4.3.

Table. 4.3 Relativistic effect for $ErSi_{14}H_{24}$ cluster.

	7a1	4t1	9t2	6a1
nonrela.(%*f*)	53	97	91	40
rela.(%*f*)	68	97	90	25

By far, all these energy levels are obtained by considering only the crystal field and quasirelativistic effects, i.e., the J number in this levels cannot be correctly defined. However, we expect that the introduction of the spin-orbit correction will not change the conclusion too much, because one of the major corrections from spin-orbit calculation is to make *f*, 5*s* and 5*p* levels more localized.

4.3 Ligand Role

The origin of the PL enhancement by coimplanted ligands is still unclear. As mentioned in the introduction, experiments have found that the presence of ligands with large electronegativity greatly enhance the PL intensity [2]. It is speculated by some experimentalists that one of the effects of these ligands is to take away some electrons from Er through the charge transfer between Er and ligands. So it is easier for Er to reach "3+" oxidation state. But there is no direct evidence to support this view.

Because there is a another puzzle regarding structures of Er related optically active centers. One measurement by extended x-ray absorption fine structure (EXAFS) suggests

that there are two possible structures for the centers when Er is co-doped with oxygen. One structure is that Er is surrounded by 6 oxygen atoms in quasi-octahedral symmetry, named active center. Another structure is that Er is surrounded by 12 silicon atoms, named inactive center. The Si lattice is also distorted [39]. These structures are shown in Fig. 4.12. However, this issue is far from settled. There are could be more than one optical active centers, in the form of some complex structures which involves Er, Si and oxygen or other ligands. This structure could also depend on implantation energy, annealing condition and doping species. Thus, it is a formidable task to model the properties of these centers. However, by constructing different simple models, we can try to understand changes caused by the introduction of ligands into the cluster. This understanding will shed some light into the interpretation of more complicated structure.

The first model is simply surrounding Er by 4 oxygens in tetrahedral symmetry for the interstitial Er cluster ($ErSi_{14}O_4H_{24}$). Oxygen is placed in tetrahedral interstitial positions. The most striking feature from this model is that Er *4f* electrons are largely delocalized. Electrons spread out in many levels that are in the gap and VB, there is no single level with high *4f* percentage for this cluster. Almost all the *4f* electrons are mixing with Si, and oxygen s, p electrons in certain degree. Table 4.5 lists properties of the highest occupied (except 8a1) Er *4f* related levels

In the table, levels from 8a1 and 3e are in the gap, the rest is in the VB except that 2a1, 2t2, 1a1 and 1t2 are the hyperdeep levels. It seems that the introduction of oxygen greatly enhances interactions among Er, oxygen and Si atoms. It is known that oxygen in Si without Er and other impurities is not electrically active. Because of the large electronegativity of oxygen, which is about 3.44, while for Er is about 1.24 and 1.90 for Si. Thus, Er and Si are competing for oxygen in the cluster, resulting mixing with each other. It can be estimated from the calculation that there are about 6.8 oxygen 2p electrons in the levels associated with *4f* orbitals. The rest (16-6.8 = 9.2) *2p* electrons are in the VB and mixing with Si.

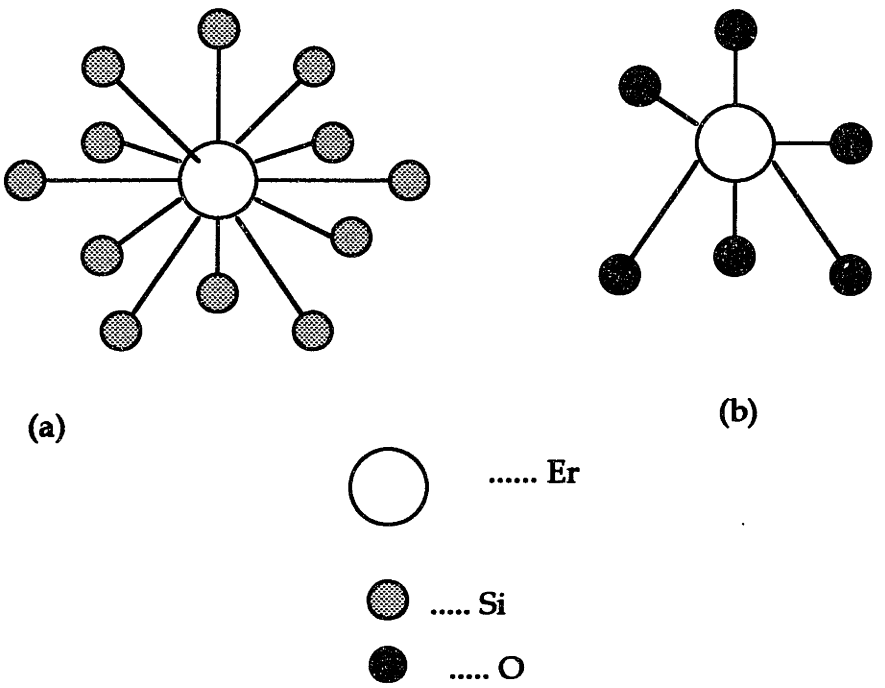

Fig. 4. 12 (a) Optically inactive Er-Si complex; (b) Optically active Er-O complex

Another source of delocalization could come from the absence of relativistic correction. It can be seen from the calculated results that without relativistic effect, the hyper deep level 1t2 ($5p^6$ of Er) is coupling relatively strong with oxygen and Si *s*, *p* electrons. Its composition can be read out from Table 4.5, only 84% 4*f* character, the rest are Si and oxygen. This might cause resonance effect to enhance interactions among Er, O and Si atoms in all the other t_2 levels. Table 4.4 also shows the interaction between Er 5*p* electron and oxygen 2*s* electron at $2a_1$ and $2t_2$ levels. After applying the relativistic correction, the new composition of $1t_2$ becomes 91% Er *f* character, 2% oxygen, 4% Si1 and 3% Si2. The resonance effect is reduced. Accordingly, the oxygen content in those gap levels of $12t_2$, $11t_2$, $10t_2$ is smaller but was not disappear. So mixings of Er-O-Si still prevail in this configuration. This result indicates that the strong delocalization of 4*f* electrons and interactions among Er 4*f* electrons, Si and oxygen *p* electrons are due to the structure of cluster, i.e., these effect are very sensitive to the positions of ligands with

respect to Er as we know oxygen is not electrically active in the pure Si. The calculation also suggests that this (Er with 4 tetrahedral coordinated interstitial oxygen) may not be the Er center observed in the experiment because the large delocalization of *f* electrons will not favor the strong luminescence intensity observed in the experiment.

Table 4.4 The energy levels of $ErSi_{14}O_4H_{24}$

	occup.	Er 4f (%)	oxygen (%)	Si1 (1st shell, %)	Si2 (2nd shell, %)	Si3 (3rd shell, %)
8a1	0	52	20	1	3	2
12t2	6	69	7	3	4	3
4t1	6	75	0	1	3	5
11t2	6	3	19	3	4	6
4e	4	0	16	1	4	17
3t1	6	18	2	0	1	17
10t2	6	7	8	0	2	20
3e	4	1	36	7	4	12
9t2	6	18	22	10	18	5
8t2	6	8	9	20	12	20
7a1	2	34	34	12	2	10
2t2	6	8	84	0	2	0
2a1	2	1	83	2	6	0
1t2	6	82	6	6	3	0
1a1	2	97	0	1	0	0

To further test the theory, four different calculations were performed. First, hydrogen and Li atoms are put into the former oxygen positions ($ErSi_{14}H_4H_{24}$ and $ErSi_{14}Li_4H_{24}$). The purpose of these calculations is to test how interaction evolves from ligands without *p* electrons such as H, Li to those with *p* electrons like oxygen and

fluorine. As it is known that H and Li behave totally differently in the Si. Li is a shallow donor in the Si. But properties of H in Si are still not completely defined. Second, Er was removed from the cluster ($Si_{14}O_4H_{24}$) to see how oxygen interacts with Si. Third, four oxygen atoms are put into the substitutional position replacing the first shell of Si atoms. Forth, electrons are taken away from $ErSi_{14}O_4H_{24}$ cluster.

When 4 interstitial hydrogen atoms are introduced into the cluster as ligands, it is an open shell structure under T_d symmetry (the highest level is unfilled and the structure is not unstable). Each H gains 0.22 electrons and the final total charge for H is 1.22. Part of these extra electrons could come from Er. This is understandable because the electronegativity of H is 2.2, larger than that of erbium (1.24) and smaller than that of oxygen (3.4). The calculation shows that there is no interaction between Er and H at the hyperdeep level $1t_2$ although there is some interaction between Er and Si at this level. The whole spectrum of the electronic structure looks like the one without any ligands ($ErSi_{14}H_{24}$). There are three $4f$ dominated levels split from f orbitals, $4t_1$, $9t_2$ and $7a_1$. These levels are in the gap. The gap levels $7a_1$ and $10t_2$ show some hybridization of Er $4f$, H s and Si p electrons. But the majority of H electrons reside in VB with the 6a1 state. The Li ligand gives a different result. Li has a very small electronegativity about 0.98. After 4 Li atoms replace oxygen, Li lost about 0.42 electrons, while Er gains about 0.25 electrons comparing to the cluster of $ErSi_{14}H_4H_{24}$. The total charge of Er for above these clusters is 67.53 ($ErSi_{14}O_4H_{24}$), 67.64 ($ErSi_{14}H_4$-H_{24}), 67.72 ($ErSi_{14}H_{24}$) and 67.89 ($ErSi_{14}Li_4H_{24}$). These values can be reduced further by about 0.2 electrons if relativistic correction is applied. For instance, the Er charge for cluster $ErSi_{14}O_4H_{24}$ given by relativistic calculation is 67.39. The absolute value might not have significant meaning here because it is obtained by integrating charge density in the Er sphere. However, the radius of sphere is determined by some optimal empirical method allowing some overlapping between the Er sphere and spheres around the Er [17]. Thus the total charge could dramatically by just changing the radius of sphere. The large the radius, the large the overlap and the less the charge for Er. But the trend seems to be clear here. Ligands with large electronegativity do take away more electrons from erbium. Other features of Li ligand in the cluster are similarly to those of $ErSi_{14}H_4H_{24}$. There are three very high

percentage $4f$ dominated levels ($t_1 + t_2 + a_1$). But the cluster are very unstable because these levels are about 1.0 eV above CB. The 2s electron of lithium are so mobile that no level has over 10 % concentration of 2s electron. It seems that we can conclude that existence of $2p$ electrons from ligand atoms does help interaction between Er $4f$ and $2p$ electrons.

The cluster of just oxygen and Si ($Si_{14}O_4H_{24}$) is quite simple. It is an open shell structure. Most of the highest occupied levels are oxygen $2p$ electrons with some Si $2p$ electrons. Most of Si $2p$ electrons are in the VB. This results tell us that when Er is implanted, major interactions will happen between Er and oxygen $2p$ electrons, especially Er $4f$ levels since they are about the same energy levels as oxygen 2p electrons. Combined with the discussion above, it suggests that a large electronegativity ligand (O, F, H) helps stabilize the structure, i.e., the total energy of the system is lower due to the interaction among these atoms. While smaller electronegativity ligands (Li) will make the structure unstable. Since hybridization and charge transfer are easier taking place in the system with large electronegativity.

The third cluster is that 4 oxygen substitute 4 first shell of Si atoms. This cluster is use to test the possibility of oxygen in substitutional position. Without relativistic correction, there are very strong interaction between Er 5p and oxygen 2s electrons at the hyperdeep levels of $1t_2$ (71% Er 5p + 22% oxygen 2s) and $2t_2$ (25% Er 5p + 68% oxygen 2s). After performing the relativistic calculation, the composition of $1t_2$ changes to (94% Er 5p + 3% oxygen 2s), and $2t_2$ changes to (4% Er 5p + 87% oxygen 2s). Again, this result manifests the importance of relativistic effect in such heavy ion cluster. In contrast to the cluster with 4 interstitial oxygen, three dominant f levels are strongly visible (a_1 has 73%, t_1 has 98% and t_2 has 62% f characters). However, some mixings of Er-O-Si still exist in some levels. Er $4f$ electrons in this cluster are more localized than the cluster with oxygen in interstitial position.

The last test in the series is to take electrons off the neutral $ErSi_{14}O_4H_{24}$ cluster to see if it can increase the localization of f electrons. One and three electrons were striped away from the cluster separately. Regular and relativistic calculations have been performed regarding to these configurations. However, there is no miracle here. Er $4f$

electrons are still delocalized in most orbitals except 3t1 level with over 90% of *f* character.

Thus the calculations show that interstitial oxygens in interstitial Er cluster is unlikely the center observed in experiments that gives strong PL in the Si:Er:O sample, although the structure with 4 substitutional oxygen ligands has better 4*f* characteristic. Even if such a complex structure exists in the Si:Er:O sample, PL intensity from this center will be very weak since *f* electrons are delocalized. The strong interaction will broaden the lines in the PL spectra.

It is also demonstrated by experiments that the Si:Er sample doped with fluorine gives much more stronger light than that in oxygen co-doped Si:Er sample at the low temperature [37]. In order to see if calculations can give some insight about the fluorine behavior in the cluster, similar calculations can be performed by putting 4 fluorine atoms into interstitial position ($ErSi_{14}F_4H_{24}$). The electronic structure shows some different features from the oxygen cluster. The first is that Er 4*f* electrons related energy levels are more localized than their counterparts in $ErSi_{14}O_4H_{24}$ cluster. Second, some occupied levels lie in the CB while in the cluster with oxygen, all levels are below CB. But the major difference is that even after the relativistic correction, there is still very high percentage of fluorine content in the hyperdeep levels of $1t_2$ and $2t_2$. This result is in contrast to the case of $ErSi_{14}O_4H_{24}$ cluster where relativistic calculation localizes the Er core electrons and greatly reduces the presence of oxygen in $1t_2$ level to only about 2%. For this cluster, even after relativistic calculation, the composition of $1t_2$ level are 76% Er 5*p* and 17% F 2*s* electrons. For $2t_2$ level, it is 18% Er 5*p* and 78% F 2*s* electrons. It is surprising to see that there is no bonding between Er and F at such a deep level in the VB as shown in Fig. 4.13. The figure clearly shows the non-bonding character between Er and oxygen. On the other hand, the $1t_2$ level of $ErSi_{14}O_4H_{24}$ cluster shown in Fig. 4.14 indicates a strong bonding between Er and oxygen. For both figures, the plane of contour plot is (110).

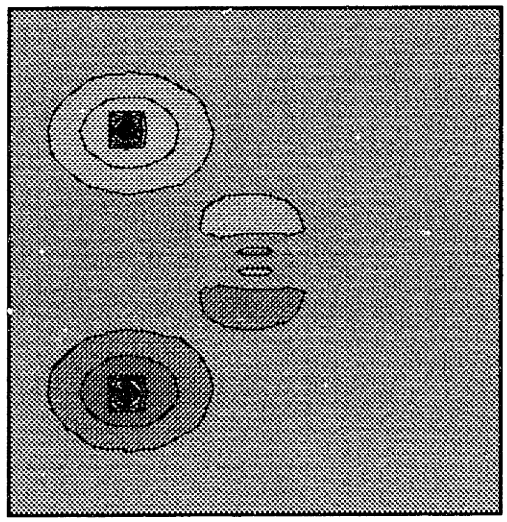

m

Fig. 4.13. The contour plot of $1t_2$ level for $ErSi_{14}F_4H_{24}$ cluster shows the non-bonding character between Er and F. Er is in the center position.

This study suggests that 4 fluorine atoms tetrahedrally surround Er is an very unstable configuration. For the hyperdeep levels, Er and F do not intend to mixing together. On the other hand, oxygen cluster is stable because of the bonding effect. The unstable T_d symmetry with fluorine ligands will tend to lower its symmetry and become stabilized. Fluorine is still probably in the interstitial position because the total energy calculation shows the interstitial F in silicon gives lowest energy [38]. Some simulation studies of Er-F reaction suggest that Er is surrounded by 3 fluorine (ErF_3) [37].

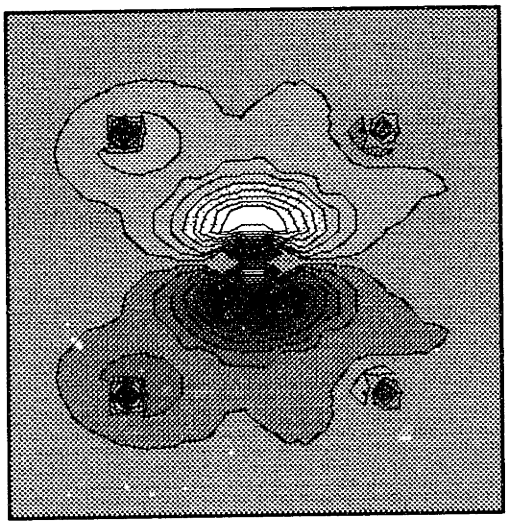

m

Fig. 4.14 The contour plot for 1t2 level of $ErSi_{14}O_4H_{24}$ cluster. Er is in the center

Thus, a C_{3v} symmetry cluster ($ErSi_{14}F_3H_{24}$) with 3 interstitial fluorine is constructed for the new simulation. Er is still in the center of symmetry. It takes at least 10 times more effort to complete the calculation due to the lower symmetry, more levels and small energy intervals between each levels. It is very easy to miss one level during the calculation. So it is very important to use very small energy increment when energy search calculation is performed. Table 4.5 lists properties of those 4*f* electron related levels. They are the highest occupied states. ($21a_1$ - $17a_1$). For these levels, Er % means 4*f* character. F % denotes sum of fluorine s and p character (mainly p). Si % is the sum of all the percentage from all the shell in the cluster. Also in the table are the hyper deep levels (2e - $1a_1$). Where Er % in this case denotes the Er 5*p* electron concentration, F % tells the F 2*s* concentration. Si % has the same meaning.

Table 4.5 Electronic structure of $ErSi_{14}F_3H_{24}$

	Occupation	Er (%)	F (%)	Si (%)
21a1	0	28	0	15
19e	1	17	1	19
20a1	2	17	0	18
19a1	2	45	0	9
5a2	2	98	0	1
18e	4	97	0	1
17e	4	75	0	6
18a1	2	74	0	4
17a1	2	21	1	13
2e	4	83	7	7
3a1	2	86	2	9
2a1	2	2	91	1
1e	4	6	87	2
1a1	2	97	1	0

The Table 4.5 shows that under C_{3v} with 3 interstitial fluorine configuration, Er 4*f* electrons are very localized. Since there are many more levels in the lower symmetry configuration, there are still some levels with some degree of mixing with Si and F. but most of the levels are not interacting with Si and F. As an example, contour plot of 2e state is shown in Fig. 4.15. It also indicates that the interaction between erbium and nearest neighbor silicon is very weak.

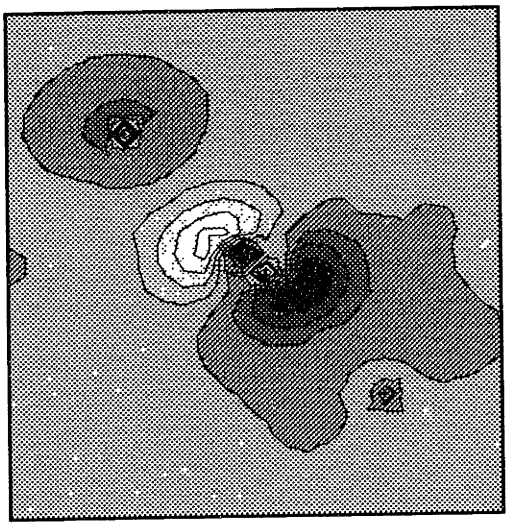

m

Fig. 4.15 The contour plot of Er - F nonbonding (2e state). Er is in the center. F is at up left corner. (110) plane.

The exact relation between this configuration and the reason that fluorine coimplanted Si:Er sample gives strong PL is unclear at this moment. But it seems that Er 4*f* electrons preserve much of their atomic character with 3 fluorine in C_{3v} symmetry , and also with some mixing with host atoms so that admixture of wavefunction is enough is break the forbidden transition. This may partially explain the high intensity coming from fluorine coimplanted Si:Er samples. But it is very difficult to draw any firm conclusion at this moment regarding the role of fluorine and oxygen ligands during the optical transition. We can only suggest that these ligand will cause larger mixing between Er and Si comparing to the case without ligands. We are not sure whether this larger admixture of wavefunction gives enhancement of light emission or not. As it is discussed in chapter 1, the light emission from forced electric dipole transition is very weak due to the small weight of nonparity wavefunction. However, this study shows that oxygen and fluorine prefer different symmetries and it is in agreement with the experimental evidence that the PL spectrum for oxygen doped sample and fluorine doped sample are different [2].

To complete the last step of theoretical investigation, it should be very interesting to see how the electronic structure changes when oxygen and fluorine atoms are put into the substitutional Er cluster. The procedures are the same as that in interstitial Er. First, 4 oxygens and fluorines are put into cluster in Td symmetry. Second, since when erbium sits substitutionally in the cluster, it can easily accommodate up to 10 ligands around it (4 in Td symmetry and other 6 in octahedral symmetry) without knocking out any silicon neighbors. It is a more open structure than that of interstitial erbium configuration. This are the two basic models used in the calculation. These are very large and time consuming calculations, the cluster size for 10 ligands is 81 atoms. 8 different calculations are performed for this study, i.e., 4 and 10 oxygens and fluorines are put into cluster separately. Both regular and relativistic effect calculations are done. As we have discussed and demonstrated the importance of relativistic correction before, all the following calculation results have been relativistic corrected. We have demonstrated that relativistic correction will reduce the interaction between Er $5p$ core and ligand $2s$ electrons in general. Results are more accurate.

Indeed, the results are interesting and surprising. It was shown in the last section that when Er substitutes Si without any other ligands, the cluster is unstable and no bonding occurs between Er and Si. The $4f$ electrons are quite large delocalized. As 4 oxygens are introduced in the substitutional cluster, it becomes a stable one. There are three levels in the gap, $11a_1$, 8e and $10t_1$. However, only $11a_1$ level is $4f$ orbital related and has 39 % of it and 12% oxygen $2p$ character. It is antibonding. The majority of $4f$ electrons are in the VB and scattered, mixing with oxygen and silicon $2s$, $2p$ electrons, resulting in a large crystal field splitting about 2.0 eV. Some of the levels are summarized in Table. 4.6 and readers can get a taste of what they look like. The Si column only refer to the percentage of first shell silicon atoms.

For the model with 4 interstitial fluorines, it is an unstable structure which should not be to surprised to see it because we have shown that fluorines do not like to be arranged around Er under Td symmetry. Er $4f$ electrons are more localized compare to that of oxygen in the cluster, but still diffused compared to the atomic configuration of Er.

Thus, neither 4 oxygen nor 4 fluorine are likely to be the structure in the Si:Er sample coimplanted with these ligands.

Table 4.6 Properties of some levels after 4 oxygens in Si:Er, Er is substitutional.

	Gap level	VB level	Er (%)	O (%)	Si (%)
11a1	x		39	12	10
8e	x		0	17	2
10t1	x		0	16	2
17t2		x	7	4	1
8t1		x	34	0	2
7t1		x	62	1	1
10a1		x	34	4	0
14t2		x	8	1	7
8a1		x	12	0	11

Much of the fun and interesting features come from the analysis of 10 oxygen in the cluster. These 10 oxygen atoms are placed equal distance from Er, but they can be treated as two groups (4 Td and 6 octahedral) because the surroundings for each of these two groups are different . The most striking feature is that in contradiction to the cluster without oxygen and the one with 4 oxygen, the 4*f* electrons of Er become very localized with a crystal field splitting of 0.081 eV, which is about the same as the value observed when RE ions are in ionic materials. The second unexpected feature is that there is no level in the gap. The three major *f* related levels ($t_1 + t_2 + a_1$) are about 3.0 eV below VB. A schematic diagram of electronic structure of this cluster is shown in Fig. 4.16. However, the number of 4*f* electrons for the three characteristic *f* levels $10a_1 + 6t_1 + 16t_2$ is only 9.0 (Fig. 4.16), which is 2 electrons short of $4f^1$ configuration. This can be attributed to the different oxygen roles from the two oxygen groups.

As can been seen in Fig. 4.16, there are three more levels ($11a_1$, $13t_2$ and $8a_1$) having some mixings of Er 4*f* and oxygen 2*p* electron., which have 0.32, 2.22 and 0.78 4*f*

electrons receptively. Fig. 4.17 shows that there is some bonding between Er and oxygen in the 13 t_2 level. While for the $8a_1$ level, Fig. 4.18 shows that there is no bonding between Er-O in the (100) plane. But Fig. 4.19 tells us that there is bonding between erbium and oxygen in the (110) plane. We also observed that there is weak bonding between Er-O in (100) for 11a1 and 10a1 states but there is no bonding between them in the (110) plane. This different bonding characteristic means that the two different groups of oxygen play different roles in the cluster. The oxygen from Td group interacts much more strongly with Er and thus a stronger bonding with Er than those oxygen from octahedral group. It is also possible that some oxygens may like to bond to silicon instead of Er because the distance between oxygen and silicon is not the same for all oxygens. i.e., there is a competition between erbium and silicon for oxygen. The one that is closer to oxygen will get it. Also the environment for these two groups of oxygens is different. Based on this information, it is possible to conclude that these 6 oxygen ligands in octahedral symmetry are responsible for the localization of *f* electrons and the stronger optical transition. This is in agreement with the EXAFS conclusion of the structure of optically active Er centers.

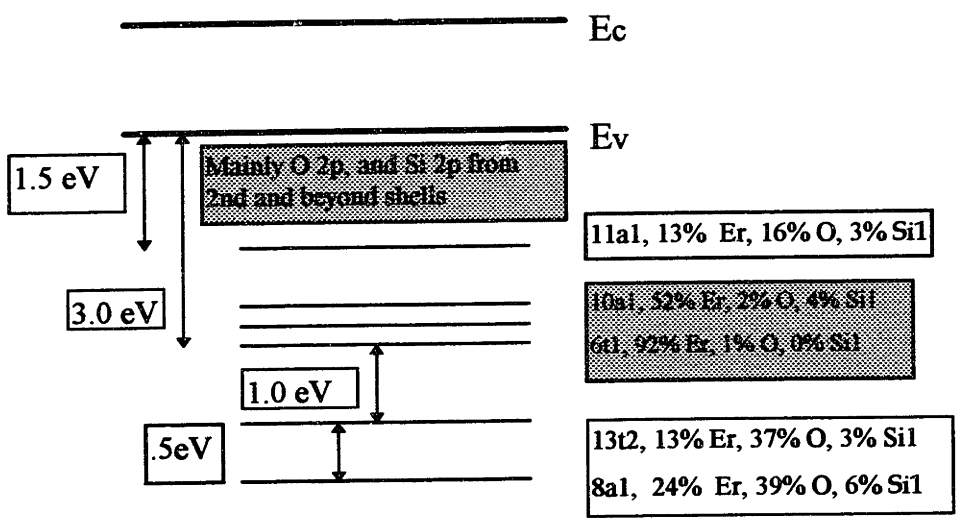

Fig. 4. 16 Schematic diagram of electronic structure of 10 oxygen in substitutional Er

Fig. 4.16 is in agreement with the calculations done by Lannoo et al. that Er 4*f* levels are in VB when Er is in the substitutional position [32]. But there is no ligand in Lannoo's calculation and 4*f* electrons are assumed 100% localized (core). So the interpretation could be very different. It is well known that there are at least two necessary fundamental conditions needed to be satisfied simultaneously in order to have PL from the Si:Er sample. The first is that the RE ions still retain atomic like structure under the influence of crystal field; second is that there are must be some degree of mixing of wavefunctions between 4*f* electrons and electrons from other element in the crystal to enable the transition. It is not clear whether this center will give better light emission.

The 10 fluorines cluster does not show the same good result as that in 10 oxygen cluster. There are still some occupied level above CB, indicating an unstable structure. This will also support our conclusion that fluorine tends to stay in lower symmetry. The only interesting feature in this cluster is that all the all 4*f* electrons are concentrated on the first 6 occupied levels. Some of them are Er-F-Si mixings. No 4*f* electrons are below these levels.

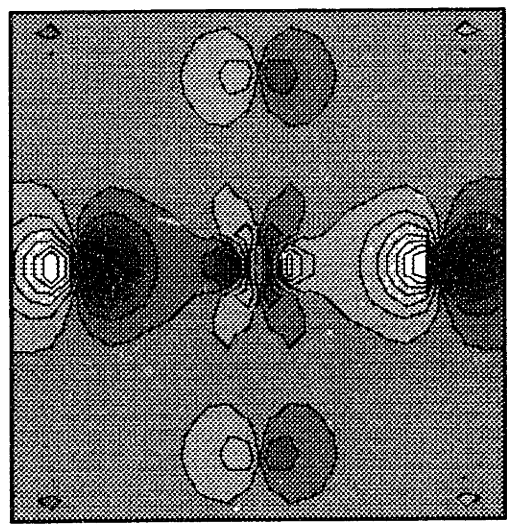

m

Fig. 4.17 the contour plot of 13t2 level in (100) plane. Er is in the center

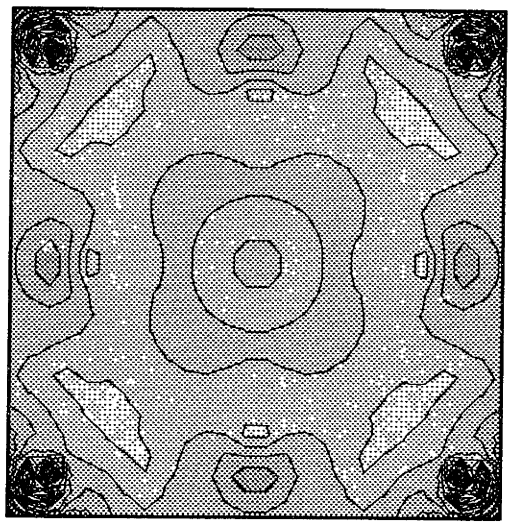

m

Fig. 4.18 the contour plot of 8a1 level in (100) plane. Er is in the center

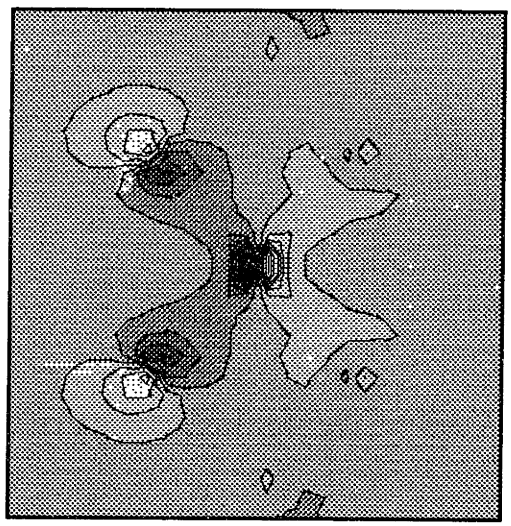

m

Fig. 4.19 the contour plot of 8a1 level in (110) plane. Er is in the center

As a summary of the theoretical work, we have tested thoroughly all the possible structures of Er and ligands (O, F) in Si under T_d symmetry. In special case, we tested interstitial Er with 3 fluorines under C_{3v} symmetry. The simulation shows that without the presence of any ligands, i.e., isolated Er in silicon, erbium prefers to sit in interstitial

position and the cluster is in "3+" charge state with $4f^1$ configuration. There is some hybridization between *f* electrons and silicon 2*s*, 2*p* electrons. The presence of ligand in the cluster makes interpretation of electronic structure more complicated because of the increase of variables. But based on the calculation, it is reasonable to make some suggestions: interstitial oxygen under T_d symmetry is a possible configuration for substitutional Er. There are maybe 6 or more oxygen surrounding Er atoms. Under the influence of oxygen, Er transfers from the interstitial position to substitutional site. One of the function of oxygen is to stabilize the substitutional position of Er through bonding interaction in some levels. It also help localize *f* electrons and a smaller CFS when Er sits substitutional lattice site. It is possible that this center is optically active since the resembles the structure determined by the EXAFS measurement. The ligand field effect is very small. The splitting energy is about 0.1 eV.

In the case of a real sample, we can expect that at least there are two kinds of centers. One is interstitial, the other is substitutional surrounded at least by 6 oxygens. This can be justified by the fact that implantation of Er usually causes large lattice damage. Even after annealing, the concentration profile of oxygen and erbium is very non-uniform. Some Er are surrounded by more oxygens and others by fewer or none. The calculation would suggest that Er has more than one lattice site in silicon. This is in agreement with the backscattering angular scanning experiment done by Tang et al that the ratio of substitutional Er to interstitial Er is 4:1. For the fluorine ligand, the calculation shows that it does not like to be under Td symmetry. It always tends to go to lower symmetry such as C3v when Er sits interstitial. The substitutional Er for lower symmetry of fluorine is in progress. This different symmetry preference of oxygen and fluorine ligands may explain the different characteristic of PL spectra for oxygen and fluorine samples.

Chapter 5

Photoluminescence Study of Erbium Centers in Silicon

5.1 Introduction

It is necessary to maximize light emission from erbium centers in silicon so that Si:Er material can compete successfully with other optoelectronic materials such as III-V semiconductors. Studies by Michel et al showed that only about 10% erbium centers in silicon are optically active [40]. Obviously, there is still a large room for further improvement.

There are basically two approaches to maximize light output. The first is to incorporate maximum amount of Er into Si without precipitation and get as much as possible optically active Er. The second is to reduce the thermal quenching. There are several ways to incorporate Er into Si. The most common used method is ion implantation. Another possible method is CVD or MBE. But there is only one study regarding MBE growth of Er in Si [28]and more studies on CVD or MBE growth of Er in GaAs [26, 29]. Most of previous studies concentrated on implanted samples [2,40], i.e., Er is incorporated into silicon through high energy (MeV) or low energy (kev) ion implantation process. The high energy implantation usually causes large lattice damage, and subsequent high temperature annealing is necessary to reduce damage and make the erbium center optically active. The shallow implantation will not damage the lattice as much as the deep implantation, but high temperature annealing is still required to remove the implantation damage. It was shown from the previous studies that fluorine coimplanted samples give the best light emission at low temperature (4 K) for deep implanted samples [37]. One the other hand, there are at least two advantages of using

CVD or MBE as doping method. The first is that there is no lattice damage (strain still exists in Si:Er layer) to samples grown by CVD. Thus, no annealing is required and thermal budget is reduced. The second is that it is possible for CVD and MBE to incorporate as much as $1x10^{20}$ cm^{-3} Er into the silicon without precipitation, and it is possible that the total amount of optically active Er centers are also increased. Studies show that the PL intensity does not increase as more erbium is incorporated into the sample due to the formation of precipitation [28]. Optimal growth condition has to be determined before get more light of out the CVD growth sample.

It is also possible to choose suitable ligands co-doping with Er to maximize the number of optically active centers. It has been known for years that light emission can be enhanced significantly by ligand coimplantation with Er [2]. The enhancement mechanism is still not completely understood. The last chapter shows that oxygen ligand can help stabilize the substitutional erbium defect and localize *f* electron under Td symmetry. It was concluded that the optically active center may have more than 6 oxygen atoms around Er when Er sits in the substitutional lattice site. Fluorine ligand tends to be stable in lower symmetry with 3 fluorine around Er when Er is an interstitial defect. Optimal process and better design of the LED may provide additional improvement of light emitting efficiency from Er centers in Si.

Thermal quenching can reduce the PL intensity by an order of 3 when temperature is increased from 4 K to room temperature [37]. It is very necessary to understand the excitation and deexcitation mechanisms of the light emission in order to minimize the quenching effect. The PL study (intensity, rise and decay time) is one of the most powerful techniques for this research. It can provide valuable insight information of Si:Er optical transition. This is the focus of this chapter. The power and temperature dependence of PL intensity and lifetime are going to be discussed. By combining with other techniques such as spreading resistance measurement, electroluminescence (EL), cathode luminescence (CL) and hall effect measurement, a more clear picture of the light emission mechanism can be achieved. Some of spreading resistance and other measurement results will be refereed in this chapter, but the detailed study is beyond the scope of this thesis.

5.2 Experimental Setup for PL, Rise and Decay Time Measurements

The experimental setup of rise and decay time measurements is shown in Fig. 5.1. A 488 nm Argon laser is used as the excitation source, because the photon energy is greater than the Si bandgap (1.12 eV) to generate carriers in Si:Er. The sample preparation is by ion implantation of Er and ligands into Si wafers (p-type and n-type). Subsequent high temperature (800°C to 1000° C) annealing in the furnace is used to reduce the implantation damage. Detailed processing conditions for each sample are shown in Appendix A. Samples are placed in a cryostat capable of varying the temperature between 4.0K - 300K. Filter 1 is an infrared filter which eliminates the low energy emission lines from the Ar laser so that those lines would not be reflected to interfere with the emission from the sample. Filter 2 is a 1.54 μm wavelength band filter. Er light signals are detected by a fast InGaP detector. The detected signals are amplified by a current amplifier and finally the signals are recorded by a HP digital scope. A beam chopper was used to modulate the laser light, which can be used as the reference frequency for the scope. The are two lens at each side of the chopper. The purpose of these two lenses is to make the beam spot as small as possible, so that the delay for rise and decay signals is negligible. The frequency is usually set to about 80 Hz. All the scanning controls and data collection are done by a computer. The overall time resolution of the system is about 3 μs.

The setup for PL study can be found in detail in somewhere else and will not be discussed here [37]. Some important information can be obtained by analyzing the PL spectrum, such as the crystal field splitting and the relative defect densities. For example, Table 2.5 shows that if Er is under T_d symmetry crystal field, there should be five peaks in the PL spectrum. If it is under C_{3v} or lower symmetry, there should be 8 peaks in the spectrum. This is in agreement with the experiment. However, the high resolution spectrum shows that there are many smaller peaks between 5 major peaks at very low temperature like 4 K [2]. Some of the peaks may come from more than one Er centers and others may come from Er processing related defects. So it is difficult to make direct comparison between theory and experiment.

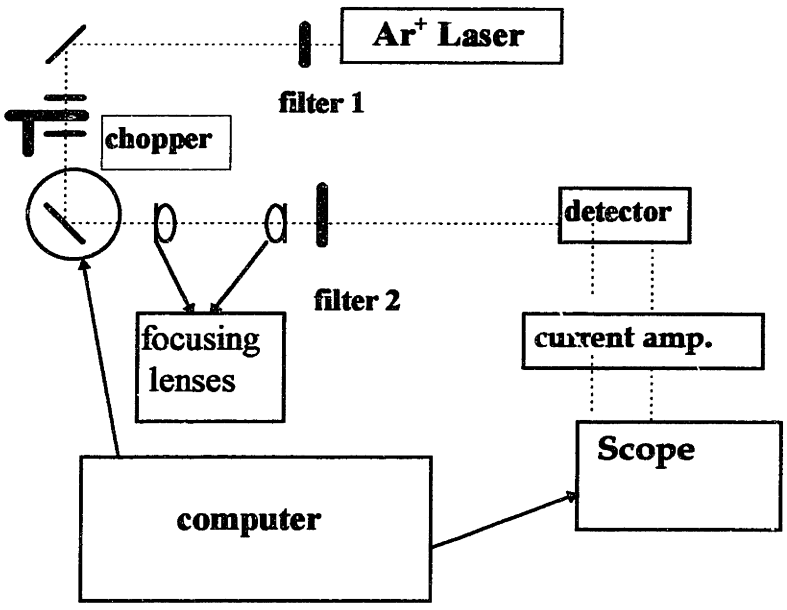

Fig. 5.1 A schematic setup of rise and decay time constants measurement

5.3 Results

5.3.1 Temperature and Power Dependence of PL Intensity

Fig. 5.2 and Fig 5.3 show the temperature dependence of PL intensity for sample D (p-type) and sample I (n-type) respectively (detailed sample conditions refer to appendix A). There are two curves for each plot, one is for high power (1.5 W) and the other is for low power (0.07 W). These plots show the characteristic of PL versus 1/T and T. The PL vs. 1/T plot is the standard plot for thermal quenching, since this plot can be fitted by a double exponential function which gives two activation energies for the thermal quenching [41].

$$\frac{I}{I_0}=1+a\exp(-E_1/KT)+bExp(-E_2/KT) \qquad (5.1)$$

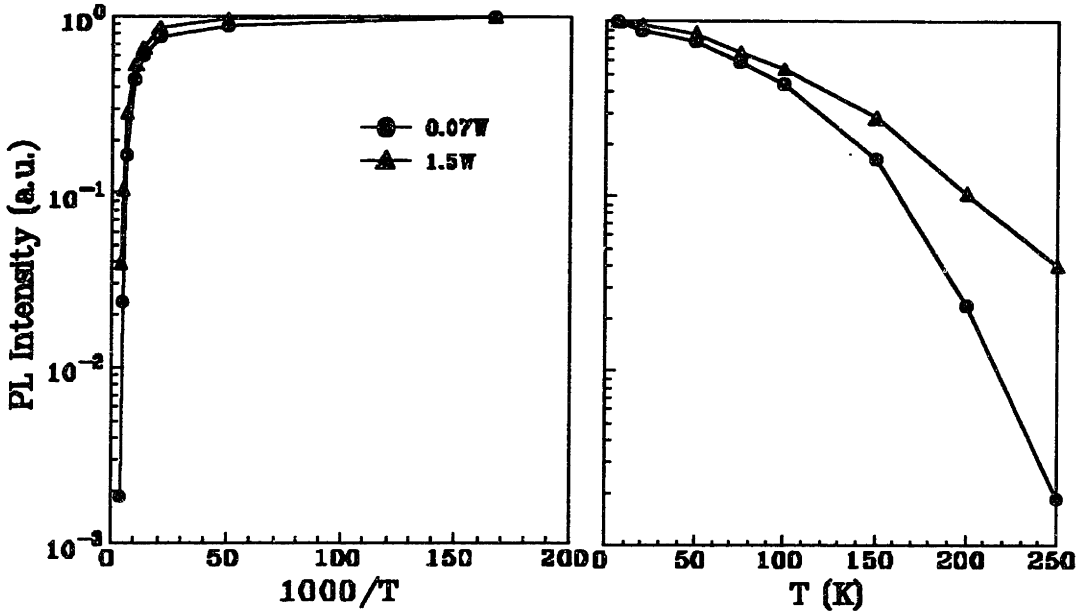

Fig. 5.2 Thermal quenching behavior for sample C (p-type). (a) PL vs. T; (b) PL vs. 1000/T

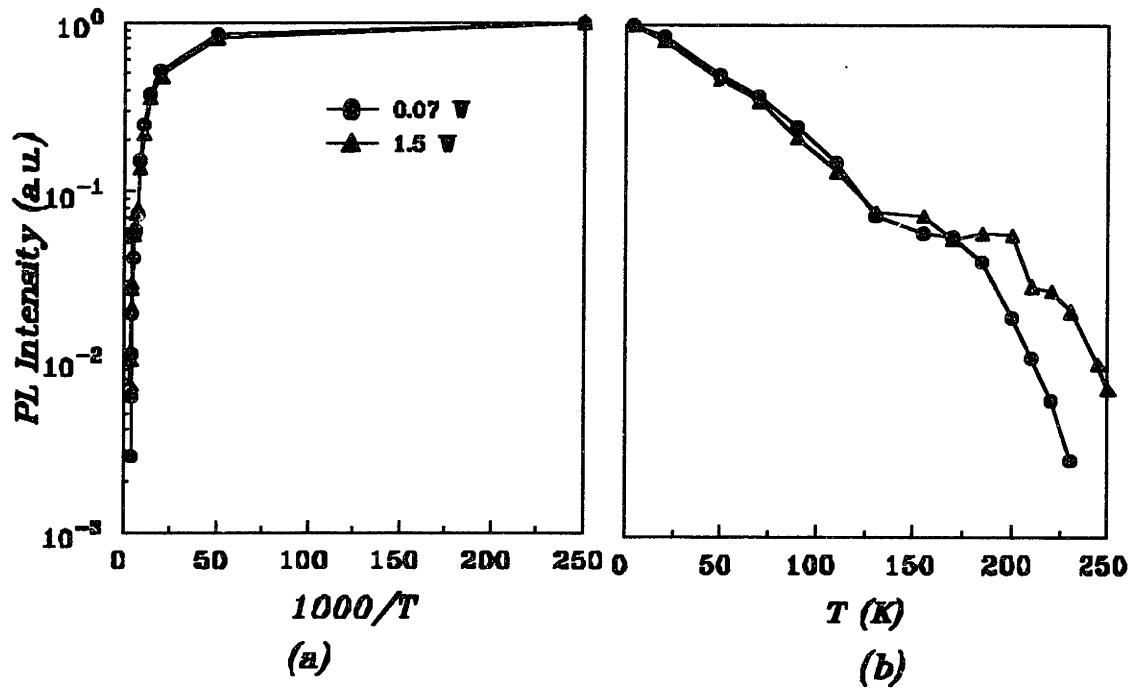

Fig. 5.3 Thermal quenching behavior for sample D (n-type). (a) PL vs. T;
(b) PL vs. 1000/T

Where E_1 and E_2 are the activation energies at low temperature and at high temperature, respectively (a and b are prefactors). For example, the two fitted activation energies for Fig. 5.2 (a) at 1.5 W is 7.6 meV and 139 meV respectively. But for the low power (0.07 W), these two activation energies are 9.8 meV and 179 meV. Thus the activation energies are power dependent, which suggests that the quenching rate for high power and low power is different. This difference can be clearly seen in the plots of PL vs. T (Fig. 5.2 (b) and Fig. 5.3 (b)). These plots show that quenching rate is stronger under low power for both type of samples. By comparing the linear temperature dependence plots of p-type and n-type samples, we can see that they show a different quenching behavior. For the p-type sample, there is just a smooth quenching. But for n-type sample, there are three different regions showing different quenching rates. These regions are: (1)4 K < T < 130 K ; (2) 130 K < T < 180 K and T > 180 K. In later discussion and simulation, we can show that this behavior relates to the Fermi level and the free carrier density.

In Fig. 5.4, we show the power dependence of PL intensity for sample I (which is oxygen coimplanted sample) and sample G (fluorine coimplanted sample) at the different temperatures. The dots are experimental data and the solid lines are extrapolated curves. One of the main points from this plot is that the power dependence curves show the sign of saturation only at low temperature (4 K for sample I and 30K for sample G), i.e., the slope of the curve is zero. The higher the temperature, the less the saturation effect for a given power. For example, Fig 5.4 (b) clearly shows that at 1.5 W, the PL intensity changes from saturation at 30 K to nonsaturation at 200 K. However, from the extrapolated solid curves, the trend of the power dependence suggests that it is possible to saturate all the optically excitable Er at the very high pump power regardless of measured temperature. Thus we can conclude that the optically active Er is the same for each sample under different temperatures, and there is no structural transition as temperature is increased.

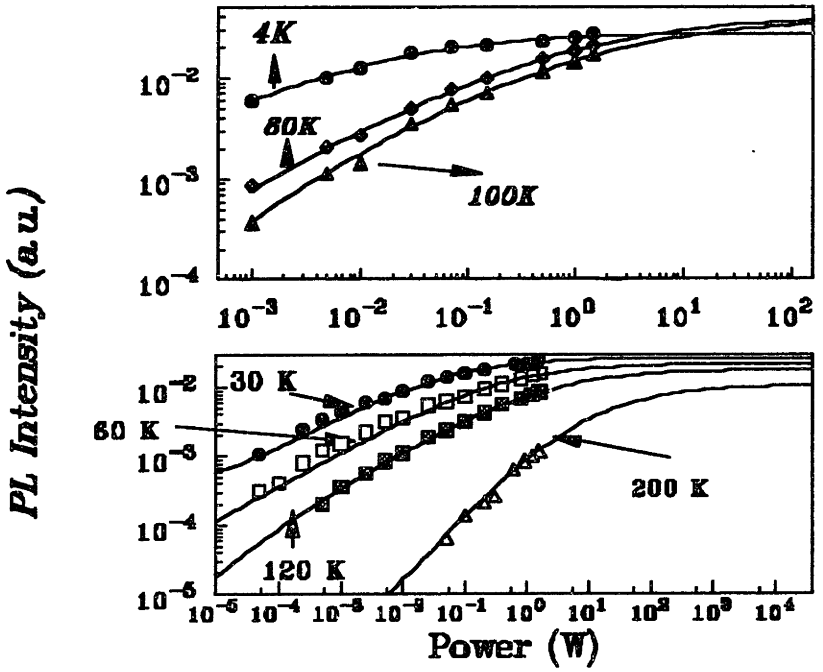

Fig. 5.4 (a) The power dependence of PL intensity at 4K, 60K and 100K for sample I. (b) The power dependence of PL intensity at 30K, 60K, 120K and 200K for sample G . The dots are experimental data. The solid lines are extrapolated curves.

5.3.2 Temperature and Power Dependence of Rise and Decay Time

In order to further understand the quenching behavior, we conducted rise and decay time constants measurements. Fig. 5.5 shows the recorded PL signal at 4 K under two different pump powers of 1.5 W and 0.06 W. The two signals are normalized. It shows that the rise is more sensitive to the power than the decay. The rise curve becomes very sharp at high power. But the decay curve only becomes slightly sharper. Fig. 5.6 shows the temperature dependence (4 K and 100 K) of PL signal at constant pump power of 1.5 W. Signals are normalized. It is interesting to point out that the shape of rise curve does not change at all from when temperature is increased from 4 K to 100 K. But the decay curve is sharper as temperature is increased. This observation is opposite to the behavior of power dependence. Both measurements are done for sample B.

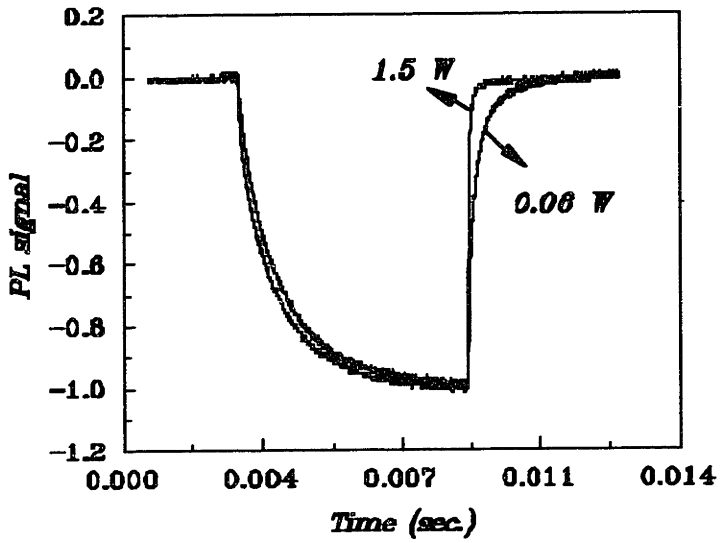

Fig. 5.5 The normalized PL signal at 4 K for power 1.5 W and 0.06 W. Sample B.

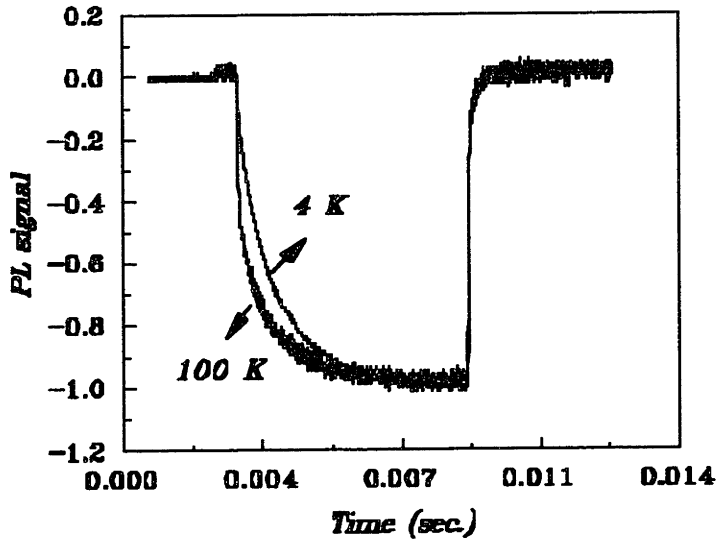

Fig. 5.6 The normalized PL signal at 1.5 W for temperature at 4K and 100K. Sample B.

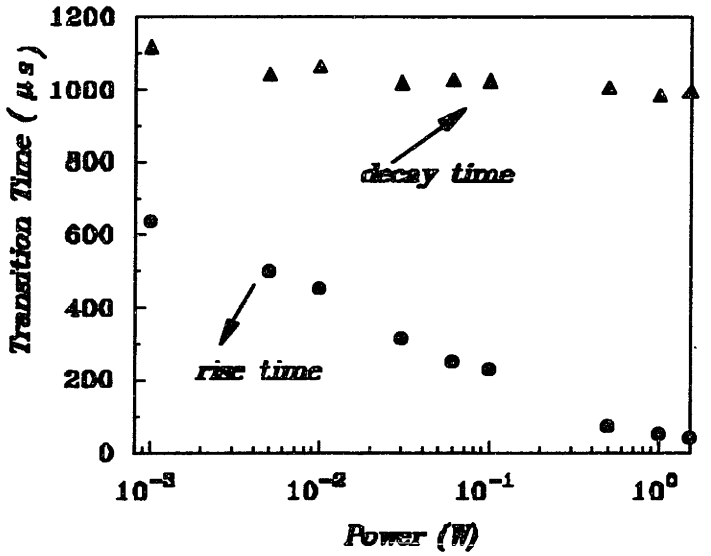

Fig. 5.7 The power dependence of rise and decay time at 4 K. Sample B

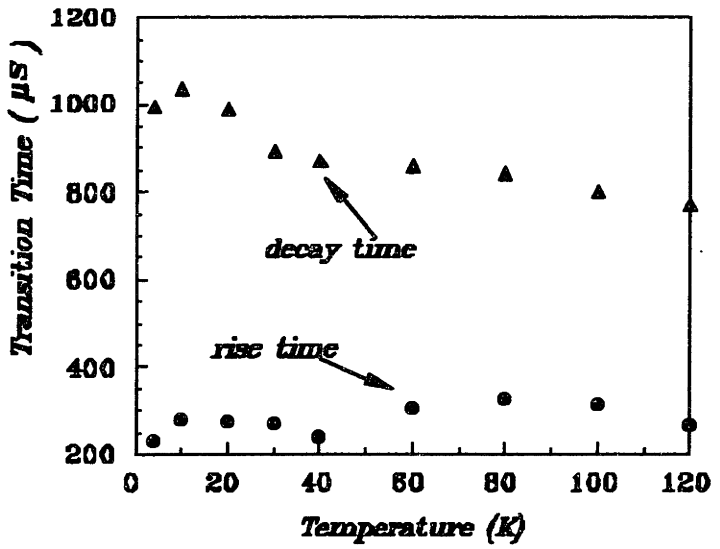

Fig. 5.8 The temperature dependence of rise and decay time at 0.1 W. Sample B

The above observations can be confirmed by plotting the rise time and decay time versus power and temperature separately. The rise and decay time constants can be obtained by fitting rise and decay curves by one exponential function. The results are shown in Fig. 5.7 and Fig. 5. 8. In Fig. 5.7, we plot the power dependence of rise time and decay time. The temperature is 4 K. Fig 5.8 is a plot of the temperature dependence of rise time and decay time. The power is 0.1 W. These two plots indeed verify the our previous observations. From Fig. 5.7, it shows that the rise time is decreased from 600 μs to about 50 μs when the power is increased by 3 orders of magnitude from 0.001 W to 1.5 W. However, the decay time is still around 1 ms. The temperature dependence are totally different. The decay time is decreased from 1 ms to about 750 μs as temperature is increased from 4 K to 120 K. When the temperature is above 120 K, the signal is too weak to get a reasonable fitting. But from another sample measurement (sample O, also p-type), at 160 K and constant pump power of 1.5 W, the decay time is only about 15 μs. So it is expected that the decay time will continue to decrease to below 100 μs when temperature is above 150 K. But the rise time is about same of 300 μs.

How does the lifetime relate to the thermal quenching as it was discussed in last section? Fig. 5.9 plots the PL vs. 1/T and lifetime vs. 1/T together. The plots clearly shows that there is a close relationship between the quenching and the decrease of lifetime. The measure lifetime is the effective lifetime other than the radiative lifetime because the decrease of radiative lifetime will increase the PL intensity. But the lifetime in the plot decreases as the temperature is increased.

Coffa et al proposed that there are two types of Er centers. A fast Er center which has a fast decay time about 100 μs, and a slow Er center which has a decay time around 1 ms. They obtained this conclusion by fitting the decay curve as a function of two exponentials [36]. They also showed that PL intensity from fast decay Er increases almost linearly with pump power in the measured range of 0.01 W to 0.06 W, while the slow Er shows saturated behavior. The thermal quenching effect for fast Er is also much less than slow Er, and it is the dominant PL in the high temperature. They concluded that the decrease of lifetime and the reduction of excitable Er as the increase of temperature are responsible for the quenching behavior above 150 K.

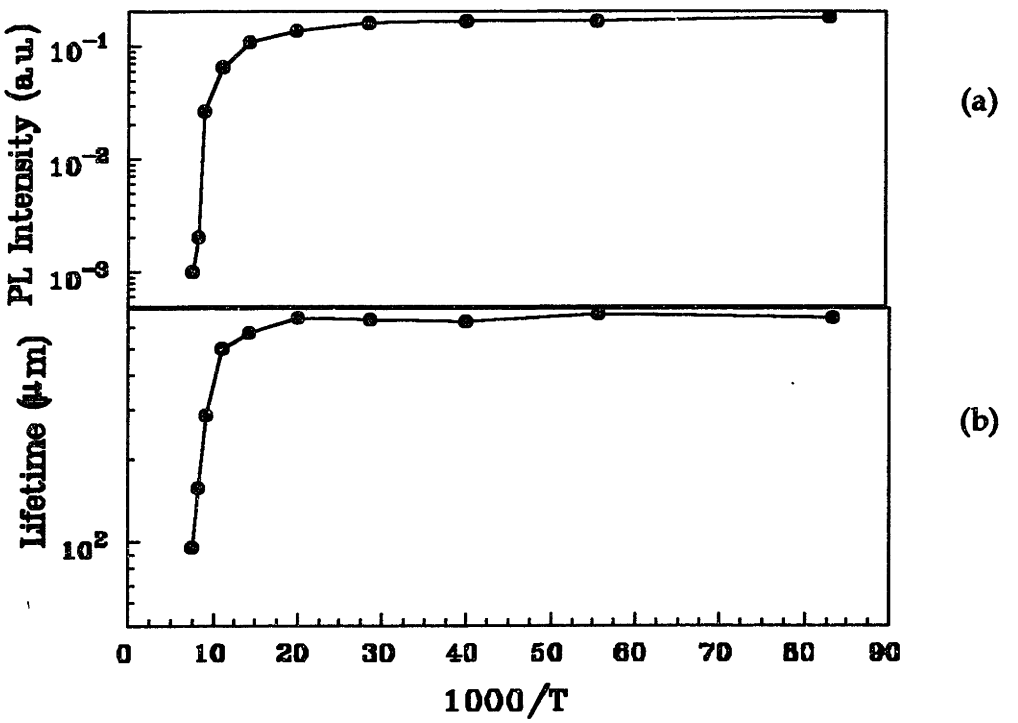

Fig. 5.9 (a) PL vs. 1000/T. (b) Lifetime vs. 1000/T. Sample G.

We did a similar analysis for our measurements for both decay and rise curves. Eq. 5.1 is the fitting function.

$$I(t) = c_1 \exp(-\frac{t}{\tau_1}) + c_2 \exp(-\frac{t}{\tau_2}) \qquad (5.2)$$

where c_1 and c_2 are coupling factors of time constant τ_1 and τ_2, which can also be viewed as the representatives of contribution to the PL intensity by the two lifetime components. τ_1 is about 1 ms and τ_2 is about 100 μs for the decay at 4 K. Both of them decrease as temperature is increased. For the rise time, τ_1 is about 600 μs and τ_2 is about 100 μs at 0.01 W and they decrease as power is increased.

Besides the temperature and power dependence study of lifetime, the same dependence study for the two contribution factors c_1 and c_2 can also give us some insight

information about the roles c_1 and c_2 play at the different temperature and power. Fig. 5.10 (a) shows the power dependence of c_1 and c_2 at T = 4 K for sample B. It is for the decay curve. The plot shows that both c_1 and c_2 increase with power, but not linearly (Log horizontal axis). c_1 increases at a faster pace than c_2. The plot shows that c_2 saturates earlier than c_1 for the power dependence. This observation is not in agreement with Coffa's result that the fast component linearly increases with the power. However, measurements on other samples confirm Coffa's result. Fig. 5.10 (b) shows the power dependence for sample G.

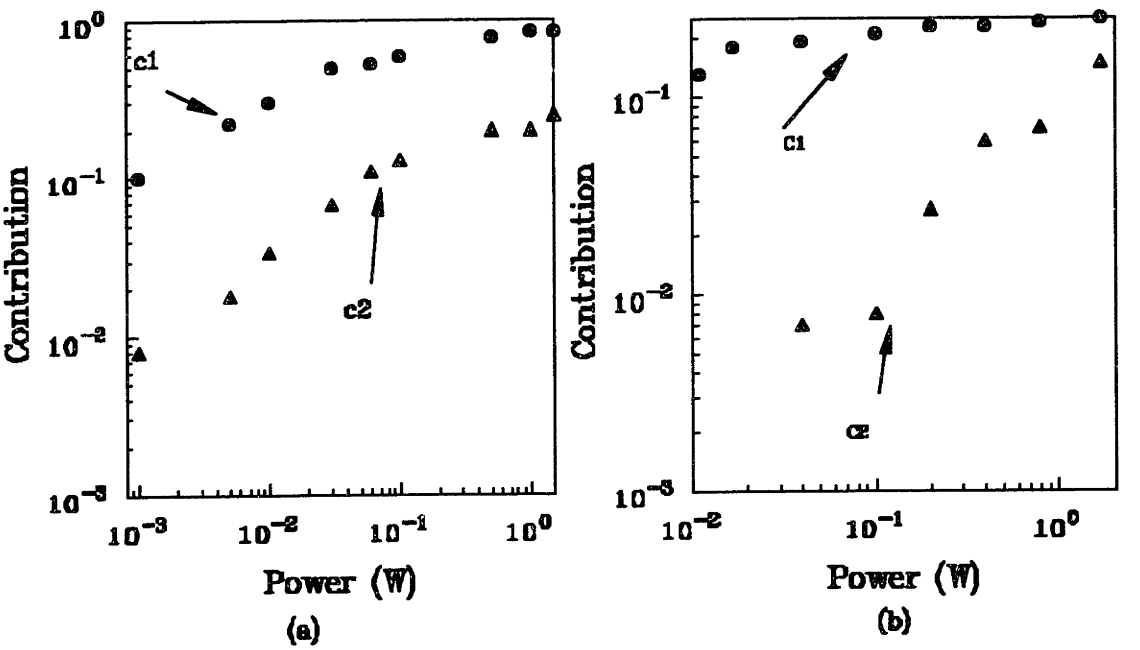

Fig. 5.10 power dependence of coefficients of decay curve. c_1 refers to the long component and c_2 refers to short component. T= 4K (a) Sample B. (b) sample G

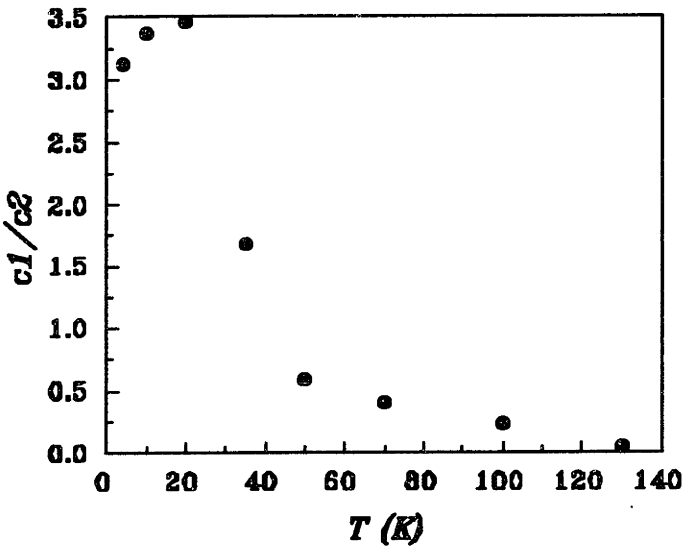

Fig. 5.11 The temperature dependence c_1/c_2 at pump power 1.5 W. Sample O

The data clearly indicate that the long component contribution saturates much earlier than the short one. The Similar behavior is observed in measurements on other samples. Spreading resistance and SIMS measurements show that sample B is very inhomogeneous. It is supposed to be an heavily boron doped sample but from SIMS data, there is no boron content, which might give one explanation that sample B behaves so differently from others. We believe the data in Fig. 5. 10 (b) is more accountable.

Fig. 5.11 is the temperature dependence of the ratio of the two coefficients for sample O. The reason to choose ratio instead of absolute value is that both c_1 and c_2 decrease with temperature. The ratio of them is a good indicator of which one is more important as temperature is increased. The power is 1.5 W. The plot shows that there is a increase at beginning, which could be due to the fitting error. When temperature is below 20K, the PL intensity should not change much. All the other data clearly shows that the short component effect is increase as temperature is increased. When T > 100 K, it dominates the PL intensity.

It also worth showing the power dependence of c_1 and c_2 at 4 K for the rise curve (Fig. 5.12). The trend is very similar to that of the temperature dependence of decay. As the pump power is increased, the short component is becoming dominant. The excitation is getting faster at higher pump power because the short component becomes the major player at thigh power. The two components almost equally weighted when pump power is about 0.03 W.

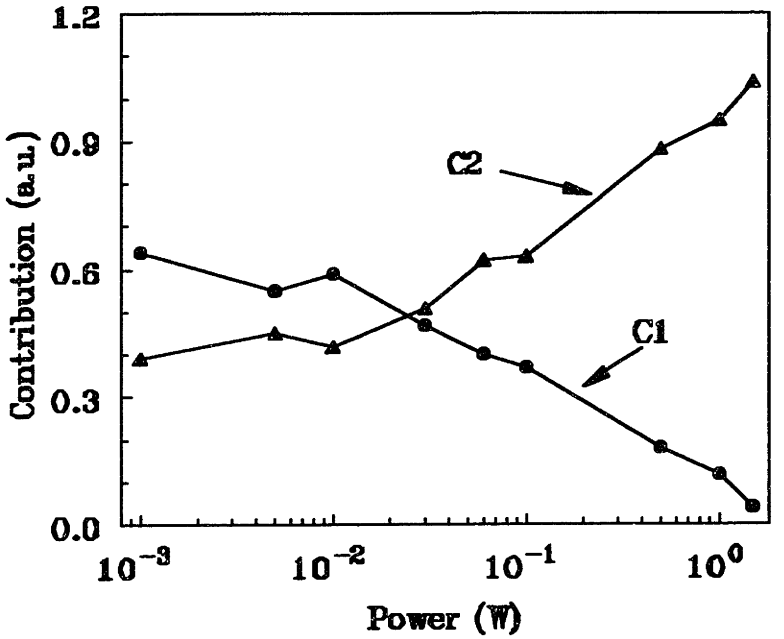

Fig. 5.12 The power dependence of c_1 and c_2 at 4 K. Sample B.

5.3.3 Lifetime of Samples with Different Ligands

The lifetime study is also carried out in samples coimplanted with different ligands. The data shows that the decay time might not depend on as strongly ligands as different process conditions. This result is shown in Fig. 5.13. In this plot, the horizontal axis represents different implanted ligands and the vertical axis shows the decay time for different ligands. The unit is μs. The pump power is 0.1 W and temperature is 4 K. The

lifetime data is obtained by one exponential fitting of the decay curve. In general, the decay time is about 1 ms. Lifetime of three fluorine samples are also shown in the plot, F14, F12, F66. Table 5.1. lists process condition, the lifetime and PL intensity. The sample F66 only has [Er] 3 x 10^{18} cm^{-3}. The other two samples has [Er] 5 x 10^{18} cm^{-3}. Simulation study has shown that there is a linear relationship between the PL intensity and the fluorine concentration [37]. In order to compare the PL intensity effectively, we can multiply the value for sample F66 by a factor of 5/3. Table 5.1 suggests that the shorter the lifetime, the higher the PL intensity. But the difference between sample F12 and F66 is marginal. If this observation is true, it gives some valuable information about how to maximize PL intensity. However, because it is done for only one type of ligand, more comprehensive study is needed before a firm conclusion can be made.

Table 5.1 Comparison of three fluorine samples.

	F14	F12	F66
[Er] (cm^{-3})	5 x 10^{17}	5 x 10^{17}	5 x 10^{17}
[F] (cm^{-3})	5 x 10^{18}	5 x 10^{18}	3 x 10^{18}
Annealing cond.	1000 °C, 1/2 hr.	800 °C, 1/2 hr.	900 °C, 1/2 hr.
Lifetime (μs) (4K)	1000	750	600
PL (Vol.) (0.01 W)	0.06	0.19	0.12/ 0.20
PL (Vol.) (1.5 W)	0.18	0.35	0.23 / 0.38

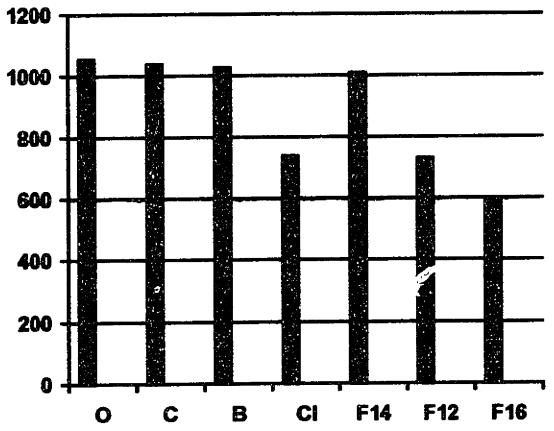

Fig. 5. 13 The decay time for different ligands. The horizontal axis represents the different ligands, and the vertical axis represents the lifetime. The unit is μs.

5.4 Junction Photocurrent Spectroscopy Measurement

One of the critical questions regarding the Er defect is whether there are any levels in the gap or not. A level is not necessary related to Er 4*f* electron. This information can help us construct a correct model to describe the PL process. In the preceding chapter, we showed that from the first principle calculation, there are two possibilities. (1) If Er is isolated and sits in the interstitial site, there will be some levels in the gap and they are related to 4*f* electrons. (2) If Er is surrounded by 10 oxygen forming a complex, all the 4*f* levels are in the VB. No 4*f* levels are found in the gap. These theoretical predictions need to be verified by experimental evidence.

The junction photocurrent spectroscopy (JPS) is a setup to detect energy level in the bandgap. The basic principle of operation is as follows: an external light source excites a carrier from a band edge to a level in the gap. The carrier can jump into the CB by thermal interaction forming free electron-hole pair. The electron-hole pair is then collected by the junction and the current is collected by a detector. A schematic setup is shown in

Fig. 5. 14. The quartz Halogen lamp is the light source. The light beam is focused by the lens, and the chopper is used to modulate the frequency of light. The monochoromator is used to select different wavelength (energy) to excite carriers into different levels in the gap. Current may needs to be amplified before being detected. This experiment is suitable for room temperature measurement, because carriers are much more easier to thermalize than they are at low temperature. When a level in the gap is detected, this measurement can not tell directly whether it is below CB or above VB by just looking at one measurement. Some comparison to different samples have to be made before a conclusion is drawn. Also this measurement will not be able to tell us whether the gap level is related to Er or not.

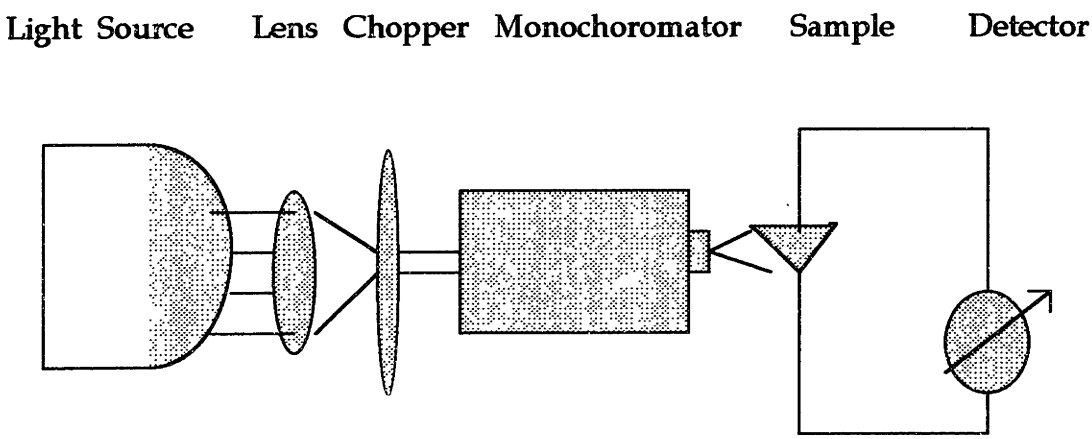

Fig. 5.14 A schematic setup for the junction photocurrent spectroscopy

Fig. 5.15 is a typical plot obtained by JPS measurement. The reference sample G7 is a plain Si with a p-n junction. No Er implantation was done on it. D61 is a n-type sample with implanted [O] = 3x 10^{18} cm^{-3}. The C2 is a p-type sample with same oxygen implantation. The plot shows that there is a level for the p-type sample C2 at about 0.94 eV. This level does not appear in the n-type sample, indicating that the level is 1.12 eV - 0.94 eV = 0.18 eV below the CB. Because for the n-type sample, the Fermi level is high enough so that this level is filled, no photocurrent can be detected. There is another peak

around 0.8 eV in both n-type and p-type samples. It is not clear the origin of this peak, because this peak varies with the experiment condition such as the position of incident beam. It is also found in the reference sample. Further investigation is needed before we can make any conclusion. The 0.94 eV level is always there for different p-type samples, but not in n-type sample. Its origin is not sure at this moment. It could be Er related or it is just created by implantation damage and has nothing to do with Er. However, the information of positions of levels is very valuable for the modeling work in the next chapter.

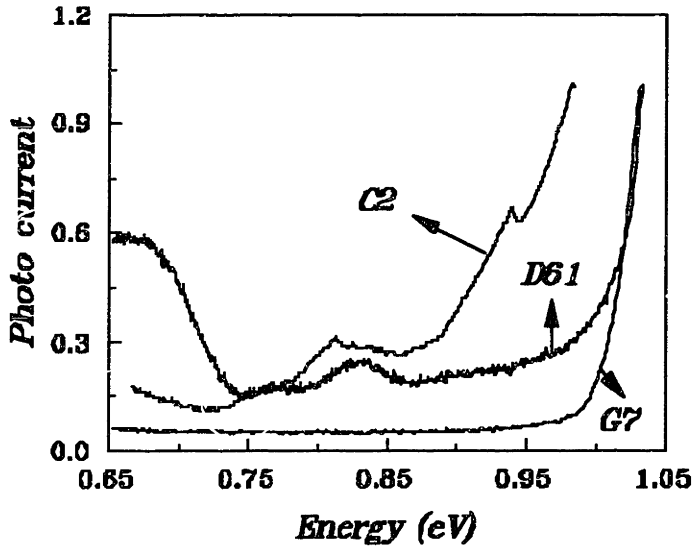

Fig. 5-15. The JPS plot of sample C2 (p-type), D61 (n-type) and G7 (reference sample)

5.5 Discussion and Summary

In section 5.3.1 and 5.3.2, we have shown that the activation energy for the thermal quenching given by Eq. 5.1 is not a fundamental property of a Si:Er sample because of its power dependence characteristic. It worth pointing out that the activation energy depends on the final measured temperature. This usually can be ignored because signals from some samples are too weak to be detected. If the temperature is not high enough, even for the same sample at the same power, the activation energy is different. It is especially true for the high activation of E_2. This is reasonable by examining Fig. 5.2 (a). As temperature is getting higher and higher, the drop of PL intensity is steeper. E_2 becomes larger. So, it is necessary to measure temperature above 200 K in order to get an accurate activation energy at a given power, although signals from some samples may be too weak to be detected at this temperature. Table 5.2 summarizes the activation for all the measured samples. It is interesting to notice from the table that the higher activation energy does not mean a steeper quenching. For instance, the data for sample K shows that E_2 at high power is larger than E_2 at low power, but the quenching is much stronger at low power. How much is the difference between the high power and low power quenching rate? This can be estimated from Fig. 5.2 for p-type sample and Fig. 5.3 for n-type sample. If we define the quenching factor as the ratio of PL intensity at the lowest temperature to that at the highest temperature. Then for the p-type sample D, the quenching factor at pump power of 1.5 W is about 50, while at power of 0.07 W, it is about 360. i.e., low power thermal quenching is about 5 times more than that for high power case. Similarly, there is about 7 times difference between the high power quenching and low power quenching for the n-type sample I.

The power dependence of thermal quenching can be explained by considering saturation effects and nonradiative process. As it is known that the solubility of Er in Si is very low, about $1x10^{16}$ cm^{-3} [37]. So there is only limited number of Er implanted and the number of optically active Er centers are even smaller. At high power, many more electron-hole pairs are generated, and all the optically active Er centers are fully activated. As temperature is increased, the nonradiative process becomes more efficient. More and more excited Er are quenched. However, if excitation power is high enough, there are

always more electron-hole pairs around Er and the deexcited Er has higher probability of getting re-excited. Thus, the quenching effect is less. Fig. 5.4 also shows that it is possible that at very high power, all the active Er centers can be saturated at a level very close to each other regardless of present temperature.

Table 5.2 Activation energies for different samples under high and low power

		High Power (1.5 W)				Low Power (0.07 W)			
		a	E1(meV)	b	E2(meV)	a	E1(meV)	b	E2(meV)
D	D61	6.13	5.6	1.07e4	77	4.89	5.6	7.4e4	90
B	JJ2	8.18	9.5	1.97e7	176				
C	C5	420	12.8	178e3	88	2.21	6.72	9.9e5	150
K	12	10.53	14	1.56e7	223	23.97	13	7.7e6	182
I	C16B	1.57	7.6	1.06e5	139	9.77	9.5	5.7e6	179

Then the next question is: What is the nonradiative process? Fig. 5.9 correlates the PL quenching to decrease of the lifetime. We concluded that the lifetime is an effective one. The decrease of this effective lifetime is due to the increase efficiency of the nonradiative process according to the relation shown in Eq. 5.3

$$\frac{1}{\tau_e} = \frac{1}{\tau_r} + \frac{1}{\tau_{nr}} \qquad (5.3)$$

where τ_r and τ_{nr} are the lifetime for the radiative and nonradiative process, respectively. There are two possibilities for the nonradiative process. The first is the multiphonon process. But there is no experimental evidence to support this assumption. It is very difficult to do the IR absorption measurement for the Er implanted sample, since the Er

profile is only about 1 μm below the surface. Another is the Auger process. Two experiments have done to verify this assumption. The first is the lifetime measurement when a reverse bias is applied to the Si:Er LED. The experimental data shows that the lifetime is increased as the reverse bias is increased. The larger the reverse bias, the larger the depletion width and the less the carriers around the Er, which decreases the efficiency of nonradiative process. Thus a longer effective lifetime is obtained. The second experiment is also the lifetime measurement, but a second CW laser beam is used to ensure a constant steady state background electron-hole pair density. The data are plotted in Fig. 5. 16. The lifetime decreases very fast as the power of second beam is increased, because there are more carriers available for the Auger process. Based on these two experiments, we believe that Auger process is the nonradiative process for the thermal quenching.

The Auger process can explain the decrease of PL intensity as temperature is increased, because the equilibrium background carrier concentration is increase with temperature, which is given by the Eq. 5.4.

$$n = N_c \exp(-\frac{E_f}{kT}) \tag{5.4}$$

where, N_c is the effective conduction band density of state and E_f is the Fermi level energy. The probability of an excited *f* electron passing its energy to the free carrier is increased very much at higher temperature. Thus, the nonradiative effect is dominant at the high temperature, and more and more excited *f* electrons pass energy to carriers before light emission process taking place.

As we noticed from PL vs. 1/T plots that the strong quenching starts at T > 100 K, we may ask: is free carrier density high enough at this temperature so that Auger process is effective? What is the value of Auger coefficient?

The Auger coefficient can be estimated by the following equation [42]:

$$C_A = (\tau_r n_0)^{-1} \tag{5.5}$$

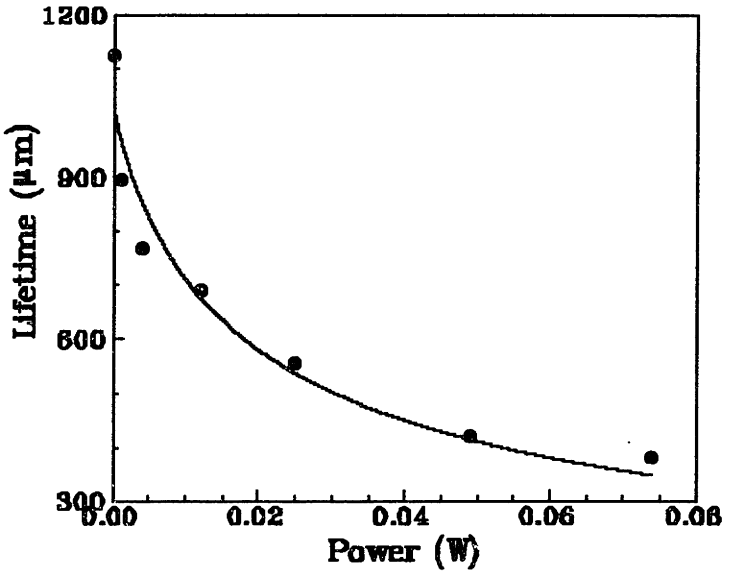

Fig. 5.16. The measured lifetime vs. the power of second beam in the 2 beam experiment. The solid line is used to guide the eye.

where τ_r is the radiative lifetime, n_0 is critical carrier concentration, which is given by Langer [42]:

$$n_0 = 4\pi^{5/2} n_r^{\,5} \sqrt{\frac{m_o a_B}{m^* a_f}} \lambda_0^{-7/2} \qquad (5.6)$$

where a_f = 1/137, a_B = 0.529 Å, and n_r is the refractive index for Si. λ_0 is the radiative wavelength, which is 1.54 μm in our case. Assuming m / m* = 1, we obtain $n_0 = 1.0 \times 10^{13}$ cm^{-3}. This result is surprisingly small although the value can be somewhat higher if the effective mass is considered. But this provides an explanation of quenching at 100 K.

Since at this temperature, the free carrier density can reach 1.0x 10^{13} cm^{-3}, which is shown in the simulation in the next chapter. It will be more convincing if the free carrier density can be measured directly from experiment. The Auger effect is more effective when temperature is above 100 K. We may also notice that the decay time decreases only slightly as power is increase at 4 K as shown in Fig. 5.5. However, the decay time decreases very much if temperature is increased. Thus, It might suggest that the quenching by excess carriers generated by laser is much less than that by the equilibrium background free carriers.

So far all the explanations focus on the decay curve. It is also possible to study the rise curve. Fig. 5. 7 shows that rise time decreases with the increase of power. If we consider there are only two process happened in the excitation. The first is the diffusion process, the second is the excitation process, which is believed to be an Auger-type process [43]. The time to excite Er *f* electron from ground state to the excited state can be assumed to be a constant. Then the effective rise time is the sum of two-step "serial" process., i.e., $\tau = \tau_d + \tau_e$,, in which the longer one is the rate limiting step. The diffusion time can be estimated by the following formula:

$$\frac{1}{\tau} = 4\pi N_{Er} D\sigma \qquad (5.7)$$

Where N_{Er} is the Er content, D is carrier diffusion coefficient and can take the value of 35 cm^2 /s. σ is the cross section area related to the Er. If we assume the quenching process is Auger process, Coulomb interaction dominated, the capture rate can be estimated by:

$$\frac{q^2}{4\pi\varepsilon_0 \varepsilon r_c} = kT \qquad (5.8)$$

where q is electron charge, r_c is the capture rate. Then the cross section σ is

$$\sigma = 4\pi r_c^2. \qquad (5.9)$$

At the 4 K, σ is about $1.5x10^{-14}$ cm^2 by this calculation However, the above equations apply only when temperature is high enough (T > 200 K). For low temperature, the σ is a constant. If we assume the site is neutral, then $\sigma \sim 1x10^{-15}$ cm^2. If $N_{Er} = 5x10^{17}$ cm^{-3}. We get $\tau \sim 10$ μs. So the diffusion is very fast. It is about the same as our system's response time. It is a not a rate limiting step during the excitation process.

Based on the discussion we have, it is possible to summarize some of the characteristics of the rise and the decay. The most striking character is that rise and decay behave almost in the opposite direction. The rise time is temperature independent while the decay time is decreasing with temperature. The rise time is decreasing with temperature while the decay time is almost insensitive to the temperature. This and other features are summarized in Table 5.3.

Table 5.3 The power and temperature dependence of excitation and deexcitation time

	Temperature	Power	Two exponential characteristic	One exponential characteristic
Decay time	T ↑, τ ↓	Very little sensitive	High power Low temperature	Low power high temperature
Rise time	Insensitive	Power ↑, τ ↓	Low power	High power

As we mentioned eariler that p-type and n-type samples show different thermal quenching behavior at the same power. Fig. 5.17 shows the PL intensity versus T under high power (1.5 W) for a n-type sample D and a p-type sample C. From the plot, it shows that for the n-type sample, there are three different quenching regions. The first one is from 4 K to 130 K. This could associate with a shallow donor with an activation energy of 45 meV. Between 130 K and 180 K, the shallow donor is depleted but the deep donor is

not activated enough to give more carriers and cause large quenching. So this is a flat region. When T > 180 K, the deep donor is activated enough to cause efficient quenching. The deep donor level is about 180 meV which can be estimated from JPS measurement. This behavior can be simulated in the next chapter. However, the p-type sample only shows a smooth quenching effect. However, the equilibrium free carrier density in the sample is very complicated. An earlier DLTS measurement showed that there are 11 levels in the gap for a p-type sample [44]. Some spreading resistance measurements for the samples with a background doping of 10^{16} cm^{-3} (sample A and sample O) shows that there is a junction on the shoulder of Er profile, which means that Er concentration is very inhomogeneous It has three regions: p-type, depletion and n-type. The inhomogeneity of free carrier density also complicates our simulations in the next chapter.

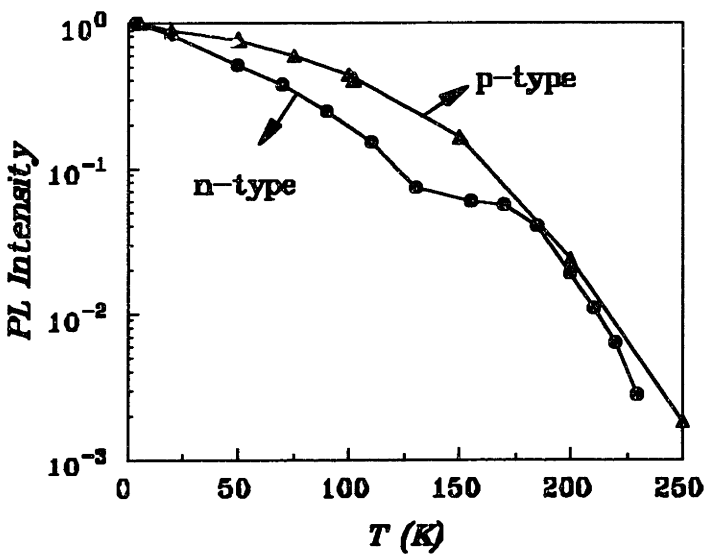

Fig. 5.17 The PL intensity vs. T for p-type sample K and n-type sample D at high power (1.5 W). PL intensity is in arbitrary unit (a.u.).

The last question we would like address in this chapter is: Two Er centers or one Er center in Si:Er? Fig. 5.10 (b) and 5. 11 indicate that there is a fast component which has more influence at high power and high temperature. This fast component is associated

with the sharp decay at the beginning of the decay curve. The two-Er center model proposed by Coffa can easily explain the decay curve. But it cannot explain why s the lifetime of both components decrease as temperature is increased? One the other hand, the one-Er center model can also give an explanation, but it is not so obvious. If we can think of the decay time changes with respect to the time scale, then an explanation can be obtained by relating it to densities of free carriers or exciton and bound carrier or bound exciton. For example, at the beginning of the time, there are more free carrier available for the deexcitation process. The deexcitation time is fast. As time is passing by, the free density decreases very fast, and it is getting difficult for Er to pass its energy to the free carrier so the deexcition time is long. As we know, the effective lifetime is determine by the parallel process given by Eq. (5. 3), we will observe a sharp decay at beginning and a long decay later. These hypothesis has to be verified by the experiment. The most direct experiment is to separate these two components and measure the PL spectra of them. If there is no change in the PL spectra, then one-Er center model is valid. Otherwise, two or more Er centers model is valid.

An interesting point is that Langer et al attribute this sharp decay to the exchange effect between a weakly bound exciton and a shallow donor or shallow acceptor [45]. This effect can be simulated quite nicely which will be shown in next chapter. However, the bound exciton effect may not be able to explain the fast decay at the high temperature because there is no bound exciton at the high temperature unless it is bound to a very deep level. It is also possible that at high temperature, the large amount of free carriers will cause enough quenching to have a very short lifetime. We don't have any lifetime data for the temperature above 130K. Further study is needed.

In summary, the power and temperature dependence of PL intensity, decay time and rise time are studied in this chapter. We find that activation energy is not a fundamental properties of Si:Er material anymore due to its power dependence. Saturation effect is very important to understand the thermal quenching behavior. At the same power, PL intensity can change from saturation at 4K to non saturation at 200K. But they tend to be saturated at the almost same level. Thus the total number of optically active Er is about the same, and there is no structural change as temperature is increased. Si:Er samples

under high pump power have much less quenching than that under low pump power. The rise time and decay time have totally different power and temperature dependence characteristics. Rise time is insensitive to the temperature and decreases with increasing of pump power, while decay time is insensitive to the power and decreases with increasing of temperature. Reverse bias and two beam measurements strongly indicate that Auger effect is mainly responsible for the quenching.

Chapter 6

Kinetics of Luminescence of Er Centers in Si

6.1 Introduction

The investigation of Er centers in silicon so far in this thesis focuses on the study of fundamental properties from both theoretical and experimental points of view. Theoretical approach was used to study the bonding among Er 4*f* electrons, Si host and ligands. Possible positions of Er 4*f* levels in the Si:Er system are proposed, but the proposals have to be verified by experiment. The photoluminescence study in last chapter strongly indicates that Auger effect is the major thermal quenching mechanism. It is believed from studies of other publications that the excitation mechanism is an Auger type as well [43]. However, the dynamic process of quenching and energy transfer is still unclear. We hope simulation work in this chapter can provide more information about the PL process and can describe some of the experimental results.

6.2 Photoluminescence Process

As shown in the PL setup diagram of Fig. 5.1, shining a larger than bandgap light on the Si:Er sample will result light emission from the sample, this sounds very simple, but the physics behind it is very complicated. The flow chart of Fig. 6.1 summarizes possible processes that transpose light in (laser power pump Si:Er) to light out (light emission). Electron-hole pairs are generated by the laser and diffuse to the Er in the form of either free carriers or excitons (for simplification of discussion, we do not distinguish between free carriers and excitons). They can be bound to the Er or Lost due to either a nonradiative process or a radiative process or both The radiative recombination energy of bound exciton will pass to Er and 4*f* electrons are excited from its ground state to the excited state. The energy loss mechanisms for bound

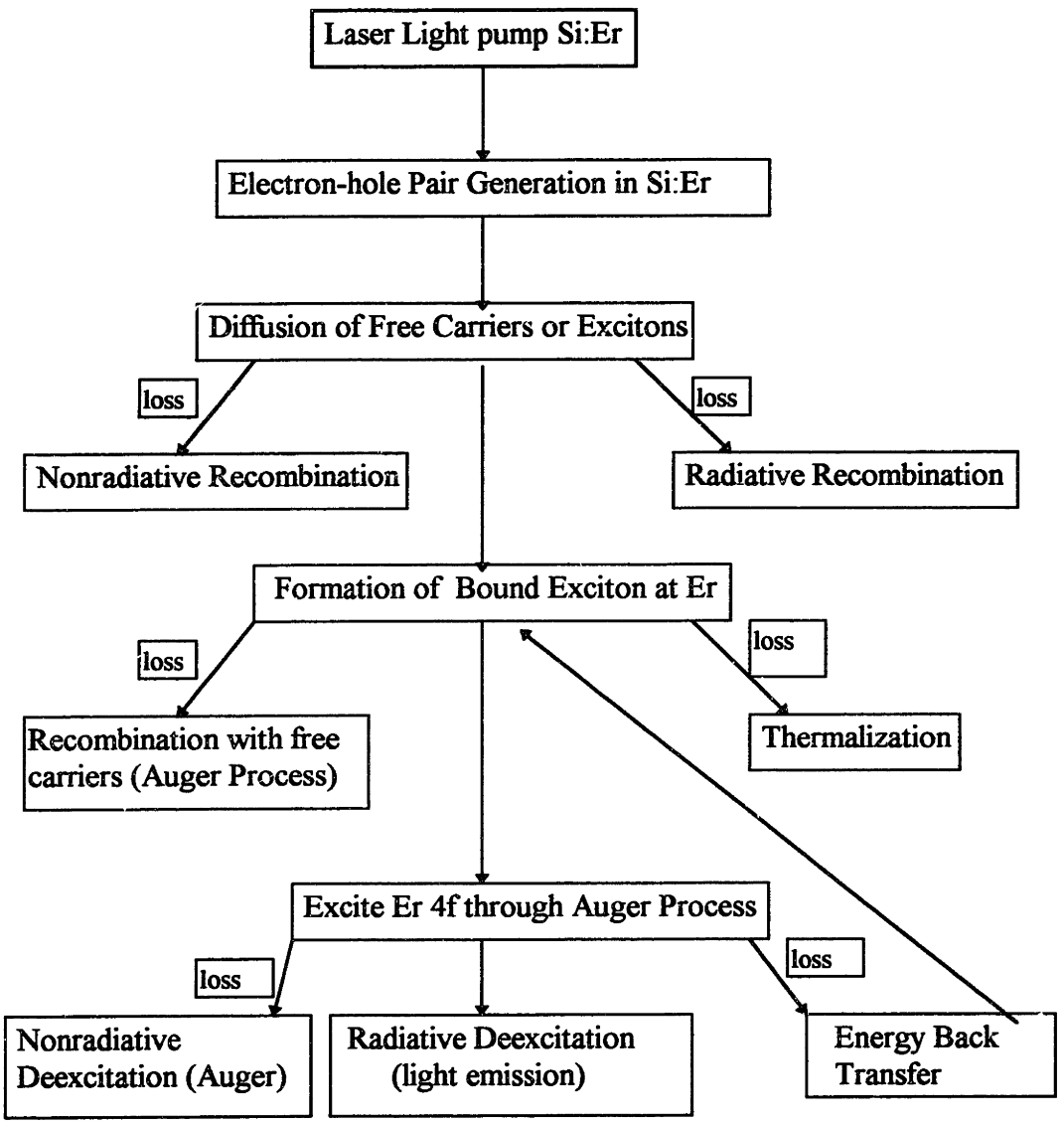

Fig. 6.1 The flow chart of PL process in Si:Er

exciton can be an Auger process (bound excitons recombine with free carriers) or a thermalization process occurring at high temperature). Radiative decay of the 4*f* electron gives the light emission. The energy can also be lost by a nonradiative process (Auger is the most probable one at low temperature) or an energy back transfer process. One of the most difficult tasks is to identify the dominant mechanism for each process. This information is crucial to establish a correct model. In return, even without complete information, modeling can give some details about how the proposed mechanisms change under different conditions (temperature, power, etc.) which may not be observable in the experiment. Some of the simulated data can be directly compared to the experiment to verify the correctness of the model.

It is necessary to start with some assumptions before deriving rate equations to describe possible processes. These assumptions are listed as follows. They are usually based on the experimental observations and some simplifications.

- One type of Er center.
- Auger effect is the dominant quenching mechanism, which can be described by $P_A = C_1 n_{ex} + C_2 n_{eq}$, where C_1 and C_2 are Auger effect coefficient for excess free carriers / excitons and equilibrium free carriers respectively. C_2 is only needed for temperature dependence study. For the power dependence study, we assume the low temperature condition with no background equilibrium carriers.

A simplest set of rate equations is as follows:

$$\frac{dN_{Er}}{dt} = \frac{n}{\tau_e} - N_{Er}\left(\frac{1}{\tau_r} + \frac{1}{\tau_q}\right) \tag{6.1}$$

$$\frac{dn}{dt} = G - n\left(\frac{1}{\tau_e} - \frac{1}{\tau_c}\right) \tag{6.2}$$

where N_{Er} is the number of excited Er, and n is the carrier density generated by laser beam. G is the generation rate. τ_e is the excitation time, τ_r is radiative lifetime, τ_q is quenching lifetime and τ_c is the lifetime of a competitive process, such as recombination of electron hole pairs. We leave this process as an option for future work and assume it is very slow for the current work. Eq. 6.1 and Eq. 6.2 describe the excitation and deexcitation processes of Er and free carriers / excitons respectively. However, rise and decay curves obtained by these equations are symmetric. The rise and decay time constants are the same, and they are independent of pump power. Obviously, this result does not agree with experiment data discussed in the last chapter. As the experiment suggests that the saturation effect is important. A saturation term is included for both equations and the new rate equations are:

$$\frac{dN_{Er}}{dt} = \frac{n}{\tau_e}\left(1 - \frac{N_{Er}}{N_{Tot}}\right) - N_{Er}\left(\frac{1}{\tau_r} + \frac{1}{\tau_q}\right) \tag{6.3}$$

$$\frac{dn}{dt} = G - n\left(\frac{1}{\tau_e}\left(1 - \frac{N_{Er}}{N_{Tot}}\right) + c_{ex}n + \tau_c\right) \tag{6.4}$$

where, one more term $c_{ex}n$ is included for the quenching of exciton. N_{Tot} is the total number of implanted Er. This set of equations are solved, and the results are plotted in Fig. 6.2. Some of the parameters and rate constants used are listed in Table 6.1. The implanted Er density is 5×10^{17} cm^{-3}. Assuming 10% is optically active, $\tau_e = 10$ μs. $\tau_q = 10^{-12}$ n, i.e., the Auger coefficient is 10^{-12}, which is smaller than the value of 10^{-10} calculated in last chapter. The calculated value of c_1 of 10^{-10} is only for the background equilibrium free carriers (temperature dependent). $\tau_r =$ 1 ms, which is the radiative lifetime. The influence of competitive process is not considered here. Fig. 6.2 simulates the PL process at 4 K. By comparing to experimental data in Fig 5.5, the general features of power dependence for rise have been nicely reproduced. Increasing pump power, the shape of rise curve becomes

increasing sharper. The simulated decay curve does not show any change under different powers while the experimental curve shows a slight change. The difference could be due to the existence of other quenching processes which are not considered, or the rate equations are incomplete. One of the simplest way to test this is to set the rate constant of competitive process to be proportional to the carrier density. This test shows that the shape of decay does not change either. Therefore, it is possible that more rate equations are needed to describe the PL process. A more complicated model including the formation of free and bound excitons is under construction which gives a different shape of decay under different powers But details are not complete yet. This simple model simulation can also show that the quenching effect is not a constant, but it depends on the carrier density (laser power). If the τ_q is set to a constant, the decay curve is distorted at very high power. The plot also shows that the maximum PL intensity is not equal to all of the optically active erbium due to the quenching process is competitive. The faster the nonradiative process, the less the PL intensity.

Table 6.1 The parameters used in the rate equations.

τ_e	τ_r	τ_q	τ_c	N_{er} (cm^{-3})	G(high) (cm^{-3} s^{-1})	G(low) (cm^{-3} s^{-1})
10 μs	1 ms	10^{-12} n	0.1 s	5 x 10^{17}	4x10^{20}	2x10^{19}

6.3 Power dependence Simulation

The next step is to simulate the low temperature (4K) power dependence of PL intensity by the steady state solution of the rate equations. This is shown in Fig. 6.3. The dots are experimental data from sample O and the solid line is the simulated curve. The simulation is in good agreement with the experimental data. So the simple rate equations can describe the power dependence of PL. At the beginning (very low power, 10^{-5} W), there is almost linear relation between PL and pump power, which means that Er is not saturated. As power is increased, Er is getting saturated, and the increase of PL intensity is getting less and less but not fully saturated within the experimental pump power. The simulation also

shows that it is possible to have little quenching, if the starting pump power is 1.0 W and then pump all the way up to the full saturation of optically active Er.

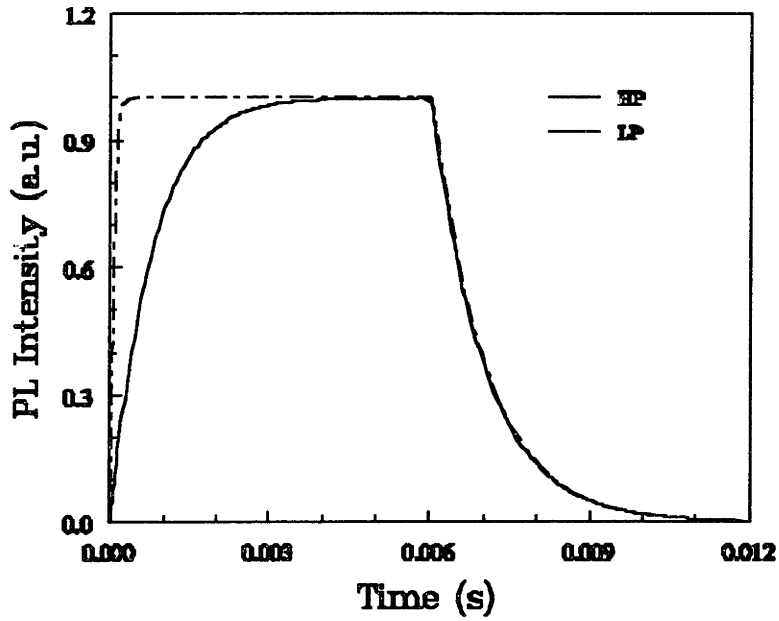

Fig. 6.2 Simulation Results by solving the rate equations under different generation rate.

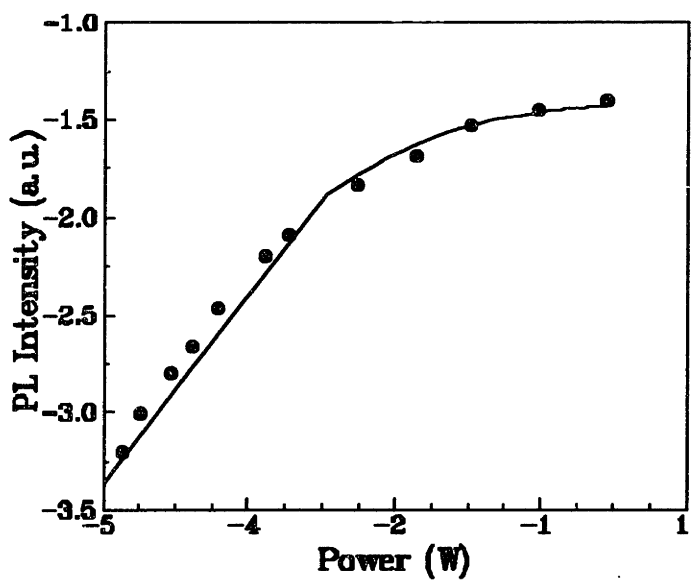

Fig. 6.3. Simulation the power dependence of PL intensity. The dot denotes experimental data. Solid line denotes simulation curve.

6.4 Temperature Dependence Simulation

Based on the assumption that Auger effect is mainly responsible for the quenching. The temperature dependence can be simulated by setting $\tau_q = 10^{-12}\ n + 5 \times 10^{-11}\ n_{eq}$. where n_{eq} is the equilibrium carrier density which is temperature dependent and is determine by the Fermi level (Eq. 5.3). Therefore, it is necessary to determine the Fermi level of the system, which depends on doping and impurity levels in the system. It is known that the background doping of n-type or p-type Si wafers will introduced a shallow donor or acceptor level about 45 meV in the gap. The spreading resistance measurements for these samples show that there is an donor level in the gap. The position could be about 0.18 eV below CB, which is from the junction photocurrent spectroscopy measurement (Fig.5.14). Thus, for the p-type sample, there is a compensation region. Based on this information, Fig. 6.4 gives schematic diagram of gap energy levels for n-type and p-type samples. The donor level is assumed to be 0.18 eV below CB. Spreading resistance gives a density of the impurity donor of about 1.2×10^{16} cm^{-3}. In the simulation, the background doping is assumed to be 10^{16} cm^{-3}.

Based on the Fermi-Dirac statistics of occupation and charge neutrality relations, the Fermi level can be determined and the free carrier density can be calculated by Eq. (5.4).

Fig. 6.5 shows the temperature dependence of free carrier density for the n-type sample. There is a sharp increase from 4 K to 100K, followed by a relative flat region between 100 K and 150 K, and then a relatively slow increase. The majority carrier is the electron. Fig. 6.6 is the temperature dependence of free carrier density plot for the p-type sample. The simulation tells that the electron is the majority free carrier. The equilibrium concentration of electron is negligible when $T < 100$ K and increases sharply between 150 K and 300 K. The different temperature dependence behavior for n-type and p-type samples provides a reasonable explanation for the thermal quenching in these samples. The simulated temperature dependence of PL intensity for p-type and n-type sample are is

shown in Fig. 6.7 and Fig. 6.8, respectively. The experimental data is also plotted in the Figures for comparison.

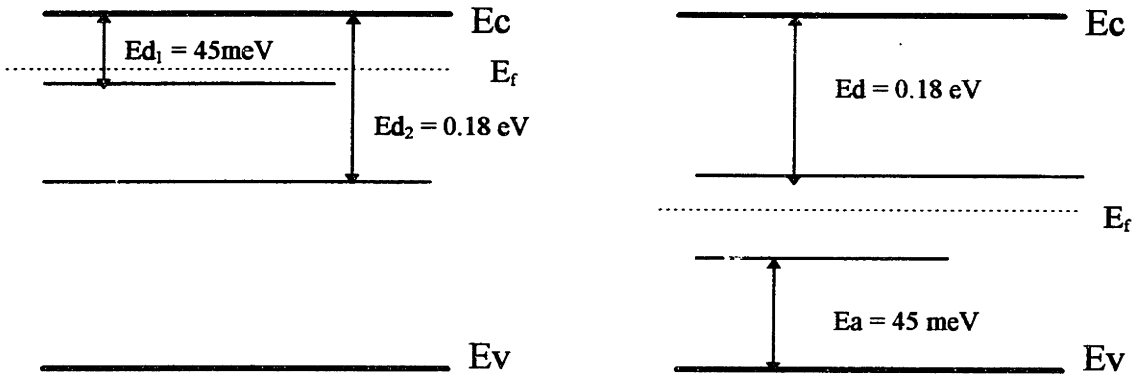

(a) n-type (b) p-type

Fig. 6.4 The schematic diagram of energy levels in the gap (a) n-type; (b) p-type. The drawing are not in scales.

These Figures show that the general trend of quenching is reproduced for both samples. However, some disagreements do exist. The simulation suggests that there is no quenching before 100 K for p-type sample. It is not in agreement with experimental evidence. This may be due to the following reasons: (1) We have not obtained the full picture of the sample. Maybe there are more shallow donor levels in the gap which give contribution to the free carrier density at the low temperature. (As DLTS measurement shows that there are 11 levels in the gap). The inhomogeneous profile of Er may also cause earlier quenching of the sample. The spreading resistance measurements show that for this type converted sample, part of Er profile is in p-type region, part of is in n-type region and part of is in the depletion region. (2) There could be another quenching mechanism at low temperature which is not equilibrium carrier density related, such as phonon coupling. No evidence has found to support this idea.

For the n-type sample, the simulation of temperature dependence of equilibrium carrier density and PL intensity confirms one of our hypothesis of last chapter, that there are three regions in the quenching curve. The flatness is due to the depletion of shallow donors. However, the Auger coefficient for equilibrium free carriers is modified from 5 x 10^{-11} to 2 x 10^{-12} because the former one gives too much quenching at the low temperature. The other one remains the same. The simulation does not give as much quenching as that shown in the experiment when T > 180 K. This is due to the slow increase of carrier density in Fig. 6.5. By modify the initial conditions, we can get a much stronger quenching when T > 150 K. This is shown in Fig. 6.9. In this case, the deep donor concentration is increased from 1.2 x 10^{16} cm^{-3} to from 1.5 x 10^{16} cm^{-3}. The background doping is also reduced to 4 x 10^{15} cm^{-3}. And the Auger coefficient for the equilibrium free carrier is back to the original value of 5 x 10^{-11}. Fig. 6.9 clearly demonstrates the three regions in the thermal quenching although the quenching at the low temperature is large compared to the experimental data. This may due to the incompleteness of the model. There is also possible a shallow acceptor compensating the strong earlier quenching in the real sample.

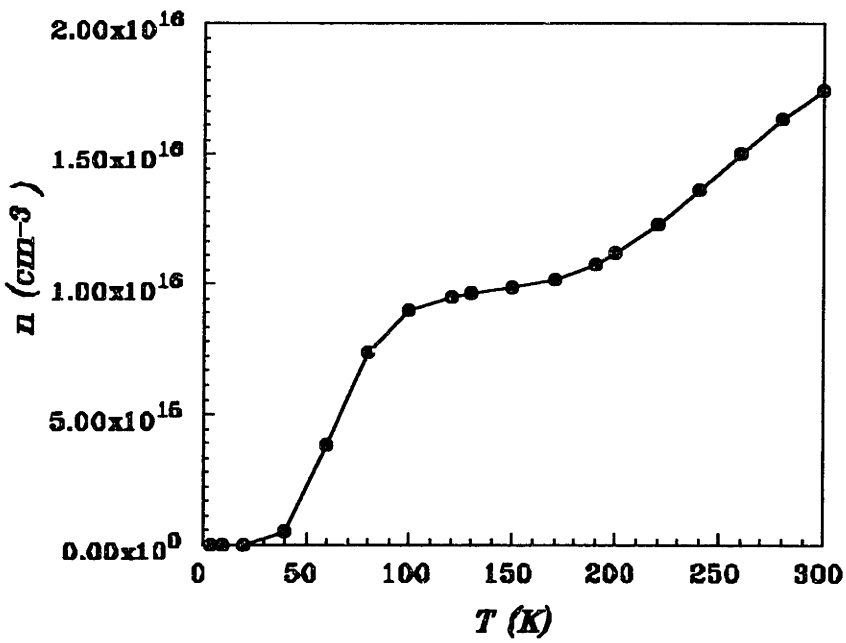

Fig. 6.5. The simulated temperature dependence of equilibrium free carrier density for n-type sample;

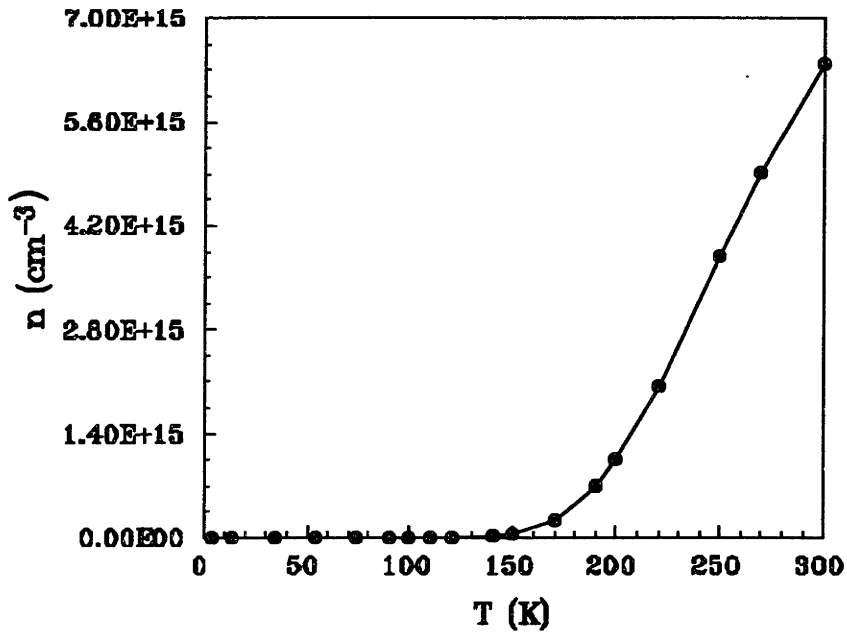

Fig. 6.6. The simulated equilibrium free carrier density for p-type sample

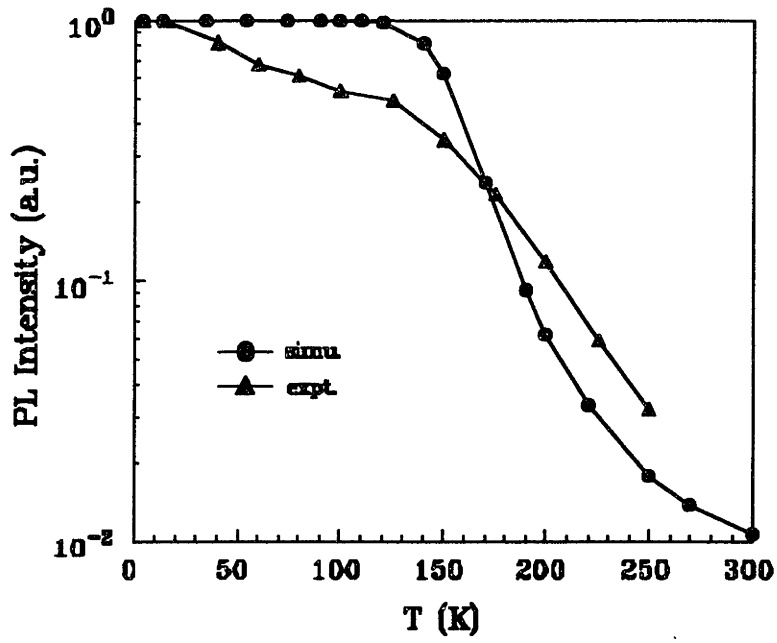

Fig. 6.7. The simulated thermal quenching effect comparing to experiment (p-type). Sample C.

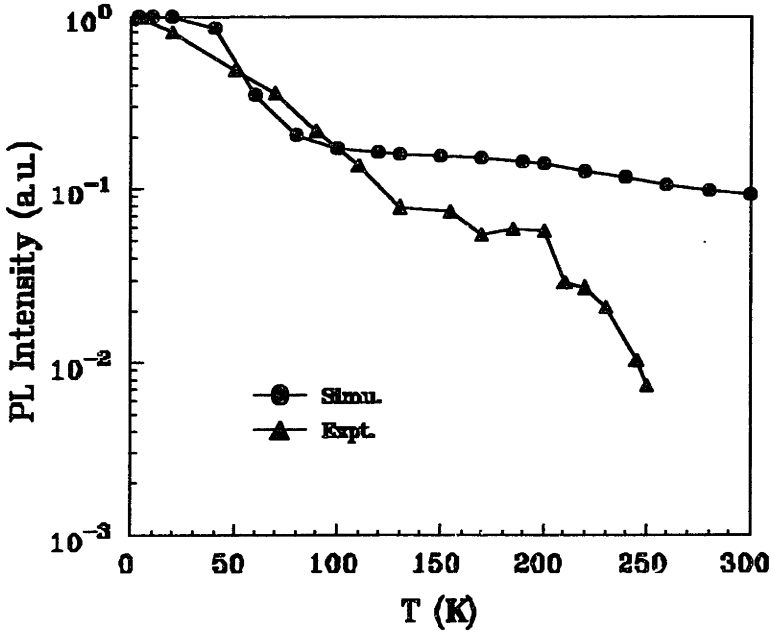

Fig. 6.8. The simulated thermal quenching effect comparing to experiment (n-type)

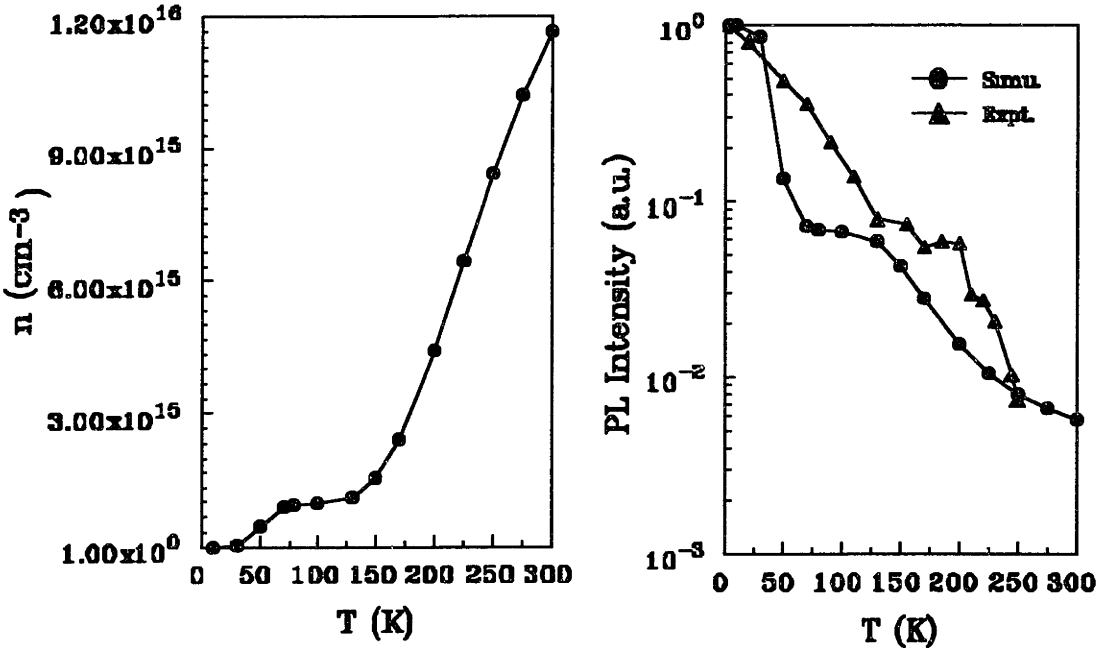

(a) (b)

Fig. 6.9. (a) The simulated temperature dependence of free carrier density. (b) The simulated thermal quenching effect comparing to experiment (n-type).

6.5 Exchange Effect

A detailed examination of Fig. 6.2 tells that the simulation curve does not show a sharp decrease at the low temperatures. A two exponential fitting shows that the contribution from short component is negative, but experimental data gives positive value. This difference may jeopardize the assumption of one Er center. However, Langer et al argued that this sharp decay is due to the exchange effect. This was confirmed by the experiment of Mn^{2+} luminescence in conducting CdF_2 [46]. The exchange effect is due to the weakly bound carriers which can exist at the low temperatures (below 40 K), because the carriers are frozen out on a shallow level (donor). It is easier to analyze if we assume the shallow level is the donor level. The Auger effect due to the weakly bound carriers is different from that of free carriers. Because in this case, the final state of the quencher is not its localized discrete state, but the ionized state with the electron excited high into the CB. The rate of energy transfer due to the exchange interaction is different from that due to electric dipole-dipole interaction and electric dipole-quadrupole interaction, because the interactions involved electric dipole are electrostatic in origin. The exchange interaction arises from requirement of the antisymmetry of the electronic wavefunctions. i.e., The luminescence spectrum of the Er^{3+} ion must overlap the absorption spectrum of the activator ions. The energy transfer rate can be estimated as [47]:

$$P_A = \frac{1}{\tau_r}\left[\frac{R_o}{R}\right]^m \tag{6.5}$$

where R_o is the critical distance at which the Auger effect equals the radiative probability. R is the distance between the excited Er^{3+} ions and the occupied shallow donors. m = 6 for electric dipole-dipole transfer. It has been proved that in the case where the exchange mechanism dominates, the transfer rate depends exponentially on the distance. The PL intensity of Er at the time t after an excitation pulse can be written as the following product [47]:

$$I(t) = Io\exp\left[-\frac{t}{\tau_r}\right]\exp\left[-\frac{C}{Co}f_i\left[\frac{t}{\tau_i}\right]\right] \tag{6.6}$$

where C is the activator (donor) concentration. $C_o = 3/(4\pi R_o^3)$ and f_i is a universal function dependent only on the kind of interaction. For an electric multipole interactive, f_i is equal to [47]:

$$f_m = \Gamma(1-\frac{3}{m})\left[\frac{t}{\tau_r}\right]^{3/m} \qquad (6.7)$$

where m = 6, 8, 10 fore the dipole-dipole, dipole-quadrupole, etc., type of interaction. For the exchange interaction

$$f = \gamma^{-3} g\left[\frac{e^{\gamma} t}{\tau_r}\right] \qquad (6.8)$$

Fig. 6.10 is the simulated the result of the exchange effect by setting $\gamma = 50$, $\tau_r = 1$ ms. c = $1x10^{16}$ cm^{-3}. It clearly shows a very sharp decay at the beginning. Double exponential fitting gives two lifetimes of 980 μs and 10 μs, respectively. But I am not convinced that the exchange effect is responsible for the sharp decay at the beginning. However, it at least gives an hypothetical explanation of the experimental observation. Some studies show that the exchange term is likely to be dominant at low temperature especially in the case that spin-orbit interaction is important[42]. At the high temperature, the bound carriers are dissociated unless they are very deep. There should be very little exchange effect. Then the sharp decay could come from the sharply increased free carrier Auger effect, which cause the decrease of lifetime and results in an overall sharp decay.

A more complicated model involving formation of free excitons and bound excitons is under study, and has shown sign of improvement. For example, the decay curve is sharper at the beginning and the contribution for this sharp decay is positive. However, these more complicated rate equations have more coefficients that may or may not be verified by experiments. More careful study is needed before we can discuss it further.

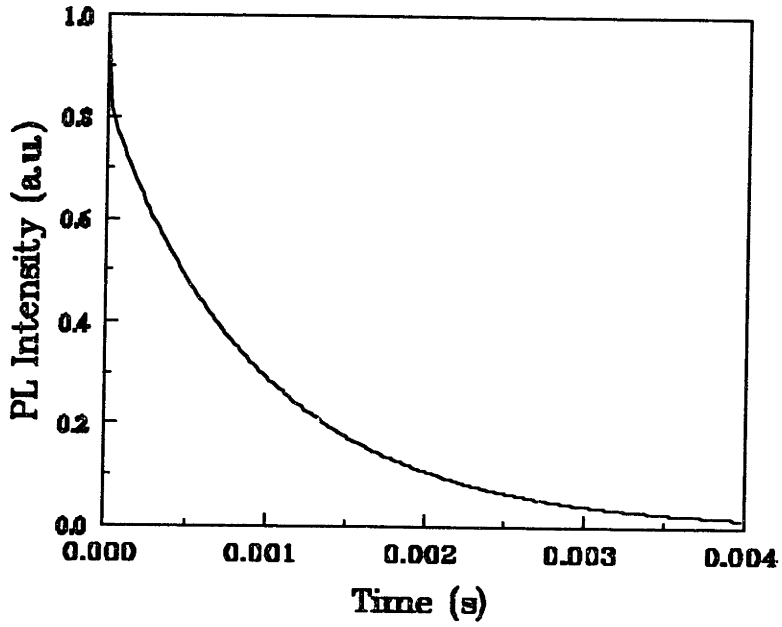

Fig. 6.10. Simulation of exchange effect shows a very sharp decay at the beginning.

In this chapter, the simulation of PL process was performed based on the assumption that Auger effect is the main quenching mechanism. By comparing to the experimental evidence, the model successfully describes the power dependence of PL intensity, and reasonably describes the trend of temperature dependence of PL intensity. The model supports the role of Auger recombination is the thermal quenching process in the PL. The simulation also suggests that the weakly bound carrier Auger effect might be responsible for the nonexponential sharp decay at the low temperature. It is necessary to have experimental data about the temperature dependence of the free carrier density to have better agreement between the model and the experiment for the temperature dependence of PL measurement.

Chapter 7

Summary and Future Work

7.1 Summary

The photoluminescence from Si:Er generates lots of excitement in the silicon based semiconductor industry. The λ=1.54 μm emission wavelength matches the minimum loss of the optical fiber transmission. The success of room temperature Si:Er LEDs proves its credibility of being a strong competitive candidate to the III-V optoelectronic materials. It has other advantages over the III-V material besides its compatibility with current semiconductor industry such as a narrow and stable linewidth with respect to operating temperature. However, a breakthrough is needed to increase the room temperature PL intensity and to be remain competitive in the future semiconductor industry. This breakthrough can only come from the study of fundamental properties of Si:Er and the adoption of optimal processing conditions. Some of the fundamental properties are the interaction between Er and the Si host, Er lattice site in Si and the excitation and deexcitation mechanisms. Based on the understanding of fundamental properties, processing conditions can be improved to maximize the number of optically active Er centers.

The interaction between Er and Si is investigated by the first principle MSW Xα calculation. The calculation shows that $4f$ electrons are not completely localized. The degree of mixing with Si host depends on the lattice of Er and the surrounded ligands. In the case of isolated Er in Si, the interstitial position is favorable. The dominant f levels are in the gap and have only little mixing with Si 2s 2p electrons. The electronic structure of these levels is $4f^1$. The cluster is stable at a "3+" charge state. However, the substitutional

position for the isolated Er is unstable due to the nonbonding between Er and Si. The formation energy is very high since all the $4f$ levels are in the CB.

The theoretical study of the ligand effect on Er shows that the presence of oxygen changes the site preference of Er. The oxygen tends to interact strongly with interstitial Er. There is large mixing of Si-O-Er and $4f$ electrons are not atomic like anymore. In practice, this result indicates that PL intensity from this center (if it exists) will be decreased which contradicts the experimental evidence that PL intensity is enhanced by the coimplantation of oxygen. On the other hand, the unstable and delocalized substitutional Er becomes stable and localized under the influence of oxygen ligands. The $4f$ electron levels is about 3.0 eV below the VB in contrast to the isolated interstitial case of $4f$ electrons is in the gap. The test suggests that when substitutional Er is surrounded by more than 6 oxygen atoms, Er is most stable and atomic like. The study also demonstrates that high symmetry configurations such as T_d are favorable for the oxygen ligand but lower symmetries such as C_{3v} is favorable for the fluorine ligand. In both of the favorable configurations, the energy level splitting caused by the crystal field effect is only about 0.1 eV, much less than value of the spin-orbit interaction about 1.0 eV.

Quasirelativistic calculation is used for the calculation. Comparing to the nonrelativistic calculation, improvement is clearly demonstrated. The interaction of hyperdeep levels (5s 5p) of Er with Si host is significantly reduced. However, spin-orbit interaction has not been considered in the current calculation. Further improvement is expected by including the relativistic calculation in the model.

The experimental study of the excitation and deexcitation mechanisms reveals several important things. We showed that the activation energy is not a fundamental properties of Si:Er samples due to its power dependence. Only at low temperatures, it is possible to saturate Er centers. As temperature is increased, the saturation behavior is less and less due to the increased efficiency of nonradiative processes. However, it is possible to saturate all the optically active Er at very high power for different temperatures. We concluded that there is no structural transformation during the temperature increase. The Auger effect is most probable factor in the thermal quenching of PL. This is verified by measuring the lifetime of a Si:Er LED under reversed bias or with a 2-beam illumination

experiment. This nonradiative process becomes more and more efficient as the temperature is increased.

The rise time and decay time behave in the opposite direction with respect to the pump power and temperature. The rise time is not sensitive to the temperature but it decreases rapidly with the increase of power. The decay time shows very limited response to the power, but it becomes shorter and shorter when the temperature is increased.

The lifetime study on different ligand impurities indicates that the lifetime may not depend on the type of ligand impurity, but it does depend on the process conditions and implantation dose. Three fluorine samples annealed at 1000 K, 900 K and 800 K give three different lifetime of 1ms, 800 μs and 600 μs. The PL intensity is also different for these samples. The relationship between the measured lifetime and PL intensity is unclear at this moment.

The thermal quenching of PL shows different characteristics for n-type and p-type samples. There are three distinct regions of the thermal quenching in n-type samples compared to one continuous quenching in p-type samples. These three regions are 4 K < T 100K, 100K < T < 150K and T>150k.

Junction photocurrent spectroscopy measurement (JPS) strongly indicates that there is a donor level at 0.18 eV below the CB This information is valuable for the understanding and modeling of the emission process.

Based on the experimental evidence and assumptions. the kinetics of the PL process was simulated by a set of rate equations. The simulated results are in good agreement with the experimental data. Power and temperature dependence of the PL intensity have been reasonably described by the model. The simulation also suggests the possibility that the sharp decay at the beginning of PL signal is due to the exchange effect involving weakly bound carriers.

7.2 Future Work

The quasirelativistic calculation already demonstrates the importance of relativistic effects. However, the quasirelativistic effect only includes Darwin and mass-velocity correction. The spin-orbit interaction is not considered. The energy levels obtained in the calculation

are the Stark manifolds under the crystal field influence. The spin-orbit calculation will enable us to identify the $I_{15/2}$ and $I_{13/2}$ states. Furthermore, based on the Slater transition theory [], the transition energy between these two states can be estimated. It is also possible to obtain the oscillator strength for every transition between each stark manifold. By comparing the oscillator strength of each transition, we may be able to explain the relative intensity of each peaks in the PL spectrum.

There are several interesting experiments that can be done to further investigate the quenching mechanism. As discussed in Chapter 5 and 6, the equilibrium free carrier density is the lifetime killer in the PL process. Measuring temperature dependence of equilibrium carrier density will allow us to directly verify the Auger quenching mechanism $P_A = C_A n$. Hall effect measurements should give reasonably values of carrier density. Another measurement related to the temperature dependence of free carrier density is the thermally stimulated capacitance (TSCAP).

There is still some uncertainty regarding the number of erbium centers in the silicon. A direct experiment to settle this controversy is to separate the short and long components by using an additional chopper. By comparison of the spectra of these components should give us the answer . If the spectra are different, a multi-center model is likely, otherwise the one-center model is valid.

The one Er center model has to be further improved by including the quenching contribution from holes, the formation of free and bound excitons etc. This consideration will increase the number of rate equations and the difficulty of solving them together. It also increases the uncertainty of results because more parameters are involved. It is also interesting to simulate the two-Er-center model to see how the two Er centers behave under different powers and temperatures.

Appendix A: Processing Conditons and Measurements of Samples

Sample	Sample ID	doping	[Er]	MeV	Ligand	Anneal cond. [C], [hr]	dev
A	c2	p/1.e16	5.e17	4.5	[O], 3.e18	900, 1/2	x (P)
B	JJ2	p/?	1.e18	4.5	[B], 1.e18	900, 1/2	-
C	c5	p/1.e17	5.e17	4.5	[O], 3.e18	900, 1/2	x (As)
D	d61	n/1.e16	5.e17	4.5	[O], 3.e18	900, 1/2	x
E	c26b	p/1.e16	5.e17	0.4	[Se], 2.e18	800, 1/2	-
F	c26e	p/1.e16	5.e17	0.4	[Se], 2.e18	900, 1/2	-
G	66	p/1.e16	3.e18	1.0	[F], 3.e18	900, 1/2	-
H	c18e	p/1.e16	5.e17	0.4	[C], 2.e18	800, 1/2	-
I	c16b	p/1.e16	5.e17	0.4	[O], 2.e18	800, 1/2	-
J	14	p/1.e16	5.e17	1.0	[F], 5.e18	1000, 1/2	-
K	12	p/1.e16	5.e17	1.0	[F], 5.e18	800, 1/2	-
L	c24b	p/1.e16	5.e17	0.4	[Cl], 2.e18	800, 1/2	-
M	6T	p/1.e18	5.e17	4.5	[O], 3.e18	900, 1/2	-
N	6E	p/1.e18	5.e17	4.5	[O], 3.e18	900, 1/2	pn
O	h1	p/1.e16	5.e17	4.5	[O], 3.e18	900, 1/2	x (As)

Sample	Sample	date	measurement type
A	c2	9-7-94 8-9-94 9-5-94	EL & PL lifetime (I,T) PL with reversed bias at RT EL & PL bias
B	JJ2	1-14-95 1-23-95 1-19-95	Lifetime (T, PW) 2-beam PL (T)
C	c5	11-17-94	PL(T)
D	d61	2-1-95 3-6-95	PL (T) PL (T,PW)
E	c26b	1-17-95	Lifetime (4k)
F	c26e	3-24-95	PL (T, PW)
G	66	8-31-94 9-3-94 9-6-94 1-17-95	Lifetime (T, PW) Lifetime (T, PW) Lifetime (90k-170k) Lifetime (4k)
H	c18e	1-17-95	Lifetime (4k)
I	c16b	1-17-95 3-24-95	Lifetime (4k) PL (T, PW)
J	14	1-14-95	lifetime (4k)
K	12	6-17-94 7-7-94 7-12-94 1-14-95	lifetime (T,PW) PL (T,PW) PL (PW at 30k, 60k,120k,200k) Lifetime (4k)
L	c24b	1-19-95	lifetime (4k)
M	6T	12-1-94	PL (T)
O	H1	12-20-94 12-17-94	PL (T, PW) Lifetime(T)

Bibliography

[1] B. Zheng, J. Michel, F.Y.G. Ren, D.C. Jacobson, J.M. Poate, and L.C. Kimerling

[2] J. Michel, J.L. Benton, R.F. Ferrante, D.C. Jacobson, D.J. Eaglesham, E.A. Fitzgerald, Y.-H. Xie, J.M. Poate, and L.C. Kimerling. J. Appl. Phys. 70, 2672 (1991).

[3] G.H. Dieke, *Spectra and Energy Levels of Rare Earth Ions in Crystals*, Interscience Publishers, John Wiley & Sons, Inc, 1968.

[4] H.M. Crosswhite and H.W. Moos, *Optical Properties of Ions in Crystals*, Interscience Publishers, John Wiley & Sons, Inc, 1967.

[5] K.H. John, private communication.

[6] A. Kozanecki, ACTA Physica Polonica A, Vol. 84 (1993).

[7] K. Takahei, A. Taguchi, in: Defects in Semiconductors 16, Eds. G. Davies, G. Deleo, M. Stavola, Mater. Res. Forum, Vol. 83-87, Trans. Tech. Publ. Zurich 1991, p 641.

[8] E. Alves, M.F. Da Silva, K.R. Evans, C>R. Jones, A.A. Melo, and J.C. Soares, Nucl. Instrum. Methods B 80/81, 180 (1993).

[9] K. Takahei, A. Taguchi, and Y. Horikoshi, J. Appl. Phys. 76 (1994).

[10] Y.S. Tang, J. Zhang, K.C. Heasman, and B.J. Sealy, Solid State Commun. 72, 991 (1989).

[11] H. Przybylinska, J. Enzenhofer, G. Hendorfer, M. Schoisswohl, L. Palmetshofer and W. Jantsch, Proceedings of ICDS 17, Gmunden, Austria (1993).

[12] K.H. Johnson, Advan. Quantum Chem., 7:143, 1972.

[13] K.H. Johnson and F.C. Smith. In P. M. Marcus, J.F. Janak, and A.R. Williams, editors, Computational Methods in Band Theory, Page 377. Plenum Press, 1971.

[14] W. Kohn. In R.M. Dreizler and J. Da Provincia, editors, *Density Functional Methods in Physics*, page 1. NATO ASI Series, series B: Physics Vol. 123, Plenum, 1985.

[15] P.G. Parr and W. Yang, *Density Functional Theory of Atoms and Molecules*, Volume 16 of the The international Series of Monographs on Chemistry. Oxford University Press, 1989.

[16] D. A. Case, Ann. Rev. Phys. Chem. 33:151 (1982).

[17] J.G. Norman, Mol. Phys. 31, 1191 (1976).

[18] R.E. Watson, Phys. Rev., 111:1108 (1958).

[19] M. Boring, and J.H. Wood, J. Chem. Phys. 71, 32 (1979).

[20] C.Y. Yang, S. Rabii, Phys. Rev. A 12, 362 (1975).

[21] H. Enne, J. Schneider, G. Pomrenke and A. Axmann, Appl. Phys. Lett. 43, 943 (1983).

[22] S. Coffa, F. Priolo, and G. Franzo, Phys. Rev. B 48, 782 (1993).

[23] X. Z. Wang and B. W. Wessels, APL. 65, 845 (1994).

[24] M. Godlewski, K. Swiatek and B. Monemar, Journal of Luminescence, 58, 303 (1994).

[25] X.M. Fang, Y. Li, and D. W. Langer, JAP. 74, 6990 (1993).

[26] H. Isshiki, H. Kobayashi, S. Yugo, and T. Kimura, APL. 58, 484 (1991).

[27] S.J. Chang, and K. Takahei, APL. 65, 433 (1994).

[28] H. Efeoglu, J.H. Eveans, T.E. Jackman, B. Hamilton, D.C. Houghton, J.M. Langer, A.R. Peaker, D. Perovic, I. Poole, N. Rave, P. Hemment, and C.W. Chan. Semicond. Sci. Techol. 8, 236 (1993).

[29] K. Takahei, and A. Taguchi, Jpn. JAP. 33, 709 (1994).

[30] X.Z. Wang and B.W. Wessels, APL. 65, 584 (1994).

[31] M. Needels, M. Schiluter, and M. Lannoo, Phys. Rev. B 47, 15 533 (1993).

[32] C. Delerue and M. Lannoo, Phy. Rev. Lett. 67, 3006 (1991).

[33] L. A. Hemstreet, Defects in Semiconductors. Edited by H.J. Von Bardeleban. Trans. Tech. Publications, Switzerland. Mat. Sci. Forum. Vol. 10-12, 85 (1986).

[34] R. Saito and T. Kimura, Phys. Rev. B 46, 1423 (1992).

[35] A. Fazzio, J. Leite and M. L. Siqueira, J. Phys. C:Solid State Phys. Vol. 12, 513 (1979)

[36] S. Coffa, Phys. Rev. (1994).

[37] R.G.F. Ren, Ph.D. Thesis.

[38] C. G. Yan de Walle, F.R. Mcfeely, and S.T. Pantelides, Phy. Rev. Lett. 61, 1867 (1988).

[39] D.L. Adler, D.C. Jacobson, D.J. Eaglesham, M.A. Marcus, J.L. Benton, J.M. Poate, and P.H. Citrin, Appl. Phys. Lett. 61, 2118 (1992).

[40] J. Michel, K.C. Kimerling, J.L. Benton, D.J. Eaglesham, E.A. Fitzgeral, D.C. Jacobson, J.M. Poate, Y.-H. Xie, and R.F. Ferrante, Mat. Sci. Forum. Vol. 83-87, P653 (1992).

[41] P.B. Klein and G.S. Pomrenke, Electron. Lett. 24, 1503 (1988).

[42] J.M. Langer, J. Luminescence 40&41, 589 (1988).

[43] S. Schmitt-Rink, C.M. Varma, and A.F.J. Levi, Phy. Rev. Lett. 66, 2782 (1991).

[44] J.L. Benton, J. Michel, L.C. Kimerling, D.C. Jacobson, Y.-H. Xie, D.J. Eaglesham, E.A. Fitzgerald, J. M. Poate, J. Appl. Phys. 70, 2667 (1991).

[45] J.A. Majewski and J.M. Langer, ACTA PHYSICA POLONICA, Vol. A67, 51 (1985).

[46] A. Suchocki and J.M. Langer, Phys. Rev. B 39, 7905 (1989).

[47] M. Inoruti and F. Hirayama, The J. of Chem. Phys. 43, 1978 (1965)

THESIS PROCESSING SLIP

FIXED FIELD: ill _____ name _____

index _____ biblio _____

▶ COPIES: Archives Aero Dewey ~~Hum~~ Hum

Lindgren Music Rotch Science

TITLE VARIES ▶☐ _____

NAME VARIES: ▶☐ _____

IMPRINT: (COPYRIGHT) _____

▶COLLATION: 116 l _____

▶ADD. DEGREE: _____ ▶DEPT.: _____

SUPERVISORS: _____

NOTES:

cat'r: date:

page: 5101

▶DEPT: MatSci + E

▶YEAR: 1995 ▶DEGREE: M.S.

▶NAME: GAN, Fangi